IJCESEN

ISSN : 2149-9144

International Journal of Computational and Experimental Science and ENgineering

ijcesen@gmail.com

Volume: 4 - No:3 - 2018

Founder-Editor in Chief : **Prof.Dr. İskender AKKURT**

dergipark.gov.tr/ijcesen

Journal Info	
Web	dergipark.gov.tr/ijcesen
E-mail	ijcesen@gmail.com
ISSN	2149-9144
Frequency	March-July-November
Founded	2015
Journal Abbreviation	IJCESEN
Language	English-Turkish

Founder-Editor-in-Chief	
Prof.Dr. İskender AKKURT	Suleyman Demirel University-TURKEY

Editorial Board	
Prof.Dr. Mahmut DOGRU	Fırat University- TURKEY
Prof.Dr.Mitra DJAMAL	Institut Teknologi Bundung-INDONESIA
Prof.Dr. Sevil CETINKAYA	Cumhuriyet University- TURKEY
Prof.Dr. Mohamed EL TOKHİ	United Arab Emirates University-UAE
Prof.Dr. Nezam AMİRİ	Sharif University-IRAN
Prof.Dr. Berin SİRVANLI	Gazi University- TURKEY
Dr. Nabi IBADOV	Warsaw University of Technology-POLAND
Dr. Zuhal ER	Istanbul Technical University- TURKEY
Dr. Nurten Ayten UYANIK	Isparta Uygulamalı Bilimler University- TURKEY
Dr. Amer AL ABDEL HAMİD	Yarmouk University-JORDAN
Dr. Zehra Nur KULUÖZTÜRK	Bitlis Eren University- TURKEY
Dr. Dhafer ALHALAFI	De Montfort University, Leicester-UK
Dr. Zeynep PARLAR	Istanbul Technical University- TURKEY
Dr. Mandi ORLİC BACHLER	Zagreb University of Applied Sciences-CROATIA
Dr. M. Fatih KULUÖZTÜRK	Bitli Eren University- TURKEY
Dr. Irida MARKJA	University of Tirana-ALBANIA
Dr. Kadir GÜNOĞLU	Isparta Uygulamalı Bilimler University- TURKEY
Dr. Ahmet BEYCİOĞLU	Adana Bilim Teknoloji University- TURKEY
Dr. Hakan AKYILDIRIM	Suleyman Demirel University- TURKEY
Dr. Zakaria MAAMAR	Zayed University-UAE
Dr. Tomasz PIOTROWSKI	Warsaw University of Technology-POLAND

Table of Contents

Volume: 4	**No: 3**	**November-2018**	
Authors	**Title**	**DOI:**	**Pages**
Ayfer ERGİN, Mustafa Fatih ERGİN	Reduction of Ship Based CO_2 Emissions from Container Transportation	10.22399/ijcesen.429944	1-4
Serkan Aydın, Hakan YÜKSEL	Internet Based Data Collection and Analysis of Objects in Solar Energy Production Systems	10.22399/ijcesen.358359	5-8
Sedat YILMAZ, Züheyr KAMACI	Resistivity and Seismic Refraction Studies on Kısıklı Landslide (Antalya, Turkey)	10.22399/ijcesen.348792	9-14
Gür Emre GÜRAKSIN, Eyüp Can BİÇER, Atilla EVCİN	Characterization of Hydroxyapatite Coating on Ti6Al4V by Sol-gel Method	10.22399/ijcesen.379088	15-19
Xueli GUO, Jun LI, Gonghui LIU, Hui YAN	Numerical Simulation of Casing Stress during Multi-stage Fracturing Based on Stage Finite Element Method	10.22399/ijcesen.418035	20-24
Lei ZHENG, Xiaodong WU, Ruidong ZHAO, Huachang LI, Mengyun LIU	Study on performance of progressing cavity pumps (PCPs) in different fit modes	10.22399/ijcesen.474462	25-29
Nai CAO, Hong LI, Mengyun LIU	Effect of Stress Sensitivity on Production of Tight Heterogeneous Reservoir	10.22399/ijcesen.444575	30-33
İsmail YÜCE	Yarns that Emit Far Infrared Rays	10.22399/ijcesen.368405	34-38
Baki BAĞRIAÇIK, Sefer Ercan EPSİLELİ, Emre PINARCI, Mustafa BELEN	Comparison of Bearing Capacity of Piled Raft Foundations Consisting of Different Number of Piles under Static and Repetitive Loads	10.22399/ijcesen.477263	39-42
MURAT OZSOY, İsmet TIKIZ, Hüseyin PEHLİVAN	Thermal Analysis of a Zirconium Dioxide Coated Aluminum Alloy Piston	10.22399/ijcesen.479222	43-50

International Journal of Computational and Experimental Science and Engineering (IJCESEN)
Vol. 4-No.3 (2018) pp. 1-4
http://dergipark.gov.tr/ijcesen

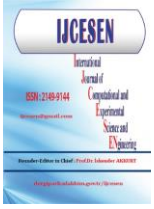

ISSN: 2149-9144

Research Article

Reduction of Ship Based CO_2 Emissions from Container Transportation

Ayfer ERGİN[1]*, M. Fatih ERGİN[2]

[1]Istanbul University, Engineering Faculty, Maritime Transportation Management Engineering Name of Institution/Department, 34320 Istanbul/ TURKEY
[2]Istanbul University, Engineering Faculty, Chemistry Engineering, 34320 Istanbul/TURKEY

* **Corresponding Author** : ayfersan@istanbul.edu.tr
ORCID: 0000-0002-6276-4001

Article Info:

DOI: 10.22399/ijcesen.429944
Received : 2 June 2018
Accepted : 19 July 2018

Keywords

Container transportation
CO_2 emissions
Carbon footprint

Abstract:

Today, with the globalization of the world, traders have almost removed the borders. Therefore, there has been a considerable increase in demand for people to reach each other. This also led to the increase in maritime transport which has approximately 80% of the volume of worlds' freight load and also is the most economical mode of transportation. Despite being the most environmentally friendly transport system, the current CO_2 emission rate due to sea transport is 2.5%. Also, 26% of CO_2 emissions and energy consumption resulting from maritime transportation is caused by container ships which only generate 16% of world fleet. In this context, container transport has been examined in terms of CO_2 emissions. Slower steaming requires less bunker consumption and fewer bunkering port calls thus lowering CO_2 emissions compared to steaming at normal speeds. However, it takes more navigation time and vessels to meet the vessel-routing schedule but it can also reduce fuel cost. This study investigates CO_2 emissions responsible for a container ship to determine bunker fuel saving and CO_2 reduction strategies for container shipping lines. A case study was carried out using the real shipping data of a container ship with a capacity 1880 TEU between Ambarlı and Savannah ports. Additionally, two different scenarios have been proposed to reduce the emission of a real container ship in operation.

1. Introduction

International shipping trade is vital for the global economy. It is responsible for more than 80% of world trade. Seaborne trade volume increased by 2.6% from 2015 to 2016 and reached 10.3 billion tons [1]. Maritime transport system is the most environmentally friendly among other transportation systems. Nevertheless it gives off around 1000 million tons of CO_2 per year and is account for approximately 2.5% of global greenhouse gas emissions [1,2]. Growing emissions of greenhouse gases cause of negative impacts on human health and the climate change [3]. Container shipping is the fastest growing segment of marine transportation by about 5% growth. One of the reasons for this increase is that container transportation can easily be integrated with other transportation modes. In addition, container transport has vital importance to supply chains with short transit time ability.

Bunker fuel costs comprise of a large part of the operating costs of container shipping line. Ronen emphasizes that bunker fuel costs are responsible for around 75% of the operating costs of a large container ship [4]. In this context, in order to save fuel consumption and to decrease the amount of emission, a case study was made. The case study was implemented utilization the real shipping data of a container ship with a capacity 1880 TEU between Ambarlı and Savannah ports. Two different scenarios have been suggested to reduce the emission of a real container ship in operation.

1.1. Literature Review

The sailing speed is the main criterion that determines the fuel consumption of a ship. There are many studies in the literature that deal with speed optimization to reduce fuel consumption and emissions. Fagerholt et al. addressed the problem of determining the optimal speed on a particular route [5]. Carlou analyzed effects of relation of CO_2 emission and reducing of speed in the container ship [6]. Kim et al. investigated amount of fuel and optimum ship speed for a fixed ship route [7]. Notteboom and Cariou researched the effects of slow sailing on BAF charge paid by shipper as well as fuel consumption at the ship [8]. Khor et al. implemented a software program to optimize the speed of large container ships. As a result the optimum speed was found to be 19.5 knots [9]. Sheng developed a mathematical model that takes into account the size and optimum speeds of container ships. The model cannot be used for vessels higher than 16,000 TEU [10]. Doudnikoff et al. investigated differences speed between inside and outside SECA which amount of CO_2 emissions and the total transit time [11]. Meng et al. used a mathematical model to investigate the fuel efficiency of container ships [12]. Mao et al. established a model for ship's speed prediction by using two statistical approaches [13]. Tai and Lin analysed possible changes main routes in the container shipping as a result of the Panama canal expansion. These changes on emissions was examined [14]. There are studies in the literature that focus on emissions in certain regions and ports such as sea of Marmara sea [15], Candarli Gulf Turkey [16], United States ports [17], Taiwan ports [18].

2. Calculation of Emission

The ship emission is influenced by fuel type, engine type, fuel consumption, operation mode, time period in operation mode, emission factors and weather conditions. The amount of shipping emissions between Turkey and USA is calculated for a container ship. Additionally, in this study, real data obtained from a container ship with a capacity of 1880 TEU was used. The emission amounts emitted by sailing ship are calculated as follows [16, 19]:

$$E^e = E_S^e + E_M^e + E_P^e \tag{1}$$

$$E_S^e = T_S \times F_t^0 \times K_{S,e}^0 = \frac{D_{i\sim j}}{V} \times F_t^{h0} \times K_{S,e}^{h0} + \frac{D_{i\sim j}}{V} \times F_t^{d0} \times K_{S,e}^{d0} \tag{2}$$

$$E_M^e = T_M \times F_t^0 \times K_{M,e}^0 = T_M \times \left(F_t^{h0} \times K_{M,e}^{h0} + F_t^{d0} \times K_{M,e}^{d0}\right) \tag{3}$$

$$E_P^e = T_P \times F_t^0 \times K_{P,e}^0 = \frac{Q_i}{EF_i} \times F_t^{d0} \times K_{P,e}^{d0} \tag{4}$$

2.1. Case Study

In the study is utilized case study of a real container ship from a global shipping. The transit time of the selected ship in the case study is 25 days between Ambarlı and Savannah ports. The container ship has been standing on the port for about 9 days for loading and unloading operations and sailing for 15 days on sea. In the study, firstly the emission amount for a specific route was calculated. The total CO_2 emissions of the ship are calculated 7.46 tonnes CO_2 per specific route. Then, daily amount of emissions per TEU are found. The daily CO_2 emission for the dry container is 0.15 kg and the reefer container is 0.22 kg.

Two different scenarios have been proposed to reduce the emission of a real container ship in operation. In the first scenario, the ship speed is reduced by 0.5 knots from the speed value in the actual scenario. Reduced fuel consumption of the ship is calculated. The total CO_2 emissions of the ship is found 6.62 tonnes CO_2 per route for first scenario. The daily CO_2 emission for the dry container is 0.13 kg and the reefer container is 0.20 kg. Reduced ship speed causes the transit time to increase. As a result the transit time between Ambarlı and Savannah ports is increased by 10 hours. However, this situation has led to a decrease in the amount of fuel consumed. The amount of emissions generated by the container ship has decreased. In scenarios first a reduction of 11.27% was calculated for the CO_2 emission amount from the container ship per a specific route.

In the second scenario, the ship speed is reduced by 1.0 knots from the speed value in the actual scenario. Reduced fuel consumption of the ship is found. The total CO_2 emissions of the ship is found 5.90 tonnes CO_2 per route for second scenario. The daily CO_2 emission for the dry container is 0.12 kg and the reefer container is 0.19 kg. Reduced ship speed causes the transit time to increase. As a result the transit time between Ambarlı port and Savannah port is increased by 21 hours. However, this situation has led to a decrease in the amount of fuel consumed. In Figure 1 show that the fall in speed has an effect on fuel consumption.

The amount of emissions generated by the container ship has decreased. In scenarios second a reduction of 20.84% was calculated for the CO_2 emission amount from the container ship per a specific route. Not only the carbon footprint of the ship but also the carbon footprint per container is calculated in the study. Figure 2 shows reducing a container ship' speed is decreased amount of emissions per container.

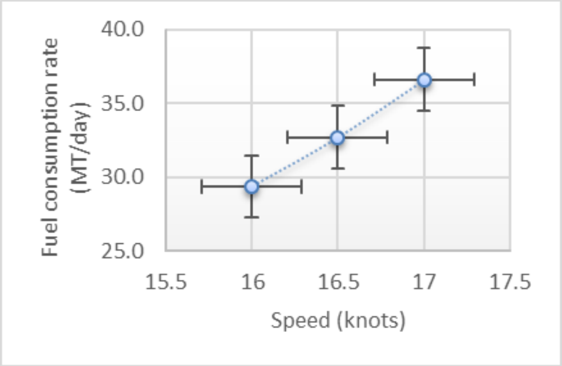

Figure 1. *Fuel consumption rates of container ship at different speeds.*

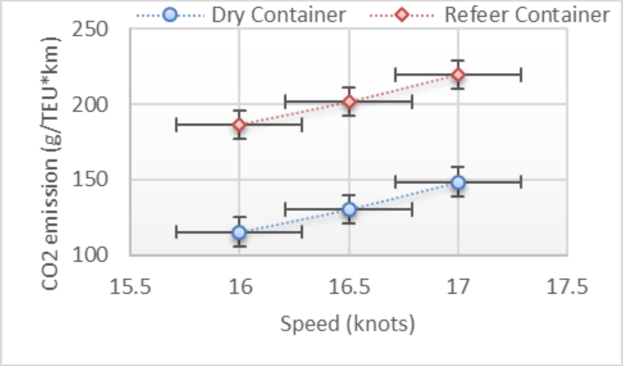

Figure 2. *CO_2 emissions of per container at different speeds.*

3. Conclusion

This study researches CO_2 emissions responsible for a container ship to determine bunker fuel saving and CO_2 reduction strategies for container shipping lines. A case study was carried out using the real shipping data of a container ship with a capacity 1880 TEU between Istanbul Ambarlı port and Savannah port. The emission amount of the container ship was calculated during the route. The total CO_2 emissions of the ship are calculated 7.46 tonnes CO_2 per specific route. This research also involves carbon footprint calculation per dry container and reefer container. A container ship accounts for daily CO_2 emission for the dry container is 0.15 gr and the reefer container is 0.22 kg.

Two different scenarios have been proposed to reduce the emissions of the container ship. In the first scenario shows that reducing the container ship's speed form 17 knot to 16.5 knot has decreased CO_2 emissions by around 11.27% between Istanbul Ambarlı port and Savannah port. In the second scenario indicates that reducing the container ship's speed form 17 knot to 16 knot has decreased CO_2 emissions by around 20.84% for the same route.

Positive impact of slow steaming provides that emission reduction from ship and fuel consumption saving. Bunker fuel costs also comprise of a large part of the operating costs of container shipping lines. The slow steaming strategy is crucial in terms of fuel and emissions reduction for container shipping industry. Global container companies should adopt a variety of technological and operational strategies to reduce bunker consumption, such as lower ship speeds, energy-saving and low-carbon power and drive systems, better body designs, voyage optimization systems and renewable energy sources.

References

[1] Hoffmann, J., the Review of Maritime Transport 2017. United Nations Publication, 2017.
[2] Sekimizu, K., Third IMO GHG Study 2014 Executive Summary and Final Report.: Micropress Printers, Suffolk, UK., 2015.
[3] Xhafka, E., J. Teta, and E. Agastra. "Mobile Environmental Sensing and Sustainable Public Transportation Using ICT Tools." network 6 (2015), DOI: 10.12693/APhysPolA.128.B-122
[4] Ronen, David. "The effect of oil price on containership speed and fleet size." Journal of the Operational Research Society 62.1 (2011): pp: 211-216.
DOI: 10.1057/jors.2009.169
[5] Fagerholt, Kjetil, Gilbert Laporte, and Inge Norstad. "Reducing fuel emissions by optimizing speed on shipping routes." Journal of the Operational Research Society 61.3 (2010): pp:523-529.
DOI: 10.1057/jors.2009.77
[6] Cariou, Pierre. "Is slow steaming a sustainable means of reducing CO_2 emissions from container shipping?." Transportation Research Part D: Transport and Environment 16.3 (2011): pp: 260-264.
DOI: 10.1016/j.trd.2010.12.005
[7] Kim, Hwa-Joong, et al. "An epsilon-optimal algorithm considering greenhouse gas emissions for the management of a ship's bunker fuel." Transportation Research Part D: Transport and Environment 17.2 (2012): pp: 97-103.
DOI: 10.1016/j.trd.2011.10.001
[8] Notteboom, Theo, and Pierre Cariou. "Slow steaming in container liner shipping: is there any impact on fuel surcharge practices?." The International Journal of Logistics Management 24.1 (2013): pp: 73-86.

DOI:10.1108/IJLM-05-2013-0055

[9] Khor, Yee Shin, et al. "Optimum speed analysis for large containerships." Journal of Ship Production and Design 29.3 (2013): pp: 93-104.
DOI:10.5957/JSPD.29.2.120022

[10] Sheng, Xiaoming, Loo Hay Lee, and Ek Peng Chew. "Dynamic determination of vessel speed and selection of bunkering ports for liner shipping under stochastic environment." OR spectrum 36.2 (2014): pp: 455-480.
DOI: 10.1007/s00291-012-0316-1

[11] Doudnikoff, Marjorie, and Romuald Lacoste. "Effect of a speed reduction of containerships in response to higher energy costs in Sulphur Emission Control Areas." Transportation Research Part D: Transport and Environment 28 (2014): pp: 51-61.
DOI: 10.1016/j.trd.2014.03.002

[12] Meng, Qiang, Yuquan Du, and Yadong Wang. "Shipping log data based container ship fuel efficiency modeling." Transportation Research Part B: Methodological 83 (2016): pp: 207-229.
DOI: 10.1016/j.trb.2015.11.007

[13] Mao, Wengang, et al. "Statistical models for the speed prediction of a container ship." Ocean Engineering 126 (2016): pp: 152-162.
DOI: 10.1016/j.oceaneng.2016.08.033

[14] Tai, Hui-Huang, and Dung-Ying Lin. "The impact of trunk route deployment changes on pollutant emissions in international container shipping after Panama Canal expansion." The International Journal of Logistics Management 27.2 (2016): pp: 335-352.
DOI: 10.1108/IJLM-09-2014-0142

[15] Deniz, Cengiz, and Yalçın Durmuşoğlu. "Estimating shipping emissions in the region of the Sea of Marmara, Turkey." Science of the total environment 390.1 (2008): pp: 255-261.
DOI: 10.1016/j.scitotenv.2007.09.033

[16] Deniz, Cengiz, Alper Kilic, and Gökhan Cıvkaroglu. "Estimation of shipping emissions in Candarli Gulf, Turkey." Environmental monitoring and assessment 171.1-4 (2010): pp: 219-228.
DOI: 10.1007/s10661-009-1273-2

[17] Corbett, James J., Haifeng Wang, and James J. Winebrake. "The effectiveness and costs of speed reductions on emissions from international shipping." Transportation Research Part D: Transport and Environment 14.8 (2009): pp: 593-598.
DOI: 10.1016/j.trd.2009.08.005

[18] Cullinane, Kevin, Po-Hsing Tseng, and Gordon Wilmsmeier. "Estimation of container ship emissions at berth in Taiwan." International Journal of Sustainable Transportation 10.5 (2016): pp: 466-474.
DOI: 10.1080/15568318.2014.975303

[19] Tai, Hui-Huang, and Dung-Ying Lin. "Comparing the unit emissions of daily frequency and slow steaming strategies on trunk route deployment in international container shipping." Transportation Research Part D: Transport and Environment 21 (2013): pp: 26-31.
DOI: 10.1016/j.trd.2013.02.009

International Journal of Computational and Experimental Science and Engineering (IJCESEN)
Vol. 4-No.3 (2018) 5-8
http://dergipark.gov.tr/ijcesen

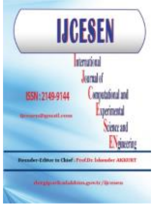

ISSN: 2149-9144

Research Article

Internet Based Data Collection and Analysis of Objects in Solar Energy Production Systems

Serkan AYDIN[1], Hakan YÜKSEL[2]

[1]Suleyman Demirel University, Technical Science Vocational School, Electricity and Energy Depart. Isparta-Turkey
[2]Suleyman Demirel University, Technical Science Vocational School, Computer Programming Depart. Isparta-Turkey

* **Corresponding Author** : serkanaydin@sdu.edu.tr
ORCID: 0000-0003-1358-7579

Article Info:

DOI: 10.22399/ijcesen.358359
Received : 27 November 2017
Accepted : 30 July 2018

Keywords :

Solar Energy
Internet of Things
Renewable Energy
Microcontroller

Abstract:

In this study, some parameters were measured during the production phase of the electricity generated by the solar panel. Light, temperature, humidity, voltage, current and power measurements were carried out during the production of the electric energy of the solar panel. Measurements were instantly transferred to the cloud technology. The Internet of Things (IoT) is very popular today. Many objects can communicate with each other. Measured data for objects can also be analyzed on an instantly, hourly, daily, etc. basis thanks to cloud technology. Renewable energy keeps updating the energy generation system of the future and it is constantly developing. In this study, the parameters measured in renewable energy systems were examined.

1. Introduction

It is important that the information used in automation and industrial systems be used in real time. Different systems are used to transfer this information in real time [1]. These systems generally store the measured values as a database or cloud-based. Thanks to this data, many faults are prevented. Within the system efficiency, the necessary values are obtained. These systems are often called the Internet of Things (IoT).

Internet of Things (IoT) is technologies that enable sensors to transmit data generated by sensors attached to objects wirelessly and control objects. Nowadays, it has started to have a very important place by using a lot of fields and has played an important role in the development of this technology in various fields and it continues to play important roles [2].

Usage rates of devices connected to the Internet are increasing and we use in most areas. Today, there are billions of devices connected to the Internet [3]. In recent years, the Internet of Things (IoT) has begun to be used in many areas, and some of them are smart houses. In similar systems, the measured data is stored in the cloud technology via different systems. With these records, it is possible to instantly or later display the data presented to the user's use [4]. Smart houses do not only control data and control but also they are now in the process of producing their own energy. One of the most commonly used methods of producing their own energy is solar energy.

Solar energy is an important renewable energy source. The Wi-Fi system is an important system for control systems in terms of speed and accuracy in solar panel systems. By combining similar systems, instantaneous monitoring of measured values, energy efficiency detection and prevention of failures will be facilitated [5]. Solar energy or photovoltaic systems are one of the most important sources of renewable energy resources. The charge control system in solar energy systems is the heart of the system. If charge control is well done in solar energy systems, system efficiency can reach 97-98% [6]. There are many factors on PV panel power output in photovoltaic systems, some of which are surface temperature, panel position and electrical load resistance [7].

This study is a combination of intelligent systems such as the solar energy system, the Internet of Things, and the Arduino microcontroller system.

2. Materials and Methods

In this study, DHT11 air temperature and relative humidity sensor for the installed solar panel and temperature and humidity measurements of the environment of the solar panel were made. The LDR light sensor also was measured the light value of the solar panel. The ACS709 current sensor was measured the voltage and current values of the solar panel. With the Arduino Due microcontroller card, the values from the sensors were processed and transferred to the database using the cloud technology, with the help of the ESP8266-ESP-201 Wi-Fi module. The reason for using Arduino Due is that the values read from the sensors are processed more quickly and stably and the GPIO pins work better with the ESP8266-ESP-201 Wi-Fi module due to the operation with 3.3 volts. In the installed system, the values read from the sensors are recorded graphically in the database with the cloud technology. These values can be examined on an hourly, daily, monthly and annual basis. Figure 1 shows the block diagram of circuit components.

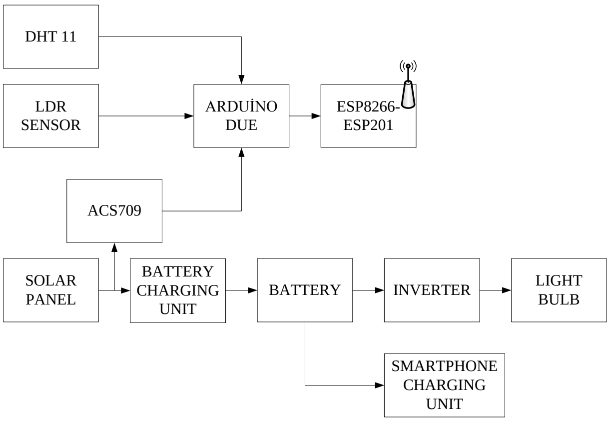

Figure 1. *Circuit Components Diagram*

The installed solar panel system is a 140 Watt solar panel. The electricity generated by the solar energy charges a 12V 60Ah hour gel accumulator via the charging circuit with a 10 A digital sun charge regulator. The accumulator is connected to a 300 W inverter. 220V 5W three led bulbs and a socket and photocell relay control are connected to the inverter. In addition, 12V / 5V six USB chargers are connected.

Figure 2. *Installed Solar Panel System*

Figure 3. *Charging and Wireless Data Transfer Station*

For a more stable measurement, the wireless data transmission system, the algorithm is drawn in Figure 4.

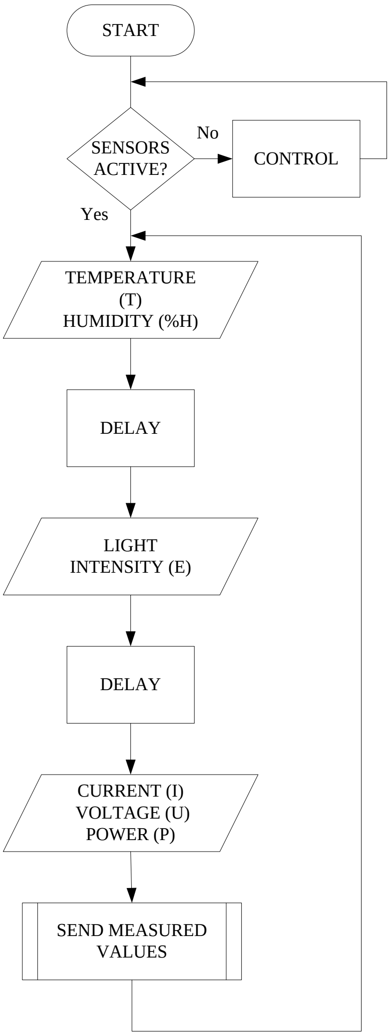

Figure 4. *System Algorithm*

3. Results

With the installation of the system, the data transferred to the cloud technology are transformed into graphics. For example, the hourly data of air temperature, relative humidity, light, current, voltage and power values are shown in Figures 5, 6, 7, 8, 9 and 10.

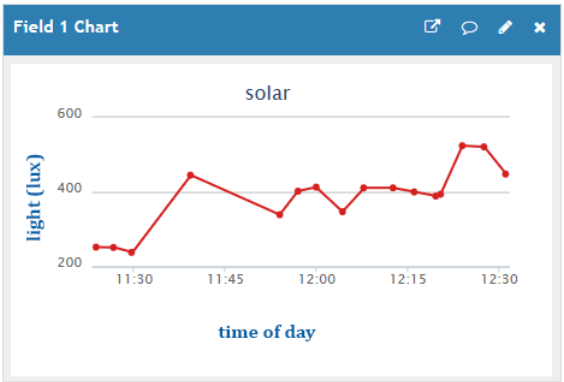

Figure 5. *Data* of Light

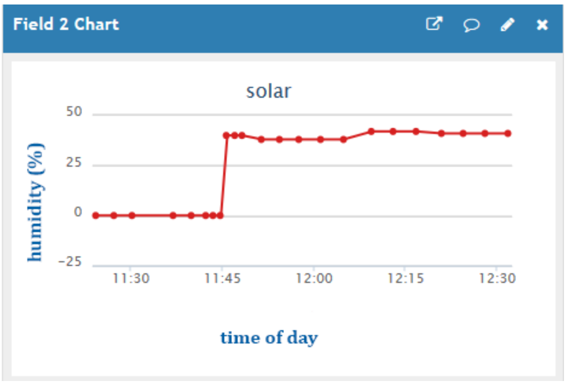

Figure 6. *Data* of Relative Humidity

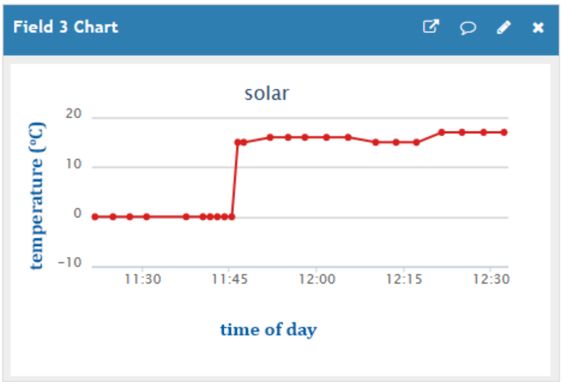

Figure 7. *Data* of Air Temperature

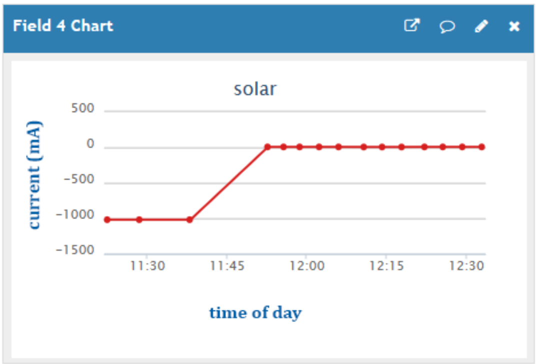

Figure 8. *Data* of Current

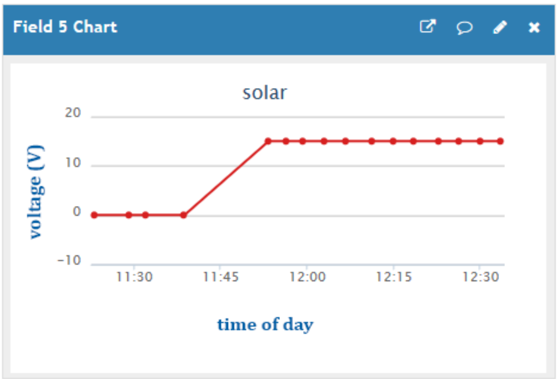

Figure 9. *Data* of Voltage

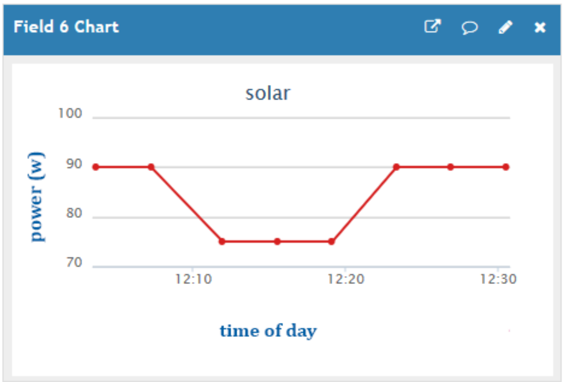

Figure 10. *Data* of Power

As a result of this study, the current, voltage and power values of the installed solar panel according to daylight, temperature and humidity values were recorded in the database via cloud technology. With these data, it is possible to determine at which intervals the most productive values can be reached. The measured values are recorded instantly to the cloud technology thanks to the Wi-Fi module.

As you can see from the figures, the measurements of relative humidity, air temperature and light values as well as the voltage, current and power values produced by the solar system have been applied. In this way, the efficient working data intervals of the system will be determined and the efficiency of solar systems will be improved.

4. Discussion

In today's technology, developments in renewable energy and cloud technology have gained momentum. The necessary calculations can be made to remove the hot spot effect in the solar panel systems and obtain the highest efficiency. By doing these calculations, studies can be developed to determine the positioning and turning angles of solar panels.

In addition, thanks to similar work, prototypes can be installed and measurements can be made prior to solar panel installation. These measurements will ensure that more accurate information is obtained before installing more powerful solar panels.

References

[1] Şimşek, M.A., Taşdelen, K., “Denetleyici Alan Ağı Üzerinden Sensör Verilerinin İzlenmesi”, SDU International Journal of Technological Science, Vol.8, No.1 (2016) pp. 20-33

[2] Köroğlu, O., **“**Nesnelerin İnterneti, Algılayıcı Ağları Ve Medya”**,** Akademik Bilişim 2015 Konferansı.

[3]Arslan, K., Kırbaş, İ., "Nesnelerin İnterneti Uygulamaları İçin Algılayıcı/Eyleyici Kablosuz Düğüm İlk örneği Geliştirme", Mehmet Akif Ersoy Üniversitesi Fen Bilimleri Enstitüsü Dergisi Özel Sayı 1 (2016) pp. 35-43

[4] Walia, N.K., Kalra, P., Mehrotra, D., An IOT by Information Retrieval approach: Smart Lights controlled using WiFi. 2016 6th International Conference - Cloud System and Big Data Engineering (Confluence), IEEE. (2016) pp. 708-712

[5] Joshi, S., Jadhav, A., Gavate, N., Yashwante, M., "Wi-Fi Based Parameter Monitoring for Solar Plant", IJESC Volume 6 Issue No.4 (2016) pp. 4085-4087

[6] Rokonuzzaman M. and Haider H.E., "Design and Implementation of Maximum Power Point Tracking Solar Charge Controller", 3rd International Conference on Electrical Engineering and Information Communication Technology (ICEEICT), IEEE (2016)

[7] Işıker, Y., Yeşilata, B., Bulut, H., "Fotovoltaik Panel Gücüne Etki Eden Çalışma Parametrelerinin Araştırılması", UGHEK'2006: I. Ulusal Güneş Ve Hidrojen Enerjisi Kongresi, (2006) pp. 150-155

International Journal of Computational and Experimental Science and Engineering (IJCESEN)
Vol. 4-No.3 (2018) pp. 9-14
http://dergipark.gov.tr/ijcesen

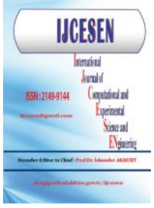

***ISSN:* 2149-9144**

Research Article

Resistivity and Seismic Refraction Studies on Kısıklı Landslide (Antalya, Turkey)

Sedat YILMAZ, Züheyr KAMACI

Süleyman Demirel University, Engineering Faculty, Geophysical Engineering Department, Isparta, Turkey

* **Corresponding Author** : zuheyrkamaci@sdu.edu.tr
ORCID: 0000-0002-2331-0162

Article Info:

DOI: 10.22399/ijcesen.348792
Received : 2 November 2017
Accepted : 31 May 2018

Keywords :

Landslide
Vertical electrical sounding
Seismic refraction
Turkey

Abstract:

When natural slope is disturbed by human activity such as road construction and infrastructure, continuous landslide monitoring is important to prevent loss of material and life. Therefore, this study aims to determine the landslide material, the possible sliding surface and the influence of groundwater on the landslide occurrence. Low cost monitoring landslide is performed which is vertical electrical sounding (VES) and seismic refraction methods. The case study area is located in the district of Kısıklı (Antalya province) in the Mediterranean Region of Turkey. VES survey were performed using Schlumberger electrode array at six locations. VES results interpretation leads to detect of maximum five geoelectrical layers. First, second and third layers represent saturated and permeable layer, while fourth and fifth layers correspond to an impermeable layer. Seismic refraction measurements were carried out on three profiles. Low velocity and elastic parameters relatively correspond to the permeable materials in near surface with thickness about 4-5 m higher porosity. The integrated of VES and seismic surveys allow mapping the weathered material at depth and providing depth information of the sliding surface which occurs at a depth between approximately 5 m and 20 m.

1. Introduction

Landslide is one of natural hazard that probably impact thousands of deaths and losses of billions of dollars every year [1]. It has different properties according to the cause of occurrence and shape [2]. It occur in the form of slipping, flowing and falling along a certain surface [3]. Therefore landslides are geologic complex formed from the combination of changes in contrast and physical values possessed by the layer [4].

Because of the high cost of geotechnical methods based on direct research, geophysical surveys are the best way to study landslides by determining landslide characteristics [5-7]. Therefore, relatively low cost and noninvasive geophysical methods provide new deals for promptly survey of large areas and produce detailed information about the landslide internal structure [8-10]. Vertical electrical sounding (VES/one-dimensional resistivity) and seismic refraction from field geophysical exploration methods are widely used to investigate the landslide area [11-16]. The success of the resistivity method is connected directly to the electrical resistivity contrast of different lithological units (clay, marl, limestone and etc [13, 17-19]. The first arrivals and their corresponding travel times of seismic refraction are analyzed. With survey of a landslide with geophysical methods may be determined the thickness and lateral extension of slip material, the possible sliding surface, the bedrock depth, the distribution of various materials and the status of groundwater within the slip mass [17, 18, 20-27]

In this study, a landslide occurred after heavy rainfall has been investigated. The maximum amount of rainfall in the landslide area formed between November and February 2010. This landslide occurred on February 2010 in Kısıklı district of Sarıabalı village of Serik town, Antalya in Turkey. Annual precipitation between 2008 and 2010 was 273 mm, 1399 mm and 1436 mm, respectively. There was not available daily rainfall data before landslide. In addition, the landslide had taken place after the huge Manavgat-Serik forest fire that broke out in the summer of 2008. Using VES and seismic refraction methods, the thickness of the mass causing landslide, water content, the sliding surface and bedrock structure has been uncovered.

2. Location and Geology

Study area is located in Kısıklı district of Sarıabalı village of Serik town of the province of Antalya in Mediterranean Region of Turkey (Fig. 1). Kısıklı landslide showing an inclination of about 17° is approximately 380 m long, about 90-110 m wide and in an environment with an altitude ranging from 50 m to 160 m. Many man-made structures, such as road along slope, a greenhouse site and several buildings, have been largely damaged by landslide (Fig. 2).

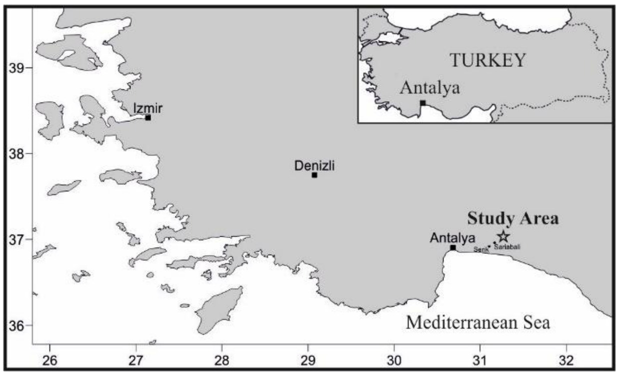

Figure 1. *Study area.*

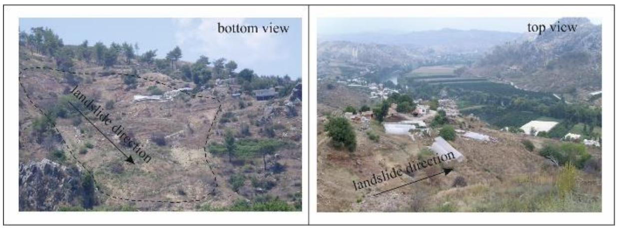

Figure 2. *Photographs of the site showing the landslide scarp and damaged structures.*

Kısıklı District includes the Ophiolitic Melange of the Antalya Nappes, the Miocene Tepekli Conglomerates and the Karpuzçay Formation [28-30]. The Ophiolitic Melange is mainly composed of limestone blocks, sandstone, marl, chert, shale, serpentinites. The Tepekli Formation around Sarıabalı region outcrops especially along the eastern margin of the Antalya Nappes and consists mainly of well-rounded clastic materials intercalated with mudstones. In places, reefal limestones embedded within the conglomerates can be observed in the area. The Antalya Basin, separated into three sub-basins such as the Manavgat, Köprüçay and Aksu, occurs within the Isparta Angle (Fig. 3) [30]. The Köprüçay Basin including the study area is separated from the Aksu Basin by the late Miocene Aksu Thrust and exists in the central position within the Antalya Basin [31, 32]. The Karpuzçay Formation includes mudstone, siltstone, conglomerates, detritic limestones and rests over the Tepekli Formation [33].

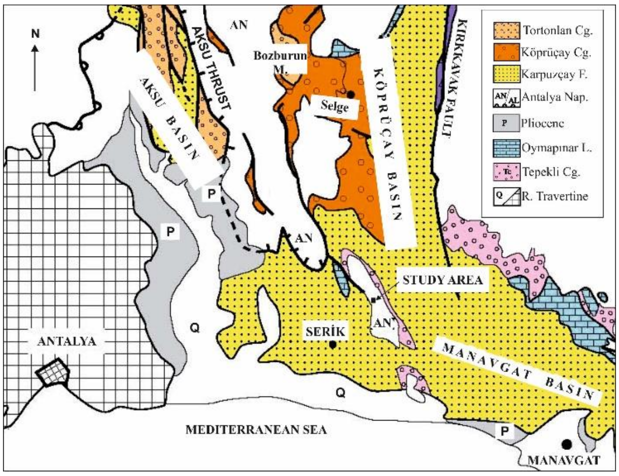

Figure 3. *Geology map of the East area of Antalya (modified after Deynoux et. al., 2005).*

3. Data Collection and Processing

The vertical electrical sounding (VES) method provides one-dimensional (1-D) underground information about the vertical electrical resistivity variation. The classic technique for field VES application is to use Schlumberger electrode array. Five Schlumberger stations were located inside landslide while the remaining one half-Schlumberger station is out landslide area (Fig. 4). Maximum current electrode interval ranges between 100 m and 150 m. VES Schlumberger data were inverted to their equivalent 1-D models composed of horizontal layers using modeling procedures. An algorithm developed by Zohdy [34] was first used to invert the field VES data. Then IPI2win software [35] was used to improve the first interpreted results.

The seismic refraction method, which benefits from waves traveling in different parts of the underground, is capable of mapping the boundaries between layers characterized by different seismic velocities. Seismic refraction is a quantitative technique that it provides the seismic velocities as well as determining the depths of different subsurface layers. Two kinds of seismic waves, namely the P-wave and the S-wave, can assist in the interpretation of geological layers. Three seismic refraction profiles were performed both forward and reverse shooting techniques. The seismic stations were located inside active landslide site (Fig. 4). Seismic refraction data were analyzed graphically, and P- and S- velocities were obtained from slopes of the time-distance graphs. Depths of the layers using travel time equations derived as a function of velocity were computed. Elastic parameters such as modulus of elasticity and Poisson's ratio that describe the subsurface material were calculated by using P- wave and S- wave velocities.

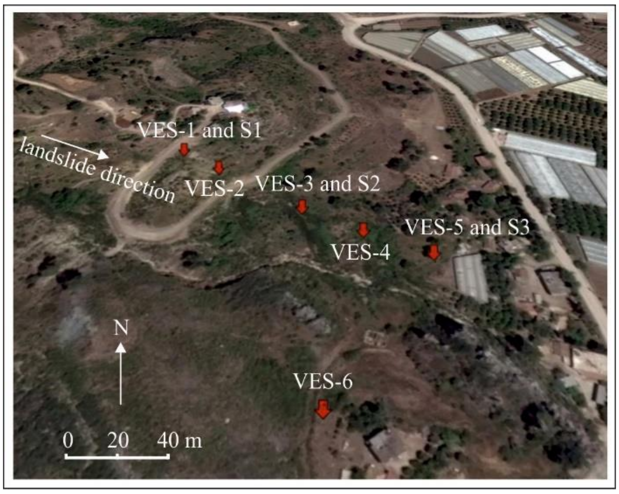

Figure 4. *Location of the measurement stations; six vertical electrical sounding (VES-1, VES-2, VES-3, VES-4, VES-5 and VES-6) and three seismic refraction (S1, S2 and S3) stations.*

4. Results and Discussion

Fig. 5 shows 1-D earth models from the resistivity data carried out at stations VES-1, VES-2, VES-3, VES-4, VES-5 and VES-6. Black lines are field data. Blue lines are 1-D models. Red lines show data calculated from 1-D models. The VES modeling results show that the shallow subsurface in the landslide area can be represented by 3 or 5 layers.

The first geoelectrical layer for VES-1 is characterized by mean 20 Ω m resistivity with thickness of 3 m. The second geoelectrical layer showed to be lower electrical resistivity value (approximately 12 Ωm with thickness of 12 m). The relatively high resistivity value for bottom layer was observed to be about 50 Ωm. The first layer for VES-2 is characterized by mean 60 Ω m resistivity with thickness of 3 m. The remained layers showed to be lower electrical resistivity values (between 17-30 Ωm). The first geoelectrical layer for mid-point VES-3 is characterized by mean 100 Ω m resistivity value with thickness of 2.3 m. The mid-geoelectric layer showed to be lower electrical resistivity value (between 23 Ωm and 35 Ωm with thickness of approximately 30 m). Bottom layer resistivity was observed to be on the rise. The first layer for VES-4 is characterized by mean 120 Ω m resistivity value with thickness of 1 m. The remained layers showed to be lower electrical resistivity values (between 15-35 Ωm). The first geoelectrical layer for VES-5 is characterized by mean 80 Ω m resistivity value with thickness of 1.7 m. The mid-geoelectric layer showed to be lower electrical resistivity value (between 20 Ωm and 30 Ωm with thickness of approximately 23 m). The bottom layer showed to be higher resistivity with approximately 100 Ωm. The higher resistivity values about 1300 Ωm were observed for VES-6 outside the landslide disturbed area.

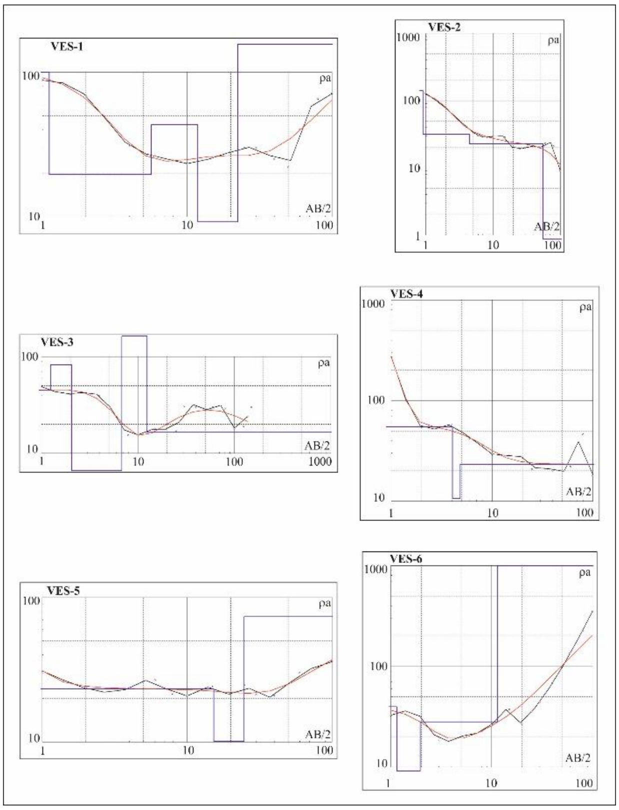

Figure 5. *The modelled VES curves using 1-D interpretation. Measured data (black curves), calculated data from 1-D model (red curves) and interpreted 1-D models (blue lines).*

Fig. 6 shows the resistivity section obtained from combining the VES results. The section illustrates the lateral and vertical variation of electrical resistivity along the profile in landslide area. In particular, the relatively low resistivity values between 13 Ωm and 30 Ωm correspond to impermeable materials, which are clay and water.

The relatively higher values than 30 Ωm resistivity correspond to the saturated mobilized landslide materials at a thickness between 5 m and 20 m.

Table 1 shows the P- wave and S- wave velocities, estimated thickness of the layer and dynamic elastic parameter as Poisson's ratio and modulus of elasticity concluded from the seismic records of three stations inside the landslide site. At seismic stations S1, S2 and S3 on the first layer, average seismic P-wave velocities were stated to be 446, 379 and 571 m/s. Their corresponding thicknesses were noted to be 5 m, 4 m and 4 m, respectively. The second layer, average seismic P-wave velocities were stated to be 1307, 1475 and 1361 m/s, and their corresponding thicknesses were noted to be 13 m, 11 m and 11 m, respectively. Average seismic P-wave velocities for the third layer were stated to be 2072, 2938 and 1996 m/s. Take into account, the modulus of elasticity is more sensitive to porosity changes than seismic wave velocities [36, 37]. This results in the assumption that the decrease in the modulus of elasticity and velocities in near surface is caused by high porosity. The Poisson distribution has values ranging from 0.08 to 0.43 (Table 1). The low Poisson's ratio (about 0.1) indicate that the material is silty clay and dry, while the high values (about 4 and above) indicate that the water content of the material is high.

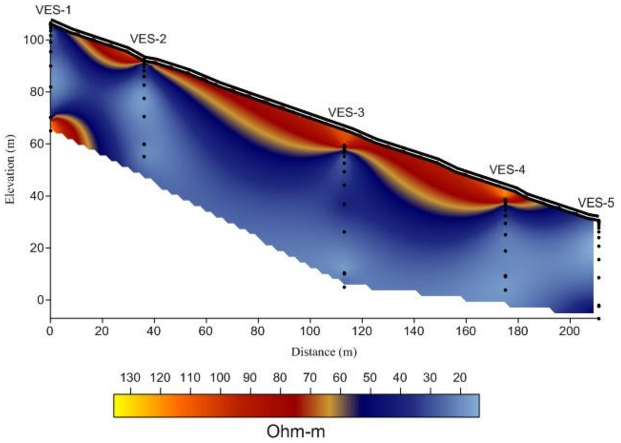

Figure 6. *Resistivity cross-section obtained from five modeled VES results.*

Table 1. *Summary of seismic refraction results.*

Parametric description	Layer	S1 station		S2 station		S3 station	
		Forward	Reverse	Forward	Reverse	Forward	Reverse
P-wave velocity (m/s)	1	446	446	379	379	571	571
S-wave velocity (m/s)		302	302	246	246	328	328
Modulus of elasticity (kg/cm^2)		2945,79	2797,73	2062,37	1880,61	4046,55	4088,03
Estimated thickness (m)		5	5	4	4	4	4
Poisson's ratio		0,08	0,08	0,14	0,14	0,25	0,25
P-wave velocity (m/s)	2	1307	1307	1475	1475	1361	1361
S-wave velocity (m/s)		611	611	523	523	626	626
Estimated thickness (m)		13	13	11	11	11	11
Modulus of elasticity (kg/cm^2)		18929,40	18929,40	15008,98	15008,98	20155,97	20155,97
Poisson's ratio		0,36	0,36	0,43	0,43	0,37	0,37
P-wave velocity (m/s)	3	2072	2072	2938	2938	1996	1996
S-wave velocity (m/s)		864	864	1205	1020	1020	1020
Modulus of elasticity (kg/cm^2)		43552,85	43552,85	33139,71	23745,15	57053,65	57053,65
Poisson's ratio		0,39	0,39	0,40	0,43	0,32	0,32

Integrated interpretation of the vertical electrical sounding and the seismic refraction tests revealed the internal structure of the disturbed landslide zone. Fig. 7 shows the slope section interpreted from the integration of two techniques. The slope cross-section permits to clearly define the slip/sliding surface, the thickness of the saturated landslide material and an impermeable layer consisting of clay and water.

5. Conclusion

Based on the vertical electrical soundings, subsurface in landslide disturbed area is represented by 3-5 geoelectrical layers characterized to be electrical resistivity values ranging from 10 Ωm and 120 Ωm within a total depth of 40 m. On the other hand, the resistivity values outside the landslide disturbed area were observed to be higher. The resistivity section obtained from the VES results illustrates the lateral and vertical variations in electrical resistivity. The relatively low resistivity values between 13 Ωm and 30 Ωm correspond to impermeable materials, which are determined by content of clay and water, particularly. The relatively higher values than 30 Ωm resistivity correspond to the saturated mobilized landslide materials at a thickness between 5 m and 20 m.

According to the results of the seismic refraction survey, the depth of about 15 m of subsurface in the landslide site is represented by 3 seismic layers. The layers within the landslide disturbed site are characterized by that the P- and S- velocities between 379-2938 m/s and 246-1020 m/s respectively. The decrease in seismic wave velocities and the modulus of elasticity in near surface is caused by high porosity.

The sliding surface between saturated and impermeable zones is at a depth between 5 m and 20 m with 1.5 m of soil material overlying between 3.5 m and 18.5 m of the mobilizing landslide material, which is presence of saturated and permeable material.

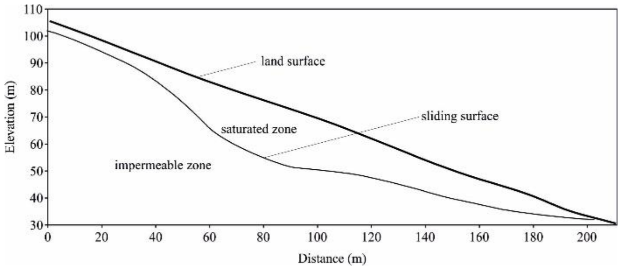

Figure 7. *The landslide section obtained from the analysis of resistivity and seismic data.*

Because of landslide occur after a huge Manavgat-Serik forest fire (summer 2008), future research is important for understanding landslide behavior in that particular area.

The integrated interpretation of 1-D electrical resistivity and seismic refraction tests is useful to figure out the subsurface structure in landslide direction. The investigation results will provide information for a stability assessment of the landslide area in the future.

References

[1] Klose M., B.Damm, B.Terhorst “Landslide cost modeling for transportation infrastructures: a methodological approach” Landslides. 12 (2014) 321-334

[2] Samia J., A.Temme, A.Bregt, J.Wallinga, F.Guzzetti, F.Ardizzone, et al. “Do landslides follow landslides? Insights in path dependency from a multi-temporal landslide inventory” Landslides. (2016) 1-12

[3] Yamao M., R.Sidle, T.Gomi, F.Imaizumi “Characteristics of landslides in unwelded pyroclastic flow deposits, southern Kyushu, Japan” Natural Hazards and Earth System Sciences. 16 (2016) 617-627

[4] Van Westen C.J. “National Scale Landslide Susceptibility Assessment for Saint Lucia” CHARIM Caribbean Handbook on Risk Information Management, World Bank GFDRR, ACP-EU Natural Disaster Risk Reduction Program. (2016)

[5] Jomard H., T.Lebourg, E.Tric “Identification of the gravitational boundary in weathered gneiss by geophysical survey: La Clapière landslide (France)” Journal of Applied Geophysics. 62 (2007) 47-57

[6] Lee C., C.H.Yang, H.C.Liu, K.L.Wen, Z.B.Wang, Y.J.Chen “A Study of the hydrogeological environment of the lishan landslide area using resistivity image profiling and borehole data” Engineering Geology. 98 (2008) 115-125

[7] Popescu M., R.D.Şerban, P.Urdea, A.Onaca “Conventional geophysical surveys for landslide investigations: two case studies from Romania” Carpathian Journal of Earth and Environmental Sciences. 11-1 (2016) 281-292

[8] Bogoslovsky V.A., A.A.Ogilvy “Geophysical methods for the investigation of landslides” Geophysics. 42 (1977) 562-571

[9] Cosenza P., E.Marmet, F.Rejiba, Y.J.Cui, A.Tabbagh, Y.Charlery “Correlations between geotechnical and electrical data: A case study at Garchy in France” Journal of Applied Geophysics. 60 (2006) 165-178

[10] Ling C., Q.Xu, Q.Zhang, J.Ran, H.Lv “Application of electrical resistivity tomography for investigating the internal structure of a translational landslide and characterizing its groundwater circulation (Kualiangzi landslide, Southwest China)” Journal of Applied Geophysics. 131 (2016) 154-162

[11] Fisseha F., G.Mewa “Road failure caused by landslide in north Ethiopia: A case study from Dedebit-Adi-Remets road segment” Journal of African Earth Sciences. 118 (2016) 65-74

[12] Martínez-Moreno FJ., F.A.Monteiro-Santos, J.Madeira, I.Bernardo, A.Soares, M.Esteves et al. “Water prospection in volcanic islands by Time Domain Electromagnetic (TDEM) surveying: The case study of the islands of Fogo and Santo Antão in Cape Verde” Journal of Applied Geophysics. 134 (2016) 226-234

[13] Yalcinkaya E., H.Alp, E.Ozel, E.Gorgun, S.Martino, L.Lenti et al. “Near-surface geophysical methods for investigating the Buyukcekmece landslide in Istanbul, Turkey” Journal of Applied Geophysics. 134 (2016) 23-35

[14] Confuorto P., D.Di Martire, G.Centolanza, R.Iglesias, J.J.Mallorqui, A.Novellino et al. “Post-failure evolution analysis of a rainfall-triggered landslide by multi-temporal interferometry SAR approaches integrated with geotechnical analysis” Remote Sensing of Environment. 188 (2017) 51-72

[15] Tábořík P., J.Lenart, V.Blecha, J.Vilhelm, O.Turský “Geophysical anatomy of counter-slope scarps in sedimentary flysch rocks (Outer Western Carpathians)” Geomorphology. 276 (2017) 59-70

[16] Yıldırım E., R.Saatçılar, S.Ergintav “Estimation of seismic quality factor: Artificial neural networks and current approaches” Journal of Applied Geophysics. 136 (2017) 269-278

[17] Akpan A.E., A.O.Ilori, N.U.Essien “Geophysical investigation of Obot Ekpo Landslide site, Cross River State, Nigeria” Journal of African Earth Sciences. 109 (2015) 154-167

[18] Perrone A., A.Iannuzzi, V.Lapenna, P.Lorenzo, S.Piscitelli, E.Rizzo et al. “High-resolution electrical imaging of the Varco d'Izzo earthflow (southern Italy)” Journal of Applied Geophysics. 56 (2004) 17-29

[19] Stan D., I.Stan-Kłeczek “Application of electrical resistivity tomography to map lithological differences and subsurface structures (Eastern Sudetes, Czech Republic)” Geomorphology. 221 (2014) 113-123

[20] Carpentier S., M.Konz, R.Fischer, G.Anagnostopoulos, K.Meusburger, K.Schoeck “Geophysical imaging of shallow subsurface topography and its implication for shallow landslide susceptibility in the Urseren Valley, Switzerland” Journal of Applied Geophysics. 83 (2012) 46-56

[21] Chambers J.E., P.B.Wilkinson, O.Kuras, J.R.Ford, D.A.Gunn, P.I.Meldrum et al. “Three-dimensional geophysical anatomy of an active landslide in Lias Group mudrocks, Cleveland Basin, UK” Geomorphology. 125 (2011) 472-484

[22] Grandjean G., J.C.Gourry, O.Sanchez, A.Bitri, S.Garambois “Structural study of the Ballandaz landslide (French Alps) using geophysical imagery” Journal of Applied Geophysics. 75 (2011) 531-542

[23] Hack R. “Geophysics for slope stability” Surveys in Geophysics. 21 (2000) 423-448

[24] Hibert C., G.Grandjean, A.Bitri, J.Travelletti, J.P.Malet “Characterizing landslides through geophysical data fusion: example of the La Valette landslide (France)” Engineering Geology. 128 (2012) 23–29

[25] McCann D.M., A.Forster “Reconnaissance geophysical methods in landslide investigations” Engineering Geology. 29 (1990) 59-78

[26] Yilmaz S. “A case study of the application of electrical resistivity imaging for investigation of a landslide along highway” International Journal of the Physical Sciences. 6-24 (2011) 5843-5849

[27] Yılmaz S., C.Narman “2-D electrical resistivity imaging for investigating an active landslide along a ridgeway in Burdur region, southern Turkey” Arabian Journal of Geosciences. 8-5 (2015) 3343-3349

[28] Akay E., S.Uysal “Post-Eocene tectonics of the Central Taurus Mountains” MTA Dergisi, 108 (1998) 23-34

[29] Çiner A., M.Karabıyıkoğlu, O.Monod, M.Deynoux, S.Tuzcu “Late Cenozoic sedimentary evolution of the Antalya Basin, southern Turkey” Turkish Journal of Earth Sciences. 17 (2007) 1-41

[30] Deynoux M., Ç.Attila, M.Olivier, M.Karabıyıkoglu, G.Manatschal, S.Tuzcu “Facies architecture and depositional evolution of alluvial fan to fan-delta complexes in the tectonically active Miocene Köprüçay Basin, (Isparta Angle, Turkey)” Sedimentary Geology. 173 (2005) 315-343

[31] Monod O., M.Deynoux, M.Karabiyikoglu, A.Çiner, C.Kuzucuoglu, G.Manatshal, S.Tuzcu, A.Hakyemez, M.Moullade “Enregistrement se´dimentaire de l’activite´ de la faille de Kirkkavak dans le bassin mioce`ne du Köprü Çay (Turquie meridionale)” 18e Re´union annuelle des Sciences de la Terre (2000) Paris p.199

[32] Monod O., G.Manatschal, M.Deynoux, A.Çiner, M.Karabiyikoglu, S.Tuzcu, C.Kuzucuoglu “Neogene morphotectonics in the Köprü Basin (Isparta Angle, Southern Turkey)” 11th Eug Meeting (2001) Strasbourg p.524

[33] Monod O., M.Karabiyikoglu, M.Deynoux, A.Çiner, G.Manatschal, S.Tuzcu, C.Kuzucuoglu, M.Moullade, A.Hakyemez, M.C.Janin, J.F.Babinot “Sedimentation, tectonics and geomorphology in the Neogene Antalya Basins: a synthetic outlook” 1st International Symposium of the Faculty of Mines (Itu) on Earth Sciences and Engineering (2002) Istanbul p.177

[34] Zohdy A.A.R. “A new method for the automatic interpretation of Schlumberger and Wenner sounding curves” Geophysics. 54 (1989) 245-253

[35] Shevnin V.A., I.N.Modin “IPI2win ver. 3.0.1- 1D interpretation of VES profile” Moscow State University (2003) Moscow

[36] Kirsch R. “Groundwater geophysics-A tool for hydrogeology” Springer (2006) Berlin

[37] Han D.H., A.Nur, D.Morgan “Effects of porosity and clay content on wave velocities in sandstones” Geophysics. 51 (1986) 2093-2107

International Journal of Computational and Experimental Science and Engineering (IJCESEN)
Vol. 4-No.3 (2018) pp. 15-19
http://dergipark.gov.tr/ijcesen
Copyright © IJCESEN
ISSN: 2149-9144

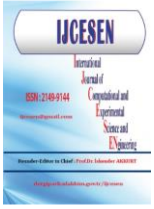

Research Article

Characterization of Hydroxyapatite Coating on Ti6Al4V by Sol-gel Method

Eyüp Can BİÇER[1], Atilla EVCİN[2], Gür Emre GÜRAKSIN[1]*

[1]Afyon Kocatepe University, Engineering Faculty, Biomedical Engineering Department, Afyonkarahisar-Turkey
[2] Afyon Kocatepe University, Engineering Faculty, Material Science and Engineering Depart, Afyonkarahisar-Turkey

*** Corresponding Author :** emreguraksin@aku.edu.tr
ORCID: 0000-0002-1935-278

Article Info:

DOI: 10.22399/ijcesen. 379088
Received : 15 January 2018
Accepted : 7 August 2018

Keywords :

Biomaterials
Hydroxyapatite
Sol-Gel
Ti Implants

Abstract:

Biomaterials are natural or synthetic materials that are used in human body and are materials to evaluate, treat, support or replace any tissue, organ, or function of the body. Due to its favorable biocompatibility and mechanical properties, HA-coated metal-based implants are used in the orthopedic surgery operations. For this purpose, sol-gel synthesized nano sized HA powders were produced. Ti6Al4V alloy was coated with hydroxyapatite (HA) by using the sol–gel method. Surface morphologies, thermal, mineralogical properties and bioactivity of the coatings were examined and the characterization of the coatings was performed by using DTA-TG, XRD, SEM, and EDX.

1. Introduction

Bone is a natural composite which mainly consists of an inorganic (Hydroxyapatite-HA) and an organic (collagen). Bones have different pore shapes according to their locations and functions throughout the body. The skeleton consists of two main structural types of bone as shown in Fig 1. Compact (cortical) bone is dense with a low surface area. Spongy (trabecular or cancellous) bone has a lower density and larger surface area than compact bone. The mineral part of the bone is constituted by calcium phosphates, in the forms of crystallized HA and/or amorphous calcium phosphates (ACP), which contains various ions like Na+, Mg^{2+}, K^{+}, CO_3^{2}-, Cl^{-}, and F^{-} [1,4].

HA is widely used as a substitute for bones and teeth owing to its excellent biocompatibility and its similar structure with the mineral part of the bone. However, its mechanical properties such as strength, hardness and toughness do not comply with mechanical properties of bone [6,8].

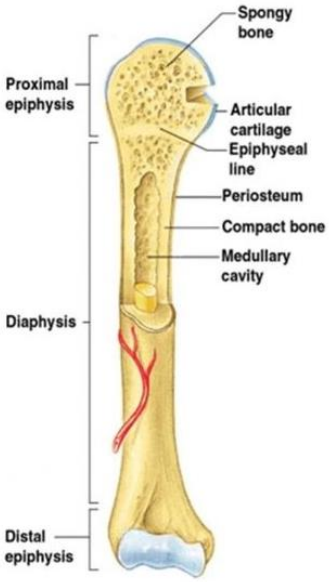

Figure 1 *Bone structure [5].*

Sol-gel process is an attractive alternative to other methods for synthesis of ceramics and glasses for many reasons: for example, low temperature synthesis, simple equipment to be used, thin film formability and so on [9-11].

Many researchers have used different methods for the fabrication of hydroxyapatite coatings such as plasma spray, HVOF, molecular beam epitaxy (MBE) vapor-liquid-solid mechanism (VLS) , solution-phase, shadow sputtering, and sol-gel methods [7].

In this work, we developed Hydroxyapatite nano particles and coating by sol-jel on Ti6Al4V metallic implant. Crystal structure, surface morphology, composition of samples was characterized by means of XRD, SEM, and EDX.

2. Materials and Methods

To synthesize powders chemically, Analytic grade $Ca(NO_3)_2.4H_2O$, $(NH_4)_2HPO_4$, NH_4OH were used as precursors. All chemicals were purchased from Merck and used as received. Ti6Al4V (Grade 5) was used as metallic implant to coat. 1.00 M stock solutions of calcium nitrate 4-hydrate and di-ammonium hydrogen phosphate were prepared using distilled water. A precipitate was formed by the drop-wise addition of the $(NH_4)_2HPO_4$ solution to the $Ca(NO_3)_2$ solution, with continuous stirring, to obtain a Ca/P ratio of 1.67 in the mixed solution. The solution was brought to pH 11 by addition of concentrated ammonium hydroxide solution (Fig 2). The obtained precipitation was HA. The precipitate was aged overnight at room temperature. The resulting powder was dried in an oven for 10 h. Finally, the dried powder was calcined in an electrical furnace at 1000 ºC for 2 h after heating at the rate of 5 °C/min. in air.

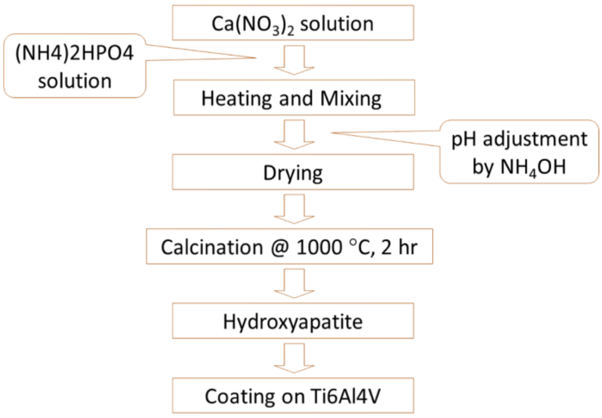

Figure 2 *Experimental flow chart*

This hydroxyapatite sol was deposited on a pre cleaned Ti6Al4V metallic implant substrate by dip coating method (Fig 3). An average of four layers was required for each film with 100 µm thickness. Then these films were air dried after deposition and heated and dried at 100 °C in an oven for 15 min. For hydroxyapatite phase formation, thin films were annealed at 500 °C for two hours at ambient conditions. Structural and thermal properties of calcined powders were characterized by XRD and DTA/TG respectively. Morphological and surface properties of annealed thin films were studied. In vitro bioactivity test of thin films were performed in stimulated body fluid (SBF) at 37 °C under static condition for 1-21 days.

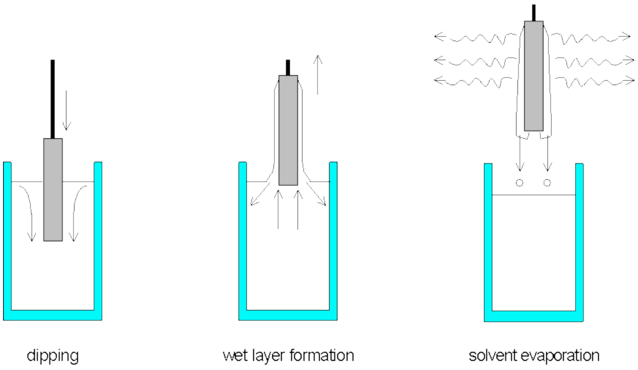

Figure 3. *Dip coating process (http://www.solgel.com/articles/Nov00/mennig.htm)*

2. Results and Discussion

The thermal properties of the HA powders were characterized by TG-DTA (Netzsch STA449F3) (Fig 4). There are one endothermic and two exothermic peak. An endothermic peak was found at 175 °C, due to removal of water and organic elements from powder. Thermal decomposition of the powder began at 400 °C. Second exothermic peak was observed at 800 °C. After this reaction, the crystal structure of the system becomes stable. Total weight loss was %11.44.

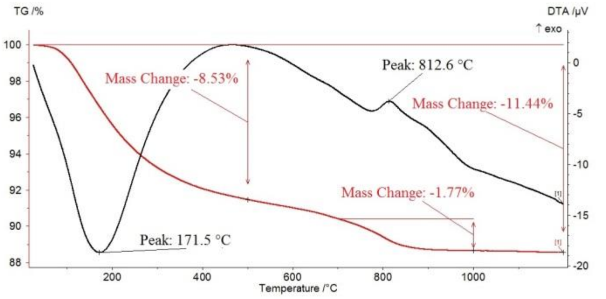

Figure 4. *DTA/TG Diagram of Hydroxyapatite powders.*

Crystal structures of the powders were characterized via powder X-ray diffraction (XRD, Bruker D 8 Advance) using Cu-Kα X-rays of wavelength = 1:5406 Å and data were taken in the 2θ range of 20° to 70° with a step of 0.1972°. As can be seen in Fig. 4, all spectra showed the HA reflections.

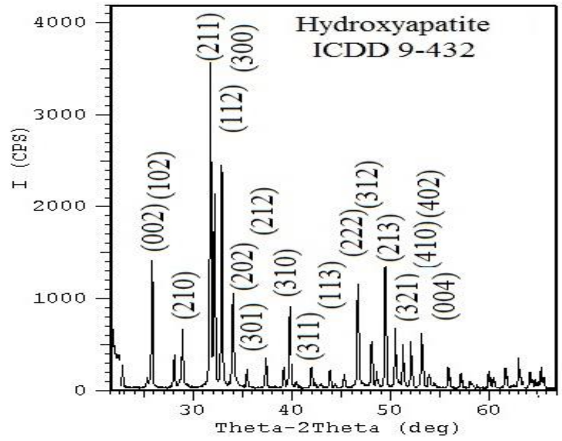

Figure 5. *XRD patterns of HA powders*

Thickness of coating layer and surface structure were obtained from the cross-sectional and surface images using a SEM-EDX (LEO 1430 VP). Fig 6 shows the morphology of HA powders. HA powders are approximately under 1 μm. Fig. 7 shows the surface morphology of the HA coating on Ti6Al4V. SEM image of coating surface is shown in Fig 7 to illustrate crack free, smooth and porous surface. SEM image of cross section is shown in Fig 8 to illustrate homogenous coating layer. Thickness of coating for HA was about 98 μm.

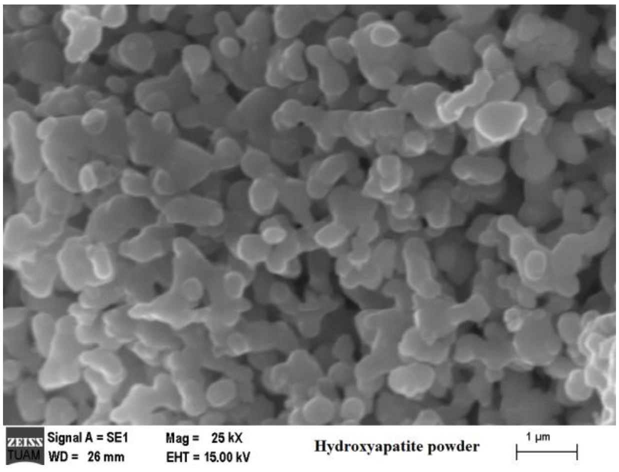

Figure 6. *SEM image of HA powders*

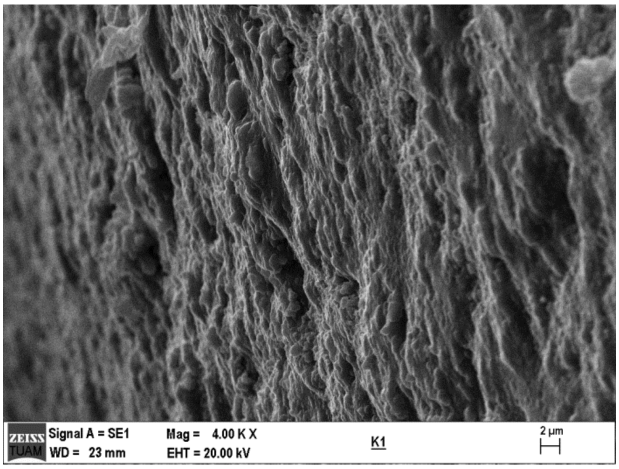

Figure 7. *SEM image of HA coating surface.*

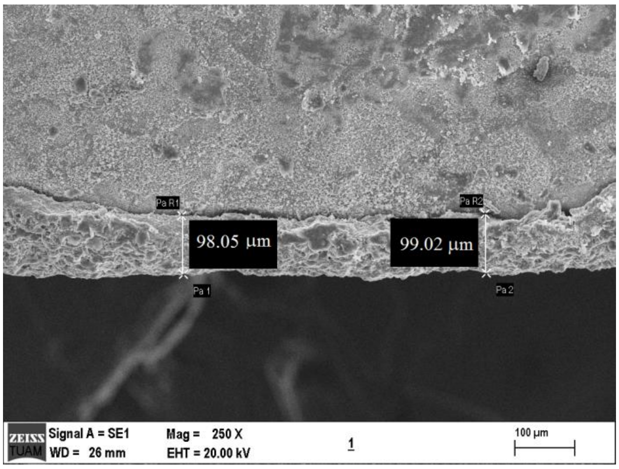

Figure 8. *SEM image of HA coating cross section.*

Table 1. *SEM-EDX analysis of HA coating surface.*

Element	Series	Net	Unn.C (wt%)	Nor. C (wt%)	Atom C (at%)
Carbon	K	19643	11.77	9.75	19.24
Oxygen	K	16174	41.41	34.28	50.79
Sodium	K	3511	2.24	1.85	1.91
Aluminium	K	6561	2.10	1.74	1.53
Silicon	K	2129	0.58	0.48	0.41
Phosphorus	K	3127	0.81	0.67	0.51
Chlorine	K	6055	1.40	1.16	0.77
Calcium	K	7716	1.69	1.40	0.83
Titanium	K	159953	57.36	47.48	23.51
Iron	K	2348	1.44	1.20	0.51
		Total	120.8	100.0	100.0

As can be seen in Table 1, Ca/P atomic ratio is 1.63. Despite the well-recognized importance of single-phase HA, however, precisely stoichiometric HA (a Ca/P ratio of exactly 1.67) is not always present.

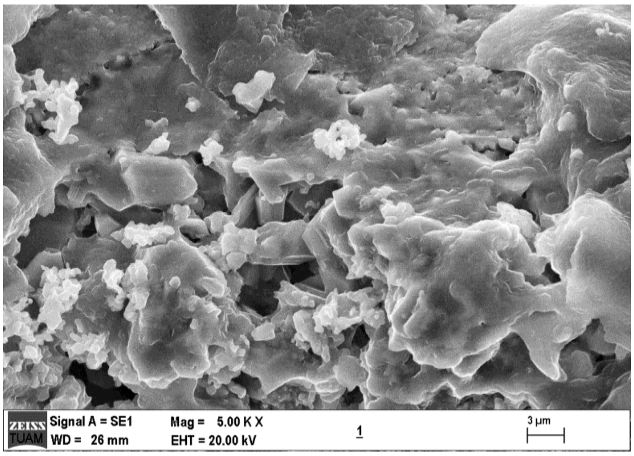

Figure 9. *SEM images of surface (after SBF solution dipping)*

In order to study the weight variety of HA coating in SBF, the dry weight of coating was measured before and after the incubation, and the percentage of weight increase (Wp) can be calculated according to the following equation (1):

$$W_p = \frac{W_b - W_a}{W_a} x100 \qquad (1)$$

Where W_b and W_a represent the weight of sample after and before soaking in SBF, respectively. The mass change of samples before and after immersing in SBF for 1, 7, 14, and 21 days was measured by using an analytical balance (accuracy: 0.1 mg). All the samples were thoroughly rinsed with distilled water and dried at 65 °C before weighing. The bio resistivity of the specimens was assessed by SBF solution. This solution was prepared according to the protocol suggested by Kokubo et al. [13,14] Then samples were weighed and characterized by SEM. As can be seen in Fig 9 new HA crystals occurred on surface. The results show that the amount of particles formed on the HA coated Ti6Al4V implant increased with the increasing of soaking time and the percentages of weight increase at immersing for 1, 7, 14 and 21 days were 1,43 % , 3,18 % , 10.40 % and 17,42 % , respectively.

4. Conclusion

In this work, sol-gel synthesized (nano sized) hydroxyapatite (HA) powders were successfully produced and used for coating Ti6Al4V implant by using sol-gel method. Experiments we have demonstrated that HA can be coated on Ti6Al4V by sol-gel method at the low temperature.

Bioactivity results showed that HA coated Ti6Al4V implants are as equally successful as HA coated implants in achieving osseointegration. Finally it can be use in biomedical application as an implant. With the increase in soaking time, the amount of new hydroxyapatite seed formed on surface increased. This was confirmed by the weight assessment and SEM images.

XRD peaks of synthesized powders completely match with the standard HA peaks.

A dense and homogeneous surface layer is expected to contribute to high adhesion strength between the HA layer and the Ti6Al4V implant. The measured coating thickness of HA on Ti6Al4V is 98 μm.

Coating surface is homogeneous and smooth.

Acknowledgement

This study has been performed within project of 15.FEN.BIL.24 under the support of Afyon Kocatepe University Scientific Research Projects Coordination Unit.
This paper presented in ”4rd International Conference on Computational and Experimental Science and Engineering (ICCESEN-2017)”

References

[1] Sam Zhang, Hydroxyapatite Coatings for Biomedical Applications, CRC Press, 2013, NewYork

[2] Andreas ¨ Ochsner and Waqar Ahmed, Biomechanics of Hard Tissues, WILEY-VCH Verlag GmbH & Co. KGaA, 2010, Weinheim

[3] F. C. M. Driessens, M. G. Boltong I. Khaïroun, E. A. P. De Maeyer, M. P. Ginebra, R. Wenz, J. A. Planell, R. M. H. Verbeeck, Applied Aspects of Calcium Phosphate Bone Cement Application, Biomaterials Engineering and Devices: Human Applications pp 253-260 doi.org/10.1007/978-1-59259-197-8_15

[4] Maria Vallet-Regi, Jose Maria Gonzalez-Calbet, Calcium phosphates as substitution of bone tissues, Progress in Solid State Chemistry 32 (2004) 1–31 doi:10.1016/j.progsolidstchem.2004.07.001

[5] http://hagans.biz/39567_a_diagram_of_a_long_bone/ 2018/08

[6] Joon Park, Biomaterials An Introduction, Springer, 2007, Iowa

[7] O. Sahin, S. Uzunoglu And E. Sahin, Influence Of Pd Addition Of Cocrmo Biomedical Alloys On The Microhardness Behaviour, ACTA PHYSICA

POLONICA A, Vol.128 (2015) B-145 DOI: 10.12693/APhysPolA.128.B-145

[8] G. Celebi Efe, M. İpek, C. Bindal and S. Zeytin, Pack Siliconizing of Ti6Al4V Alloy, ACTA PHYSICA POLONICA A, Vol 132 (2017) 760 DOI: 10.12693/APhysPolA.132.760

[9] A. Evcin, E. Arlı, Z. Baz, R. Esen, E.G. Sever, Characterization of Ag-TiO2 Powders Prepared by Sol-Gel Process, ACTA PHYSICA POLONICA A, Vol 132 (2017) 608 DOI: 10.12693/APhysPolA.132.608

[10] N. Çiçek Bezir, A. Evcin, R. Kayali, M.K. Özen, K. Esen, Comparison of Five-Layered ZrO2 and Single-Layered Ce, Eu, and Dy-Doped ZrO2 Thin Films Prepared by Sol-Gel Spin Coating Method, ACTA PHYSICA POLONICA A, Vol 132 (2017) 612 DOI: 10.12693/APhysPolA.132.612

[11] N. Çiçek Bezir, A. Evcin, R. Kayali, M.K. Özen, G. Balyaci, Comparison of Pure and Doped TiO2 Thin Films Prepared by Sol-Gel Spin-Coating Method, ACTA PHYSICA POLONICA A, Vol 132 (2017) 620 DOI: 10.12693/APhysPolA.132.620

[12] Haibo Wang, Jong-Kook Lee, Amr Moursi, John J. Lannutti, Ca/P ratio effects on the degradation of hydroxyapatite in vitro, Journal of Biomedical Materials Research Part A, Volume 67A, Issue 2, 1 November 2003, Pages 599–608 DOI: 10.1002/jbm.a.10538

[13] T. Kokubo, H. Kushitani, S. Sakka, T. Kitsugi, T. Yamamuro, Solutions able to reproduce in vivo surface-structure changes in bioactive glass–ceramic A-W, J. Biomed. Mater. Res., 24 (1990), pp. 721–734 DOI: 10.1002/jbm.820240607

[14] Y. FAN, X. LU, A study of apatite formation on natural nano-hydroxyapatite/chitosan composite in simulated body fluid, Front. Mater. Sci. China 2008, 2(1): 1–94 DOI 10.1007/s11706-008-0016-6

International Journal of Computational and Experimental Science and Engineering (IJCESEN)
Vol. 4-No.3 (2018) pp. 20-24
http://dergipark.gov.tr/ijcesen

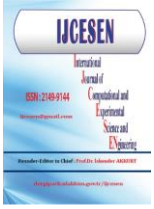

ISSN: 2149-9144

Research Article

Numerical Simulation of Casing Stress during Multi-stage Fracturing Based on Stage Finite Element Method

Xueli GUO[1*], Jun LI[1], Gonghui LIU[1, 2], and Hui YAN[1]

[1]China University of Petroleum, Beijing, The College of Petroleum Engineering, 102249, Beijing-China
[2]Beijing University of Technology, Beijing-China

* **Corresponding Author :** clouder0713@163.com
ORCID: 0000-0002-9774-799X

Article Info:

DOI: 10.22399/ijcesen.418035
Received : 24 April 2018
Accepted : 7 August 2018

Keywords :

Stage finite element method
Casing stress
Fracturing
Cement channelling
Transient temperature

Abstract:

During multi-stage hydro-fracturing operation, casing deformation issues have widely occurred in the Weiyuan-Changning National Shale Gas Demonstration Area, which dramatically reduce the productions of shale gas wells. It is important to access the influence of multiple factors on casing during fracturing operations. In this paper, a stage finite element method is presented to establish three-dimensional physical and finite element casing-cement sheath-formation (CCF) models during volume fracturing processes. It considers the influences of initial stress and displacement state at and near the wellbore. Loads from the initial stress field, fracturing pressure, and transient temperature changes are incorporated in the models. Cement channelling, cement elastic modulus, casing eccentricity, and fracturing pump rate are also the variables taken into account. Sensitivity analyses are conducted to reveal which one has the greatest influence on casing stress. The results indicate that casing stress is highly affected by cement channelling. Low casing stress can be guaranteed by high cement sheath modulus and optimal fracturing pressure. Casing transient temperature is significantly reduced by the large pump rate, then a certain thermal stress generating in the casing. Among all the factors, casing eccentricity has a minor influence on casing stress.

1. Introduction

The characteristics of geological conditions of shale formation are “poor storage environment”, “buried deep”, “severe fault structure”, “heterogeneous production layer” [1]. Horizontal well drilling and multi-stage fracturing are two key techniques for the development of shale gas [2]. During multi-stage fracturing processes, a large amount of fracturing fluids are injected into the borehole in large pump rate and high pressure [3]. High pressure and complex downhole conditions would increase the risk of casing integrity [4, 5].

From 2009 to 2016, 101 fracturing wells have been drilled by Petro-China in Weiyuan-Changning National Shale Gas Demonstration Area, including 90 horizontal wells, while 32 wells of which faced with casing deformation failure problems with 47 deformation points, shown in **Figure 1**. Wells with casing deformation failure account for 31% [6], which shown serious casing deformation failure problems during fracturing of shale gas. Finite element method is an effective way to accurately calculate casing stress in a complex downhole condition. In this paper, three-dimensional physical and finite element models of casing-cement sheath-formation (CCF) are established based on the stage finite element method. Cement channelling, cement elastic modulus, casing eccentricity, and fracturing

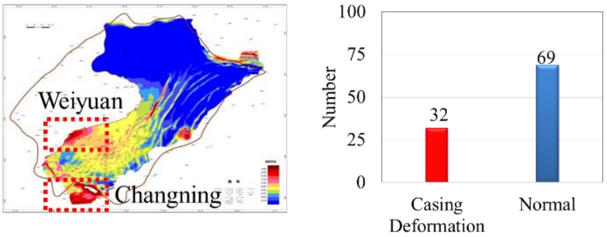

Figure 1. *Casing deformation in shale gas play*

pump rate are the variables taken in account to reveal the influences in casing deformation.

2. Model and Development

The researchers did not consider the influence of initial geo-stress, they loaded the stress directly after establishing the CCF model [7]. Only a few scholars loaded the stress in the formation before drilling, which is called stage finite element method (FEM) [8].

2.1. Stage finite element method

The whole drilling, casing, cementing, and fracturing processes are considered by the stage FEM. Before drilling, the initial stress has already existed in the formation. So it is loaded and the displacement field is zero in the formation. The rock originally occupied borehole volume. When a wellbore is drilled, it is removed, which results in stress concentration around the hole. After drilling, mud exerts some pressure-P_i on the borehole wall, which will reduce the stress concentration around the hole. After setting casing and cementing the annulus, the disturbance to the stress field still exists. During fracturing process, the casing pressure increases dramatically and the casing string is cooled, the stress disturbance around the hole will be amplified, possibly leading to the casing integrity problem. For the conventional method, the initial stresses are directly loaded in the model after drilling.

2.2. Model establishment

SLG (Solid Liquid Gas) Map can be obtained from the IBC (Isolation Scanner), shown in ***Figure 2***. Three kinds of colors represented the gas, liquid, and cement sheath, respectively. Casing deformation has occurred in 2 579 m and 2 331m, where the cement channel and casing eccentricity are serious.

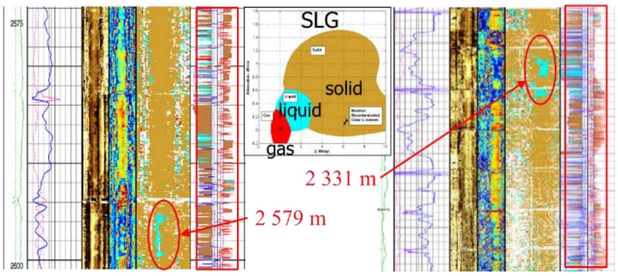

Figure 2. *SLG (Solid Liquid Gas) Map from the IBC (Isolation Scanner)*

Based on the stage FEM, a three-dimensional physical CCF model is established considering transient thermal-pressure coupling effect, shown in ***Figure 3.*** The parameters of cement channelling angle and casing eccentricity are defined as e and θ, respectively. Other factors, like pump rate-Q, fracturing pressure-P_f, and cement elastic modulus-E_c are also taken into account to investigate the influences on casing stress. The stress boundaries are σ_H, σ_h, σ_V, which represent the maximum horizontal stress, minimum horizontal stress, and vertical stress, respectively.

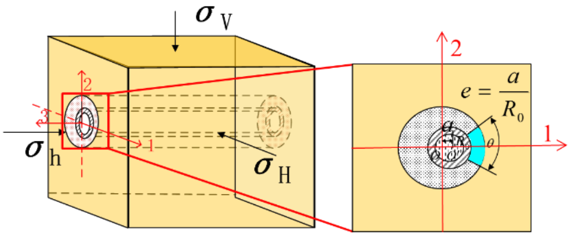

Figure 3. *Three-dimentional CCF physical model*

The finite element model is analysed using the ABAQUS finite element software to investigate the influence on casing, shown in ***Figure 4***. The geometrical dimensions of the CCF model are shown as following: the wellbore diameter is 215.9 mm, the casing diameter is 139.7 mm, and the casing thickness is 9.17 mm. According to the Saint-Venant principle, the formation boundary dimension should be 5-6 times larger than that of the well-bore geometry. In view of this, the model geometry is 2×2 m, while the corresponding wellbore diameter and axial length are 0.2159 m and 2 m, respectively. The stress boundaries are loaded using the key words *Predefined Field.

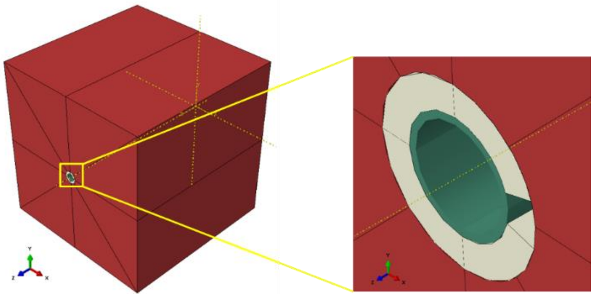

Figure 4. *Three-dimentional CCF finite element model*

2.3. Control equations

The pump rate can influence the convective heat transfer coefficient- h. When large amounts of fracturing fluids are injected into the wellbore, they are usually in a turbulent state. The transient heat transfer model is shown in ***Figure 5***. Heat transfer coefficient between the fracturing fluid and the inner casing wall can be calculated using Marshall Model, shown in **Eq**. (1). [9]

$$h = 0.0107\frac{k_m}{D}\square\left\{\rho D_{eff}\frac{4Q}{\pi D^2}\Big/\left[K\left(\frac{3n+1}{4n}\right)^n\left(\frac{8Q}{15\pi D^3}\right)^{n-1}\right]\right\}^{0.67} \square\left[K\left(\frac{3n+1}{4n}\right)^n\left(\frac{8Q}{15\pi D^3}\right)^{n-1}C_m\Big/k_m\right]^{0.33} \quad (1)$$

Where h is the heat transfer coefficient, $W\cdot m^{-2}\cdot °C^{-1}$; D is the pipe diameter in calculation, m; D_{eff} is the equivalent diameter, m; ρ is the drilling mud density, kg·m^{-3};$\mu_{w,app}$ is the apparent viscosity, Pa·s; Q is the fracturing pump rate, m^3·min^{-1}; C_m is the fluid specific heat capacity, J·kg^{-1}·°C^1; n is the fluid rheological index, for fracturing fluid n<1; K is the fluid consistency coefficient, Pa·s^{-n}.

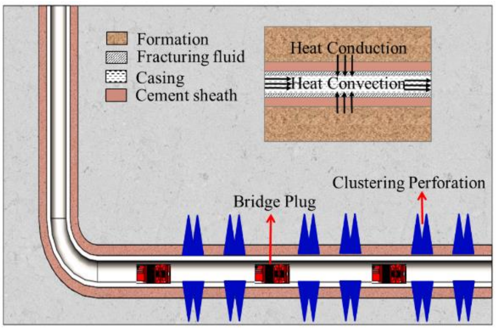

Figure 5. *The transient heat transfer process*

For the CCF model, the solution of unidimensional time-dependent equation in cylindrical geometry, the heat transfer equation, is obtained as time-dependent temperature distribution by ***Eq***. (2). [10-12]

$$k_i\left(\frac{\partial^2 T^i}{\partial z^2}+\frac{\partial^2 T^i}{\partial r^2}+\frac{1}{r}\frac{\partial T^i}{\partial r}\right)+q_i=C_{pi}\rho_i\frac{\partial T^i}{\partial t} \qquad (2)$$

where k_i is the coefficient of thermal conductivity, W·m^{-1}·°C^1; C_{pi} is the specific heat capacity, J·kg^{-1}·°C^1; ρ_i is the density, kg·m^{-3}; q_i is The heat source density, W·m^{-3}; T^i is the thermal field, °C; i=1, 2, 3, is represented the casing, cement sheath, and formation, respectively; t is the time, s; r is the radius of the CCF model, m.

After calculating the thermal field, the stress of CCF under thermal-pressure coupling in cylindrical geometry can be obtained by ***Eq***. (3).

$$\boldsymbol{\varepsilon} = \mathbf{D}\boldsymbol{\sigma} \qquad (3)$$

where **ε** is the strain array under the condition of thermal-pressure coupling; **σ** is the stress matrix; **D** is the elastic matrix.

Shale formation contains numerous inherent bedding planes [13], so it can be seen as the transverse isotropy material. **D** can be written by:

$$\mathbf{D}=\begin{bmatrix} 1/E_1 & -\mu_1/E_1 & -\mu_2/E_2 & 0 & 0 & 0 \\ -\mu_1/E_1 & 1/E_1 & -\mu_2/E_2 & 0 & 0 & 0 \\ -\mu_2/E_2 & -\mu_2/E_2 & 1/E_2 & 0 & 0 & 0 \\ 0 & 0 & 0 & G_2 & 0 & 0 \\ 0 & 0 & 0 & 0 & G_2 & 0 \\ 0 & 0 & 0 & 0 & 0 & G_1 \end{bmatrix} \qquad (4)$$

where E_i is the elastic modulus, GPa; G_i is the shear modulus, GPa; μ_i is the Poisson's ratio; $G_1=E_1/2(1+\mu_1)$; $G_2=E_1E_2/(E_1+E_2+2\mu_2E_2)$; i=1,2 represent the parameters of parallel and vertical shale bedding.

2.4. Parameter setting

The internal casing pressure is obtained from the pump pressure plus the hydrostatic fluid pressure downhole. The external boundary stress is the geo-stress of shale reservoir. Taken different pump rates, cement channelling angles, casing eccentricities, fracturing pressures, and cement moduli into consideration, the casing stresses are calculated to reveal which factor is the most important for casing deformation.

Unless otherwise mentioned, the applied maximum horizontal stress σ_H is 82 MPa, the minimum horizontal stress σ_h is 55 MPa, the vertical stress σ_v is 57 MPa, the formation temperature $T_\infty{}^3$ is 100 ℃, and the fluid temperature T_a is 20 ℃. The thermal and mechanical properties of different materials are presented in ***Table 1.***

Table 1. *Thermal and mechanical properties*

Parameters	**Casing**	**Cement Sheath**	**Formation**	**Fluid**
Elastic Modulus E_i/ (GPa)	210	10	22-40	-
Poisson's ratio μ_i	0.3	0.15	0.23	-
Coefficient of Thermal Expansion α_i/(10^{-5}·℃$^{-1}$)	1.06	1.0	1.02	-
Coefficient of Thermal Conductivity k_i /(W·m^{-1}·℃$^{-1}$)	58.2	1.74	1.0	1.73
Specific Heat Capacity C_i / (J·Kg^{-1}·℃$^{-1}$)	460	1830	1043	4200
Density ρ_i / (kg·m^{-3})	7850	1800	2500	1000

3. Results and Analysis

3.1. Transient temperature and stress

A total of 5 simulations were performed to investigate numerically the transient temperature and stress of casing during fracturing process. Simulations were conducted using ABAQUS program. The pump rates were set as 0/1/3/16 m^3/min. The results are shown in ***Figure.7***. It is seen that the downhole temperature would drop dramatically in a few minutes when the pump rate is larger than 3 m^3/min, while casing stress increases dramatically. If there is no thermal transferring, temperature will be in the same and the stress will increase linearly. The larger the pump rate, the lower the downhole temperatures and the higher the casing stress.

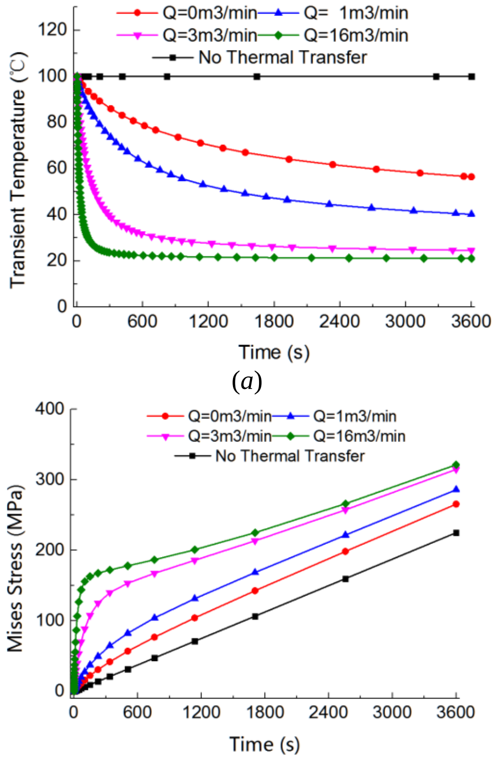

(*a*)

(*b*)

Figure 6. *The Influence of Pump Rate on Casing. (a) Transient Temperature. (b) Transient Mises Stress.*

3.2. The Influence of Different Factors on Casing Stress

Using the thermal-pressure coupling model, simulations for different cement channelling-θ, cement sheath elastic moduli-E, casing eccentricity-e, and fracturing pressure-P_m are conducted to investigate the influences on casing stress. The results are shown in ***Figure 7***.

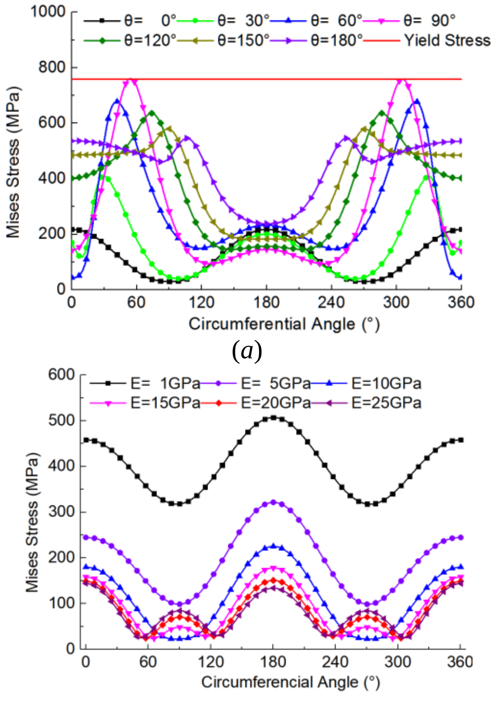

(*a*)

(*b*)

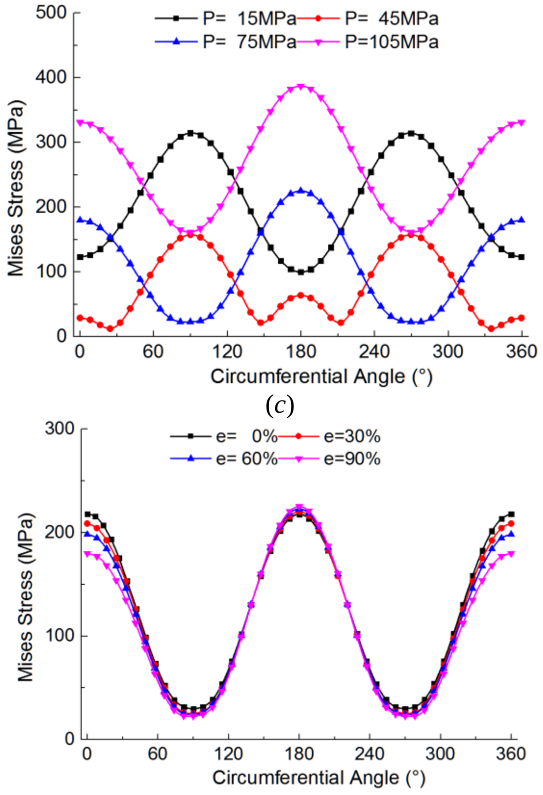

(*c*)

(*d*)

Figure 7. *The Influence of Different Factors on Casing Stress (a) Cement Channelling. (b) Cement Modulus. (c) Fracturing Pressure. (d) Casing Eccentricity.*

Figure 7 (a) shows that the casing stress will increase dramatically with the increasing of θ. For the casing of P110 steel grade, the yield stress is 758MPa, shown as the red line. The largest Von Mises stress of casing 750MPa appears at the angle of 90°, which is almost close to the yield stress. The risk of casing failure is very high. ***Figure 7*** (b) shows that the lower the cement modulus, the higher the casing stress. When the cement modulus is larger than that of formation-22GPa, the stress could hardly decrease. ***Figure 7*** (c) shows that lower and higher pressure can increase the casing stress. Obviously, suitable pressure can guarantee a low casing stress. ***Figure 7*** (d) shows that no matter how serious casing eccentricity is, casing stress is almost the same. The casing eccentricity has minor influence on casing stress.

3.3. Comparison of different factors

The maximum stresses of each factor are presented in ***Figure 8***. It is seen that the cement channel has the greatest influence on casing stress, while the casing eccentricity has the least influence on casing stress. Cement modulus, fracturing pressure, and pump rate have some influences on casing stress.

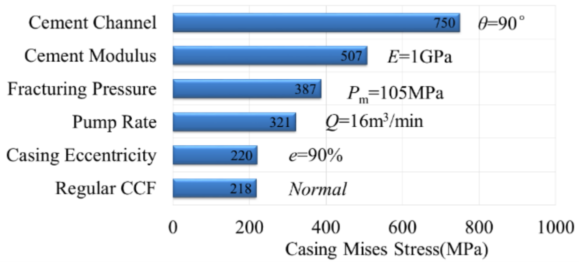

Figure 8. *The Maximum of Mises Stress of Different Factors*

4. Conclusions

Based on stage finite element method, three-dimensional transient thermal-pressure CCF models are established. The effects of different factors on casing stress are conducted to reveal which one has the greatest influence on casing stress. Conclusions can be drawn from the former analyses results.

(1) Casing stress can dramatically increase with the increasing of cement channelling. The largest casing Mises stress-750 MPa appears at the channelling angle of 90°, which is almost the same as the yield stress.

(2) Large cement sheath modulus, optimal fracturing pressure can guarantee a lower casing stress.

(3) The transient temperature drops dramatically with the increase of pump rate, leading to a certain thermal stress. Casing eccentricity has a minimum influence on casing stress.

Acknowledgement

Authors thanks to Dassault Systemes Simulia Corparation for providing ABAQUS software program. This paper was supported by the National Natural Science Foundation, Project No. 51674272, and China Petroleum & Chemical Corporation, Project No. HX20180001.

This paper was presented in "4rd International Conference on Computational and Experimental Science and Engineering (ICCESEN-2017)"

References

[1] Lv Z., Wang L., Deng S., et al. China Shale Gas Exploration: Early Sichuan Basin Longmaxi Shale Gas Stimulation and Completion Case Study, SPE/IADC Middle East Drilling Technology Conference & Exhibition. Society of Petroleum Engineers, Dubai 2013, DOI:10.2118/166746-MS.

[2] Sugden C., Johnson J., Chambers M., et al. Special Considerations in the Design Optimization of High Rate, Multistage Fractured Shale Wells, IADC/SPE Drilling Conference and Exhibition. Society of Petroleum Engineers, San Diego ,2012, DOI:10.2118/151470-MS.

[3] Zhou C., Wu X., Li H., et al. Influence of In-situ Stress Distribution on Selection of Fracturing Fluid Backflow Technology, Acta Physica Polonica A, 130(2016) 347-351. DOI: 10.12693/APhysPolA.130.347.

[4] Davies R. J., Almond S., Ward R. S., et al. Oil and gas wells and their integrity: Implications for shale and unconventional resource exploitation, Marine and Petroleum Geology, 56(2014) 239-254. DOI:10.1016/j.marpetgeo.2014.03.001.

[5] Rocha-Valadez T., Mentzer R. A., Hasan A. R., et al. Inherently safer sustained casing pressure testing for well integrity evaluation, Journal of Loss Prevention in the Process Industries, 29(2014) 209-215, DOI:10.1016/j.jlp.2014.02.012.

[6] Yan W., Zou L., Li H., et al. Investigation of Casing Deformation during Hydraulic Fracturing in High Geo-stress Shale Gas Play, Journal of Petroleum Science and Engineering, 150(2016) 22-29, DOI: 10.1016/j.petrol.2016.11.007.

[7] Lin T., Yu H., Lian Z., et al. Numerical simulation of the influence of stimulated reservoir volume on in-situ stress field, Journal of Natural Gas Science and Engineering, 36(2016) 1228-1238, DOI: 10.1016/j.jngse.2016.03.040.

[8] Zhang, W., Eckert, A., Liu, X. Numerical Simulation of Micro-Annuli Generation by Thermal Cycling. 51st U.S. Rock Mechanics/Geomechanics Symposium, American Rock Mechanics Association. San Francisco, 2017. ID: ARMA-2017-0354.

[9] B. Nagy, International Conference on Computational and Experimental Science and Engineering (ICCESEN 2014), 25-29 October, 2014 Antalya-Turkey. DOI: 10.12693/APhysPolA.128.B-314.

[10] M. Koru and O. Serçe. Experimental and Numerical Determination of Casting-Mold Interfacial Heat Transfer Coefficient in the High Pressure Die Casting of A-360 Aluminum Alloy 130(2016) 453-458. DOI: 10.12693/APhysPolA.130.453.

[11] F. Kulalı, I. Akkurt, N. Özgür, International Conference on Computational and Experimental Science and Engineering (ICCESEN 2015), 14-19 October, 2015 Antalya-Turkey. DOI: 10.12693/APhysPolA.130.496.

[12] O. Ipek, M. Kan, B. Gurel, International Conference on Computational and Experimental Science and Engineering (ICCESEN 2015), 14-19 October, 2015 Antalya-Turkey. DOI: 10.12693/APhysPolA.132.580.

[13] Gao C, Xie L Z, Xie H P, et al. 2017. Estimation of the equivalent elastic modulus in shale formation: Theoretical model and experiment[J]. Journal of Petroleum Science and Engineering, 151:468-479. DOI: 10.1016/j.petrol.2016.12.002.

International Journal of Computational and Experimental Science and Engineering
(IJCESEN)
Vol. 4-No.3 (2018) pp. 25-29
http://dergipark.gov.tr/ijcesen

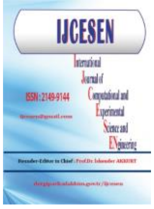

ISSN: 2149-9144

Research Article

Study on Performance of Progressing Cavity Pumps (PCPs) in Different Fit Modes

Lei ZHENG[1*], Xiaodong WU[1], Ruidong ZHAO[2], Huachang LI[3] and Mengyun LIU[1]

[1]MOE Key Laboratory of Petroleum Engineering, China University of Petroleum (Beijing), 102249, Beijing-China
[2]Research Institute of Petroleum Exploration ＆ Development, CNPC, 100083, Beijing-China
[3]Sinopec International Petroleum Service Corporation, 100020, Beijing-China

* **Corresponding Author** : sydxzhenglei@163.com
ORCID: 0000-0003-4774-2071

Article Info:

DOI: 10.22399/ijcesen.474462
Received : 24 October 2018
Accepted : 7 November 2018

Keywords

Progressing cavity pump
Fit parameter
Volumetric characteristics
Power consumption
Work efficiency

Abstract:

The performance of progressing cavity pumps（PCPs）is significantly different in different fit modes between the stators and rotors，such as interference fit for conventional PCPs with rubber stators and clearance fit for novel all metal PCPs. In order to study the influence of fit modes on PCP performance, a novel concept of the fit parameter is introduced to quantitatively describe the fit condition. Based on working principles of PCPs, comprehensive studies are carried out on the pump performance in different fit modes, including the volumetric characteristics, power consumption and work efficiency. The results show that the theoretical pump rate slightly decreases with the increase of the fit parameter. Though there is obvious friction inside the pump and the interference has a great impact on the power consumption, the PCP in interference fit is able to achieve high volumetric efficiency (>80%). Though there is inevitable leakage and the clearance has a significant influence on the flow rate, the PCP in clearance fit can reach high mechanical efficiency (>90%). The novel all metal PCP in clearance fit has enormous potential for development owing to its good overall performance.

1. Introduction

The progressing cavity pump (PCP) has been widely used as an effective artificial lift method in the oil field development, which shows significant advantages, such as low cost, easy installation, high efficiency and adaptation to complex working conditions. But there are still some deficiencies in resisting wear and temperature for conventional PCP, which operates with the rubber stator and metallic rotor in interference fit. Now a new type of all metal PCP in clearance fit has been developed to overcome these limitations [1], in which both the stator and rotor are made of metallic materials. Therefore, the fit modes of PCPs become more diversified and not limited to the traditional interference fit. Many studies have been conducted on the performance of conventional PCPs in interference fit and all metal PCP in clearance fit respectively [2-5], indicating that results are significantly different. However, there is still a lack of studies on the PCP performance based on the fit condition between the stator and rotor, namely considering different fit modes comprehensively.

In this paper, a fit parameter is introduced to study the PCP performance in consideration of fit modes. The conventional PCP and all metal PCP are taken as typical examples to analyze the relationship between the performance and fit parameter. This study can provide a theoretical basis for the PCP design and the choice of PCP types in the oil field application.

2. PCPs in Different Fit Modes

2.1. Basic Structure

As shown in Figure 1, the fit modes of PCP mainly depend on the relative size of its stator and rotor, which can be defined by a new parameter, given as:

$$\delta = \frac{d_r - d_s}{2} \quad (1)$$

Where δ is the fit parameter, m; d_r is the rotor diameter, m; d_s is the stator diameter, m.

Therefore, the case of $\delta=0$ represents the exact fit (Figure 1a), which rarely exists in actual situations; the case of $\delta>0$ represents the interference fit (Figure 1b); the case of $\delta<0$ represents the clearance fit (Figure 1c). It is notable that the red section in each figure is the flow cross-sectional area during PCP operation of pumping fluid.

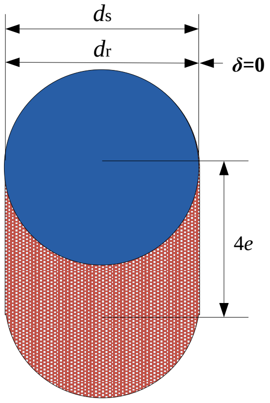

(a) Exact fit

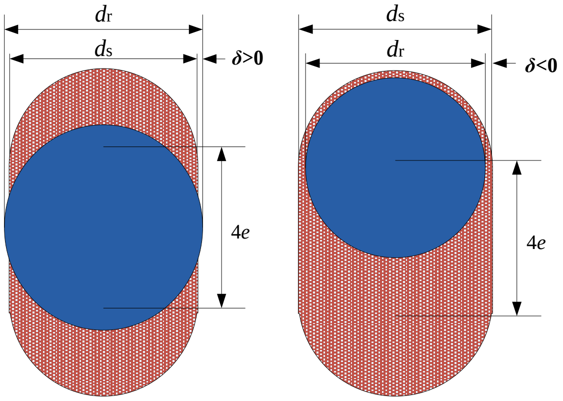

(b) Interference fit (c) Clearance fit

Figure 1. *Different fit modes between stator and rotor*

Considering the influence of the fit parameter on the flow rate inside the pump, the flow cross-sectional area in different fit modes can be calculated as:

$$A = \begin{cases} 4ed_r, \delta = 0 \\ 2\left[\frac{d_r^{\,2}}{4}\arcsin\left(\frac{2\sqrt{\delta d_r - \delta^2}}{d_r}\right) - \sqrt{\delta d_r - \delta^2}\cdot\left(\frac{d_r}{2} - \delta\right)\right] \\ +4ed_r - 8e\delta - \pi(\delta d_r - \delta^2), \delta > 0 \\ 4ed_r - 8e\delta - \pi(\delta d_r - \delta^2), \delta < 0 \end{cases} \quad (2)$$

Where e is the pump eccentricity, m.

Then the theoretical pump rate can be calculated as:

$$Q_t = 1440nAT \quad (3)$$

Where n is the rotational speed, r/min; T is the stator pitch, m.

2.2. Working Principles

The PCP body is divided into several cavities by the mutual meshing movements of the stator and rotor during the pump operation. Each cavity moves spirally from the inlet to the outlet along the pump, realizing the process of fluid pressurizing and lifting. For the PCP in interference fit, these cavities can be well sealed and little leakage occurs at relatively low lifting pressure, in which the flow rate is approximately equal to the theoretical pump rate. But when the lifting pressure becomes higher than the pressure-bearing limit corresponding to the interference, the rubber stator can be penetrated and the leakage flow occurs [6]. For the PCP in clearance fit, cavities along the pump connect with each other and fluid leakage exists objectively during the pump operation. However, the lifting capacity can be ensured by the viscous resistance of the fluid, which has a certain sealing effect on the leakage flow in the clearance between the stator and rotor.

3. Performance Analysis

3.1. Volumetric Characteristics

Based on the working principles mentioned above, the leakage characteristics of PCPs are closely related with the fit modes, which can influence the volumetric characteristics significantly [7]. The actual flow rate can be obtained by subtracting the leakage from the theoretical pump rate, given as:

$$Q = Q_t - q \quad (4)$$

Where Q is the actual flow rate, m^3/d; q is the leakage, m^3/d.

For PCPs in interference fit, the pressure-bearing limit depends on the pump structure and working conditions, which can be obtain by experimental analysis [3], given as:

$$\Delta p_k = kn^{0.25}t^{0.21}\mu^{0.08}\delta Z, \delta > 0 \quad (5)$$

Where k is a constant related with the stator property, which is 0.12 for the stator made of acrylonitrile-butadiene Rubber (NBR)[3]; t is the operating temperature, ℃; μ is the fluid viscosity, mPa·s; Z is the number of pump stages.

Then the volumetric efficiency of PCPs in interference fit can be calculated by the following empirical formula as [3]:

$$\eta_v = \begin{cases} 1 - \frac{\alpha}{\Delta P_k}\Delta p, \Delta p \le \Delta p_k \\ 1 - \alpha - 0.015\left(\Delta p - \Delta p_k\right)^{\beta}, \Delta p > \Delta p_k \end{cases}, \delta > 0 \quad (6)$$

Where Δp is the total lifting pressure, MPa; α is a constant determined by the stator, which is 0.05 for the NBR stator; β is a constant related with pump geometrical parameters.

For PCPs in clearance fit, the pressure increases approximately linearly from the inlet cavity to the outlet cavity during the pump operation [8]. According to the clearance flow theory [9], the fluid leakage caused by differential pressure in the clearance can be expressed as:

$$q = k\frac{(-\delta)^3 \Delta p}{12\mu Z}, \delta < 0 \tag{7}$$

Where q is the leakage, m^3/d; k is a constant related with the clearance structure, which is equal to the ratio of the clearance width to the clearance length; $\Delta p/Z$ is equal to the single-stage pressure difference, MPa.

Then the volumetric efficiency of PCPs in clearance fit can be calculated as:

$$\begin{aligned}\eta_{\mathrm{v}} &= \frac{Q_{\mathrm{t}} - q}{Q_{\mathrm{t}}} \\ &= 1 - \frac{k(-\delta)^3}{17280\mu nTZ\left[4ed_{\mathrm{r}} - 8e\delta - \pi(\delta d_{\mathrm{r}} - \delta^2)\right]}\Delta p, \delta < 0\end{aligned} \tag{8}$$

3.2. Power Consumption

During working of PCPs in different fit modes, the total power consumption can be generally reflected by the shaft power, which mainly consists of the theoretical hydraulic power and the frictional loss power. The former power is linear to the lifting pressure, while the latter power is closely related with the frictional condition between the stator and rotor inside the pump [10]. Therefore, the total power consumption can be given as:

$$P = P_{\mathrm{u,th}} + P_{\mathrm{f}} = (P_{\mathrm{u}} + P_{\mathrm{s}}) + P_{\mathrm{f}} \tag{9}$$

$$P_{\mathrm{u}} = \frac{Q \cdot \Delta p}{86.4} \tag{10}$$

$$P_{\mathrm{s}} = \frac{q \cdot \Delta p}{86.4} \tag{11}$$

Where P is the total power consumption, kW; $P_{\mathrm{u,th}}$ is the theoretical hydraulic power, kW; P_{u} and P_{s} are respectively the active power and the leakage loss power, kW; P_{f} is the frictional loss power, kW.

The hydraulic power (such as P_{u} and P_{s}) is corresponding to the volumetric characteristics mentioned above. The frictional loss power is comprehensively influenced by the fit modes and other operating parameters. Among them, the fit parameter can directly determine the frictional force between the stator and rotor. Due to the computational complexity of the frictional loss power [11, 12], it can be obtained by the regression analysis of experimental data of PCPs in different fit modes [5, 13].

3.3. Work Efficiency

The total efficiency of PCPs in different fit modes is the ratio of the active power to the shaft power, which also equals to the product of the volumetric efficiency and the mechanical efficiency [14], given as:

$$\eta = \frac{P_{\mathrm{u}}}{P} = \eta_{\mathrm{v}} \cdot \eta_{\mathrm{m}} \tag{12}$$

$$\eta_{\mathrm{m}} = 1 - \frac{P_{\mathrm{f}}}{P} \tag{13}$$

Where η_{m} is the mechanical efficiency.

4. Results and discussion

Based on the mathematical analyses above, a simulator can be developed to model the PCP performance in different fit modes using Visual Basic for Application (VBA). The conventional PCP with NBR stator and all metal PCP are respectively taken as examples to simulate the pump performance and analyze the relationship between the fit parameter and pump performance. The basic geometrical parameters and lifting parameters of two PCPs are designed to be the same except the fit parameter, as shown in Table1.

Table 1. *Basic parameters of PCPs*

Variable	**Value**
Stage number	20
Rotor diameter, mm	50
Stator pitch, mm	160
Eccentricity, mm	5
Fluid viscosity, mPa·s	40
Temperature, ℃	55
Lifting pressure, MPa	8
Rotational speed, r/min	120

The fit condition between the stator and rotor can be quantitatively described by the fit parameter δ. The positive range (δ>0) corresponds to the interference fit for the conventional PCP, in which the bigger the fit parameter is, the larger the interference will be. The negative range (δ<0) corresponds to the clearance fit for all mental PCP, in which the bigger the fit parameter is, the smaller the clearance will be. As the exact fit mode rarely exists, the relationship curve of the fit parameter and the pump performance is not continuous at the point of δ=0.

The volumetric characteristics based on the fit condition between the stator and rotor are simulated, as shown in Figure 2. Results show that, with the increase of the fit parameter, both the theoretical pump rate and fluid leakage decrease in different fit modes. For PCPs in interference fit (δ>0), the extreme interference value is 0.323mm corresponding to the pressure-bearing limit, which means the pump cavities are penetrated and the leakage flow happens when δ ranges from 0 to 0.323mm. When δ is above 0.323mm, the pump can operate normally. It is the reason why the actual flow rate firstly increases and then decreases with the increase of the fit parameter. For PCPs in clearance fit (δ<0), due to the leakage flow in the clearance, the fit parameter has a significant influence on the flow rate. When δ increases from -0.3mm to -0.05mm, the fluid leakage decreases rapidly from 17.52m^3/d to 5.64m^3/d, and the corresponding actual rate increases rapidly by 89.3%.

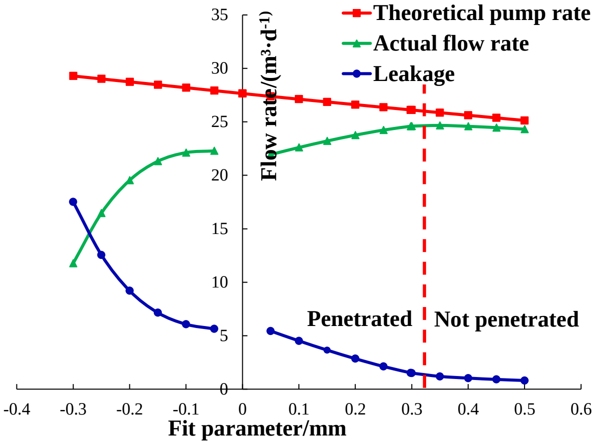

Figure 2. *Relationship between volumetric characteristics and fit parameter*

The power consumption based on the fit condition between the stator and rotor is simulated, as shown in Figure 3. The total power consumption increases with the increase of the fit parameter, and it needs to be noted that the total power consumption in interference fit (δ>0) is much larger than that in clearance fit (δ<0). It is mainly determined by the fact that the friction situation between the stator and rotor is positively correlated with the interference value. For the cases of both two fit modes, with the increase of the fit parameter, the active power increases and the leakage loss power decreases. Besides, results show that the influence of the fit parameter on the hydraulic power (P_u and P_s) in clearance fit is obviously greater than that in interference fit. The work efficiency based on the fit condition between the stator and rotor is simulated, as shown in Figure 4. For PCPs in clearance fit (δ<0), with the increase of the fit parameter, the volumetric efficiency increases rapidly, while the mechanical efficiency decreases slowly and keeps at a relatively high level. As a result, the total efficiency increases rapidly at beginning and then the increment becomes gentle, indicating more seriously affected by the volumetric performance. According to this rule, an optimum clearance can be designed for the PCP in clearance fit under certain

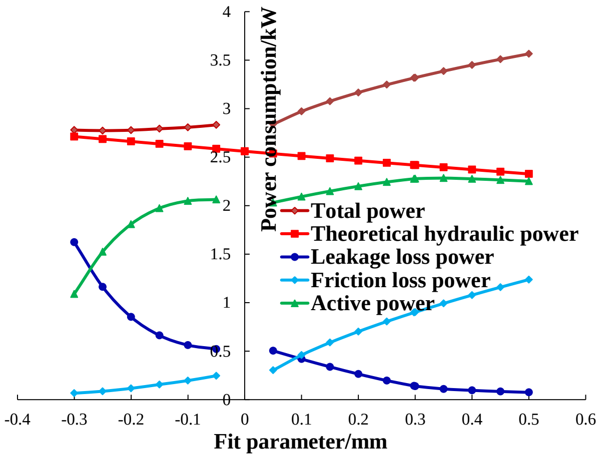

Figure 3. *Relationship between power consumption and fit parameter*

operating conditions. For PCPs in interference fit (δ>0), it can realize much higher and more stable volumetric efficiency, especially under the condition where the rubber stator is not penetrated. Combining the negative effect of the fit parameter on the mechanical efficiency, the total pump efficiency presents a decline trend. On the whole, results illustrate that PCPs in interference fit can achieve the volume efficiency above 80% (even above 90% during normal operating); PCPs in clearance fit can achieve the mechanical efficiency above 80%, and can realize higher total efficiency with an appropriate design for the fit clearance. Therefore, the novel all metal PCP also has great potential to be developed, which can be regarded as a good alternative pump for pumping fluid.

5. Conclusions

The fit mode between the stator and rotor has a significant influence on the PCP performance, including the volumetric characteristics, power consumption and work efficiency. The fit parameter can be used to describe the fit condition quantitatively and analyze the PCP performance in different fit modes. The relationship between the PCP performance and the fit parameter has been simulated comprehensively in consideration of various fit conditions. The results show that, as the fit parameter varies, the volumetric efficiency and mechanical efficiency of the PCP in a specific fit mode change in opposite trends. By contrastive analyses, the conventional PCP in interference fit is able to achieve better volumetric characteristic, while the novel all metal PCP in clearance fit can ensure greater mechanical characteristic. It indicates the PCP in clearance fit is also feasible to pump fluid, which can be regarded as an additional facility to the conventional PCPs.

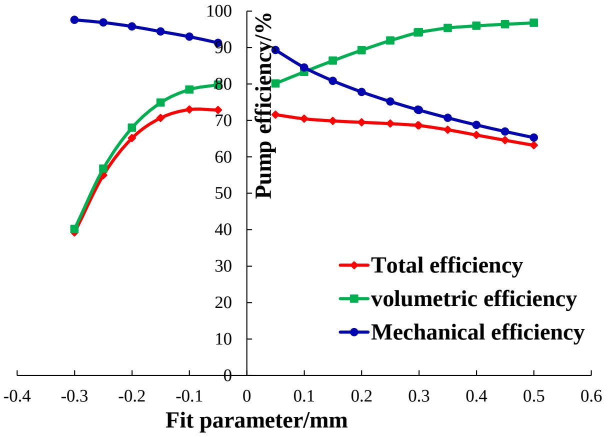

Figure 4. *Relationship between work efficiency and fit parameter*

Remarkably, during the real production of the artificial lift, the novel all metal PCP is more preferable to be used considering its long operating life and high temperature resistance.

Acknowledgement

Authors thanks to the National Science and Technology Major Project (NSTMP) Program (grant number: 2017ZX05072006-002) and the National Science and Technology Major Project (NSTMP) Program (grant number: 2017ZX05009-003) in China.

This paper was presented in “4rd International Conference on Computational and Experimental Science and Engineering (ICCESEN-2017)”

References

[1] J.L. Beauquin, F.O. Ndinemenu, G. Chalier, L. Lemay, L. Seince, A. Damnjanovic. World's first metal PCP SAGD field test shows promising artificial-lift technology for heavy-oil hot production: Joslyn field case. SPE annual technical conference and exhibition, Society of Petroleum Engineers, Anaheim 2007, ID: SPE-110479-MS.

[2] Y. Wang, X. Du. Effect of rotate speed test and temperature for hydraulic characteristic of PCP. Oil Field Equipment, 4, 40 (2011).

[3] J. Wei, W. Wu, Y. Zeng, J. Guo, F. Lin. Numerical simulation and application of performance characteristics of progressive cavity pump. Oil Drilling & Production Technology, 4, 28 (2006).

[4] J. Gamboa, A. Olivet, S. Espin. New approach for modeling progressive cavity pumps performance. SPE annual technical conference and exhibition, Society of Petroleum Engineers, Denver 2003, ID: SPE-84137-MS.

[5] J. L. Beauquin, C. Boireau, L. Lemay, L. Seince. Development status of a metal progressing cavity pump for heavy oil and hot production wells. SPE international thermal operations and heavy oil symposium, Society of Petroleum Engineers, Calgary 2005, ID: SPE- 97796-MS.

[6] F. Zegrar, S. Boucetta, B. Othmani. High pressure behavior of elastic and mechanical properties of NiGa intermetallic compound. International Conference on Computational and Experimental Science and Engineering (ICCESEN 2015), Antalya 2015. DOI: 10.12693/APhysPolA.130.471.

[7] C. Zhou, X. Wu, H. Li, Z. Ren, Y. Xin. Influence of in-situ stress distribution on selection of fracturing fluid backflow technology. International Conference on Computational and Experimental Science and Engineering (ICCESEN 2015), Antalya 2015. DOI: 10.12693/APhysPolA.130.347.

[8] S.F. Andrade, J. Valrio, M. Carvalho. Asymptotic model of the 3D flow in a progressing-cavity pump. SPE Journal, 2, 16(2011), ID: SPE-142294-PA.

[9] G. Vetter, W. Wirth, H. Korner, S. Pregler. Multiphase pumping with twin-screw pumps-understand and model hydrodynamics and hydroabrasive wear. Proceedings of the 17th international pump users symposium, Houston 2000.

[10] R. Kiliç. Determination of imbalance problem in electric motor and centrifugal pump by vibration analysis. International Conference on Computational and Experimental Science and Engineering (ICCESEN 2015), Antalya 2015. DOI: 10.12693/APhysPolA.130.487.

[11] N. Ozsoy, M. Ozsoy, A. Mimaroglu. Influence of parameters on tribological behaviour of E-Glass fiber reinforced epoxy composites. International Conference on Computational and Experimental Science and Engineering (ICCESEN 2015), Antalya 2015. DOI: 10.12693/APhysPolA.128.B-55.

[12] O. Boubaker, B. Said. Investigation on mechanical properties of Mn_3Sb intermetallic compound. International Conference on Computational and Experimental Science and Engineering (ICCESEN 2015), Antalya 2015. DOI: 10.12693/APhysPolA.130.33.

[13] J. Wei, G Shi. Rod string torque calculation of progressive cavity pump. China Petroleum Machinery, 9, 23 (1995).

[14] Y. Lv, X. Wu, Y. Li, Q. Wang. Progressing cavity pump well system efficiency analysis model and its application. Oil Drilling & Production Technology, 1, 28 (2006).

International Journal of Computational and Experimental Science and Engineering
(IJCESEN)
Vol. 4-No.3 (2018) pp. 30-33
http://dergipark.gov.tr/ijcesen

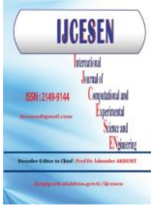

ISSN: 2149-9144

Research Article

Effect of Stress Sensitivity on Production of Tight Heterogeneous Reservoir

Nai CAO, Hong LI，Mengyun LIU*

Department of Petroleum Engineering, China University of Petroleum (Beijing), 102249, Beijing-China

* **Corresponding Author :** star_lmy@vip.163.com
ORCID: 0000-0003-3396-7552

Article Info:

DOI: 10.22399/ijcesen.444575
Received : 17 July 2018
Accepted : 16 November 2018

Keywords

Tight reservoirs
Stress sensitivity
Heterogeneity
Production analysis

Abstract:

Permeability can be effected by many factors including effective stress, and this will further impact the final production of oil and gas. In this work, a stress-dependent permeability calculation model was adopted and based on which a production function for heterogeneous tight sandstone reservoir on core scale is derived. Stress sensitivity has been taken as the primary influencing factor to analysis the impact of effective stress on the productivity of heterogeneous tight sandstone reservoir. The results shows that the stress sensitivity needed to be taken into cosideration when the effective stress cannot be overlooked in the design of developing plan for tight reservoirs; and the severity of the heterogeneity has a noticeable influence on the production.

1. Introduction

Heterogeneous tight reservoirs are important target areas for oil and gas exploration, many researches on the relationship between reservoir physical parameters and effective stress has been conducted with a large number of experiments[1-3]. The strong heterogeneity of tight reservoirs affects the variation of permeability, leading to different extents of stress sensitivity. Permeability is an important parameter in the calculation of production, meaning the stress sensitivity of heterogeneous reservoirs has an effect on production. It is significant for the development of tight heterogeneous reservoirs to calculate the production considering stress sensitivity. Many scholars have theoretically studied the law of stress sensitivity of permeability. Liu et al studied the variation of porosity and permeability of low permeability reservoirs with effective stress by the model of variable diameter capillary bundle [4]. Based on the characteristics of rock pore structure and particle contact deformation, Dong et al quantitatively analyzed the stress sensitivity of tight sandstone [5]. Wang et al analyzed the stress sensitivity of low permeability reservoir using the model of unequal diameter circuitous capillary bundle according to the theory of elastic mechanical thick wall tube [6]. However, most of the studies were deduced under homogeneous conditions, rather than heterogeneous conditions [7-8]. Therefore, in this paper, the production equation was obtained based on heterogeneous stress sensitivity model by Hertz contact deformation principle [9-12]. The results of different production pressure were compared between the two groups of cores.

2. Production model

Assuming the pores of heterogeneous tight sandstone capillary tubes are composed by particles with different properties. The basic stacking unit is a tight accumulation of 4 particles. Particles are deformed by the effect of effective stress, which leads to deformation of the pores of the capillary tube. The variation law of porosity recovery rate and permeability recovery rate with effective stress are obtained by calculating the seepage area of pores before and after deformation. The equations for porosity recovery rate and permeability recovery rate are as follows [9]:

$$\frac{\Phi'}{\Phi}=\left[1-\frac{\sqrt{S(R,\sigma)}-\sqrt{S'(R,\sigma)}}{\sqrt{S(R,\sigma)}}\right]^{3}=\left[\frac{\sqrt{S'(R,\sigma)}}{\sqrt{S(R,\sigma)}}\right]^{\frac{3}{2}} \quad (1)$$

$$\frac{K'}{K}=\frac{\Phi' S'(R,\sigma)}{\Phi S(R,\sigma)}=\left[\frac{S'(R,\sigma)}{S(R,\sigma)}\right]^{\frac{5}{2}} \quad (2)$$

Where Φ' is porosity after deformation; Φ porosity before deformation; S' is the seepage area after deformation; S is seepage area before deformation; R is radiu of particle; σ is effective stress on the pores of the capillary tube. K' is permeability after deformation; K is permeability before deformation. Therefore, the production equation can be dereived from Darcy theory as:

$$Q=\frac{K'A\Delta P}{\mu L}=\left[\frac{S'(R,\sigma)}{S(R,\sigma)}\right]^{\frac{2}{5}}\frac{KA\Delta P}{\mu L} \qquad (3)$$

Where Q is production; A is the area of the overcurrent cross section; L is the length of the rock in the flow direction; ΔP is the pressure difference between the two ends of the rock in the flow direction; μ is dynamic viscosity of the fluid.

3. Model Calculation

Two groups of capillary tube pores composed by different particle size particles were selected, the rock particles Poisson ratio were 0.22, and the elastic modulus was 12.9 GPa. The pore size ratio of each group of capillary tubes was 4:3 respectively (0.20 mm:0.15 mm) and 5:3 (0.25 mm:0.15 mm) [9]. Different particle size ratios can represent different heterogeneity of tight reservoirs. **Hata! Başvuru kaynağı bulunamadı.** is the relationship between effective stress and permeability of cores with different particle size ratios. With the increase of effective stress, the sensitivity of permeability stress is obvious.

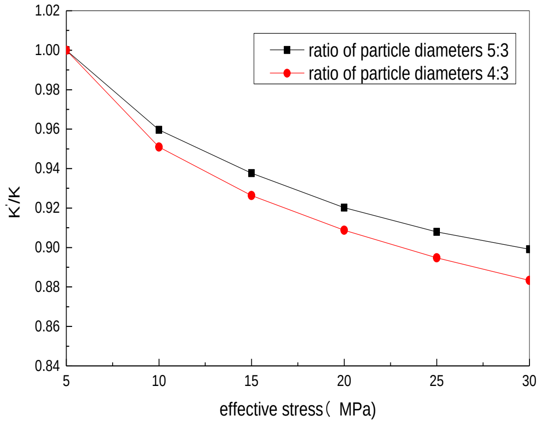

Figure 1. *Relationship between effective stress and permeability of different particles formed capillaries*

Table 1. *Basic parameters of cores*

Parameters	**Core 1**	**Core 2**
Diameter/mm	25	25
Length/mm	41.22	43.96
Porosity/%	15	14.18
Permeability/10^{-3} μm^2	9.83	2.47

Stress dependent permeability experiments have been conducted on 2 tight heterogeneous sandstone cores. Parameters are shown in Table1. Production prediction can be obtained by the production equation (3). The modified production under different production pressure (5-25 Mpa) has been calculated. The production results of core 1 are shown in Figure 2, the production results of core 2 are shown in Figure 3.

4. Results and discussion

As it can be seen from Figure 2 and 3, under the same effective stress, production increases with the increase of production pressure. Under the same production pressure, the production decreases with the increase of effective stress. However, the trend of this decline is increasing with the increase of effective stress. That is to say, the effect on production is small when the effective stress is low, but the effect is obvious when the effective stress can not be ignored. This means that the effect of stress sensitivity must be taken into account in the calculation of production for low permeability heterogeneous reservoirs when the effective stress is relatively high. Otherwise, there will be a great deviation in the calculation of production and the formulation of production systems.

Then compare the effects of different ratios of particle diameters from Figure 4. Due to the relatively small ratio of particle diameters, under the same effective stress, the lower recovery rate of permeability, the more obvious the stress sensitivity. As a result, the production is lower.

5. Conclusions

In this paper, a production calculation function has been derived on previous work, and production prediction on core scale has been made using it. Based on the work presented, the following coclusion can be drawn: The stress sensitivity needed to be taken into cosideration when the effective stress cannot be overlooked in the design of developing plan for tight reservoirs; and the severity of the heterogeneity has a noticeable influence on the production.

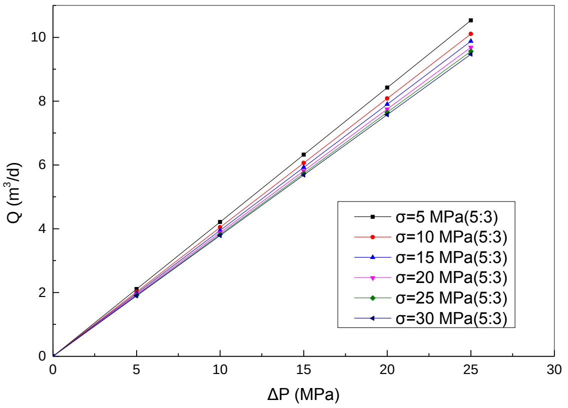

(a) ratio of particle diameters(5:3)

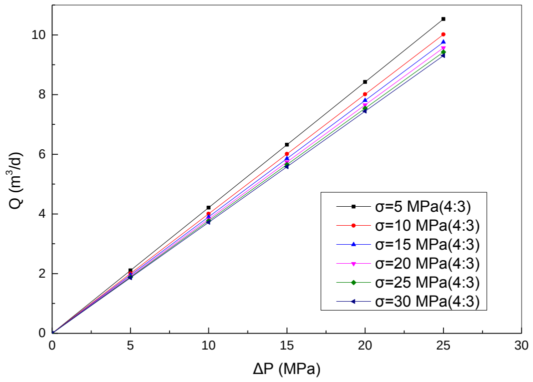

(b) ratio of particle diameters(4:3)

***Figure 2.** The production results of core 1*

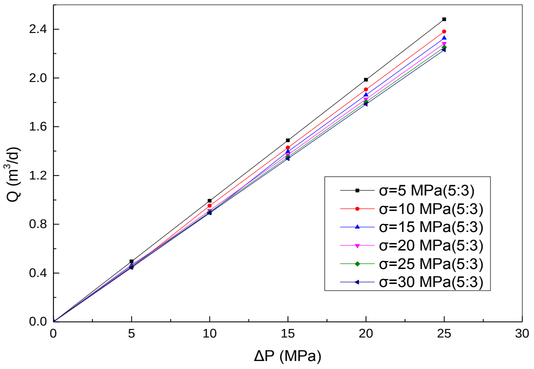

(a) ratio of particle diameters(5:3)

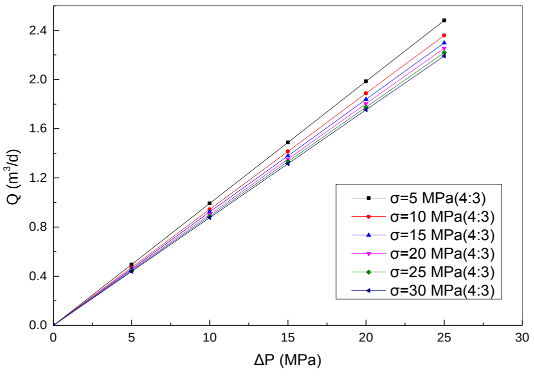

(b) ratio of particle diameters(4:3)

***Figure 3.** The production results of core 2*

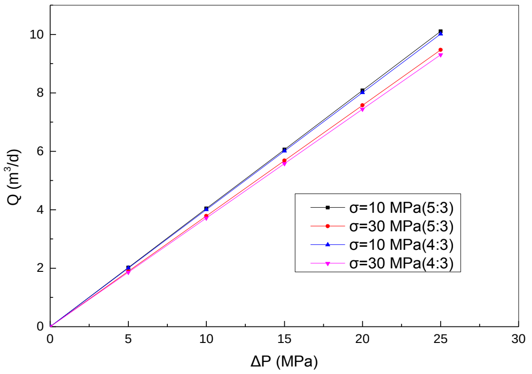

***Figure 4.** Comparison production results of different particle diameters ratio*

Acknowledgement

The authors are grateful for financial support from the State Major Science and Technology Special Project of China during the 13th Five-Year Plan (Grant 2016ZX05014-004).This paper has been presented in “4rd International Conference on Computational and Experimental Science and Engineering (ICCESEN-2017)”

References

[1] P.X. Wang, R.J. Liu. Universal model of stress sensitive coefficient for low permeability reservoir. Petroleum Geology and Recovery Efficiency, 2012 19: 75-77.

[2] J. Gao, J. Lü, J.L. Wang. Evaluation on stress sensibility of low permeability rock under reservoir condition. Chinese Journal of Rock Mechanics and Engineering, 2009, 28: 3 899-3902.

[3] Song, X.N. Cui, X. Su, et al. Determination and application of reasonable flowing pressure in ultra-low permeability reservoirs, peripheral Daqing.Special Oil & Gas Reservoirs, 2014, 21:102-105.

[4] R.J. Liu, H.Q. Liu, H.L. Zhang, et al. Study of stress sensitivity and its influence on oil development in low permeability reservoir. Chinese Journal of Rock Mechanics and Engineering, 2011, 30:2697-2702.

[5] P.C. Dong, G. Lei, B.Y. Ji， et al. Nonlinear seepage regularity of tight sandstone reservoirs with consideration of medium deformation. Chinese Journal of Rock Mechanics and Engineering, 2013, 32: 3 187-3 196.

[6] X.W. Wang, Y.Z. Huang, Z.M. Yang. Study of stress sensitivity of tight reservoir. Rock and Soil Mechanics, 2010, 31:182-186.

[7] L.Q. Wang, H.Q. Liu, S.G. Zhen， et al.Quantitative research on stress sensitivity of low permeability reservoir. Acta Petrolei Sinica，2009,30:96-99.

[8] X.Q. Tan, X.A. A. Yue, X.Y. Liu， et al. Stress sensitivity of low permeability heterogeneous reservoir and its influences on fluid distribution-taking CO2-drive oil reservoir as example. Petroleum Geology and Recovery Efficiency, 2009, 16: 92-94.

[9] G. Lei, H. Wang, P.C. Dong, Quantitative analysis on stress sensitivity of heterogeneous tight sandstone, 2015, 22: 90-94.

[10] M. Cevri, D. Üstü. Prediction of the Probabilities of the Transmission of Genetic Traits within Bayesian Logical Inference (ICCESEN 2016).

[11] N.M. Özgül, M.Y. Savaşçin, İ. Özkan. (2016) Recycling of Coal Ash in Production of Low Density Masonry Unit (ICCESEN 2016).

[12] M.C. Boz, F. Öner, B. Mavi. (2016) Natural Radioactivity and Radiation Hazards in Coals Extracted in Amasya, Turkey (ICCESEN 2016).

International Journal of Computational and Experimental Science and Engineering (IJCESEN)
Vol. 4-No.3 (2018) pp. 34-38
http://dergipark.gov.tr/ijcesen

ISSN: 2149-9144

Review Article

Yarns Emitting Far Infrared Rays

İsmail YÜCE*

Trakya University, Techinal Science Vocational School, Textile, Clothing, Shoe and Leather Department, 22030, Edirne – Turkey

* **Corresponding Author** : ismailyuce@trakya.edu.tr
ORCID: 0000-0001-6657-7169

Article Info:

DOI: 10.22399/ijcesen.368405
Received : 18 December 2017
Accepted : 17 November 2018

Keywords:

Bioceramic
Yarn
Infrared
Healthy textiles

Abstract:

Infrared radiation refers to electromagnetic radiation whose wavelength is longer than visible light, but shorter than terahertz and microwave radiation. Far infrared radiation (FIR) denotes radiation that is considered a kind of infrared radiation and includes wavelengths between 5.6-1000 micron. These rays are emitted by sun rays, human body, metals and some minerals. The positive effect of these rays on human health has already been mentioned and they are widely used especially in Far East countries in textile products and saunas.
For the textile products to emit such rays, the fibres or fabrics are required to gain some features. For this purpose, bioseramic powder is applied to the fibres and hence the textile becomes able to emit far infrared rays. This study deals with yarns that have acquired the ability to emit far infrared rays and their usage areas in textile. This review examines bioceramic powders, black body, production of FIR emitting yarns, features of yarns, various usage areas and future trends by means of literature review method.

1. Introduction

Far infrared radiation qualified as thermal radiation exists within electromagnetic spectrum and the wavelength of these rays range between 710 nanometre and 1 mm [1]. Infrared radiation is examined in three sections; namely near infrared radiation (NIR), middle infrared radiation (MIR) and far infrared radiation (FIR). Far infrared radiation is between 5.6 and 1000 micron and cannot be seen by human eyes [2]. These rays are emitted by sunlight, human body, metals and some minerals [21], [22]. Far infrared radiation has the feature of increasing blood circulation. With the increase in blood flow, oxygen and food stuffs are carried while carbon dioxide other waste substances move away. FIR rays between 4-14 μm are accepted to be beneficial for cellular growth and this radiation is named “life rays” by some researchers [2]. That far infrared radiation is beneficial for human health encourages its usage in commercial areas. As being one of such usage areas, saunas have been developed, benefiting from treatment features of far infrared radiation [3]. It has been reported that these saunas are used in the treatments of congestive coronary failure, hypertension and obesity [4].

The positive effects of far infrared radiation have also taken the attention of textile engineers and interest in textile designs with these features has increased in recent years. Far infrared radiation fabrics can be obtained in two ways: 1. Adding a bioceramic mineral or a natural or cultivated substance (bamboo charcoal) into a fabric (coating, lamination, pressing etc.) 2. Adding a substance with far infrared feature into polymer matrix during fiber spinning [6-10]. When applied into textile products, bioceramic materials can emit far infrared radiation. [2]. Especially, bioceramic materials can emit rays of 8-14 μm wavelength over 0,9 ε [5]. This study deals with black body emission and yarns that can emit far infrared radiation. Some information on production, usage areas, characteristics and future trends of these yarns has been presented.

2. Bioceramics, Bamboo Charcoal and Black Body Emission

Bioceramics can be defined as ceramics having biological function and they can emit far infrared rays (Figure 1) [2], [23]. Production of FIR textile can generally occur when nano or micro bioceramic powders are added to polymer matrix before the spinning of fibers. These powders are believed to retain and re-emit the rays emitted by body [2]. Some of the bioceramic powders that can be added to the textile structure for far infrared feature include Magnesium oxide (MgO), Zirconium dioxide (ZrO_2), Aluminium oxide (Al_2O_3), Iron III oxide (Fe_2O_3), Silicon dioxide (SiO_2), Germanium, Titaniumdioxide (TiO_2), Bamboo charcoal as well as such minerals as nephrite, pearl powder, tourmaline. Bioceramic materials emit FIR to the deep parts of diarthroses and hence blood circulation increases in tissues [9], [24], [25].

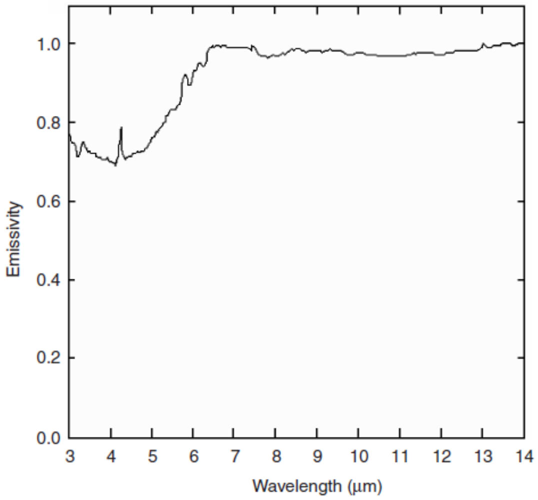

***Figure 1**. : FIR emission of bioseramic materials. Emission at and above 6 micron is about 0,98 ε [23].*

Bamboo charcoal powder is another material that attribute FIR feature to the textile products. Bamboo is generally grown up in low-latitude tropical and subtropical regions [12]. Bamboo charcoal powders are obtained by carbonizing the bamboo plant in ovens at 800-1200 °C and the harvest of the plant should be made after five years [26]. Bamboo charcoal powders produce far infrared radiation that can be absorbed quickly by human body. Reaching to the deep parts of human body and creating atomic and molecular frictions, these rays can increase internal temperature of the body. In addition, capillary vasodilation and the acceleration in blood circulation enable body temperature to be protected. Bamboo charcoal powders have the feature of anion emission, strong absorption, deodorization and moisture absorption [14].

In many studies, bamboo charcoal powders were used for the textile products to emit far infrared radiation. Fibers with different polymers were obtained from extruder by adding them into polymer matrix. The studies showed that bamboo charcoal powders increased the FIR emissivity rate [8], [12], [14].

The degree of emissivity of FIR materials ranges between 0 and 1. Each material above absolute zero emits IR. Each objects that are exposed to heat emit electromagnetic wave called black body emission. This electromagnetic wave is infrared in room temperature (wavelength: 0.77 ~ 1000 µm). While black body emission is evaluated as 1, other materials are named as grey body and their emissivity is between 0 and 1. For instance, human skin: 0.99; tree, wood, water, ice, frost, leaves: ~ 0.97; glass, concrete, brick: 0.94; stainless steel: 0.74; Aluminium: 0.18 [22].

3. Production of Yarns Emitting Fir and Their Usage Areas

FIR fibers are wound with various fibers so that yarns gain the property of FIR. [11-17]. FIR fibers are sold in the market with the trade names Celliant®, Emana®, Nilit®.
The working principle of fabrics obtained by bioceramic-applied fibers is based on the retroreflection of energy with a wavelength of 8-14 µm emitted from human body to the body. To put it differently, the fabric functions as a mirror [2], [18], [19]. The increase in the amount of FIR powders also increases the emissivity of these rays. However, the concentration of FIR powders should not exceed 5%. Powder concentration above 5% leads to decrease in the endurance of fibers as well as blockage in nozzles [20].

The effects of FIR on human health include decreasing swelling and ache in muscle and joints, encouraging renewal and quick recovery and improving blood circulation. For this reason, the ideal applications of FIR textiles have a comprehensive area ranging from local pain killers to others areas of supporting a health life. The products include therapeutic knee, elbow, waistbands, gloves, socks, shirt and belts (Figure 2) [2]. FIR clothes designed for sportsmen have been produced in order to regulate sweating, lactic acid and toxins [2]. In a study, it was found out that ceramic powders emitting FIR can decrease muscle tiredness and normalize acidification of strained muscles, which decreased muscle tiredness [23]. They can also increase muscle elasticity and relieves aching and muscle spasms by decreasing

Figure 2. *FIR textile products [18].*

the risk of injury. FIR textile products can help to heal injured, over engineered muscles, tendons and bonds [2], [27].

In Brazil, a study was carried out on FIR emitting clothes of twenty-one footballer. The yarn used in this study had PA 6-6 yarns with FIR feature and eleven of the footballers wore pyjamas having this feature. The remaining ten people (placebo) wore clothes made from PA 6-6 fiber that did not include FIR. The footballers wore these pyjamas after the training for three nights and slept for ten hours each night. The study showed that it is possible to benefit from FIR clothes in order to quicken recovery of muscle aches of footballers after training [29].

The main therapy function that FIR textiles aim is to encourage microcirculation. FIR therapeutic products have been designed for rheumatoid arthritis, knee ache, shoulder ache, neck ache and all kinds of arthritis [2]. In addition, positive results were obtained in a research on their effect on decreasing cellulitis [28]. FIR finds a place in healthy textile applications because of its property of expelling toxins from the body, stimulating cellular activity, increasing circulation, eliminating ache and swelling. These products are also used commercially in the treatment of Raynaud’s syndrome, sprains, fractures, bunions, gout, athlete’s foot, psoriasis, poor circulation, chilblains and RSI [2,30].

Ko and Berbrayer made a test on sixty patients with raynaud’s syndrome by using two types of gloves. One type of the gloves can emit FIR while the other is of conventional (placebo) type. As a result of the study, in both subjective and objective measures, it was reported that significant improvements were observed in the recovery processes of the ones who wore FIR gloves [31].

The surfaces (membrane) obtained by nano-size fibers have various usage areas in medicine because of specific big surface, small pore size and high porosity. In a study, germanium (Ge) and silicon dioxide (SiO_2) nano particles were mixed with polyvinyl alcohol and nanofiber surface was obtained. This surface encourages quick recovery in pledgets with its far infrared radiation emission and antimicrobial property as well as having the potential of preventing microbial infection. These products were also found out to have usage potential in medical textiles [33].

FIR fabrics are used in home textiles in such products as bed, blanket, sleeping-bag for improving sleeping quality. In order to improve sleeping-quality, discs that can emit far infrared radiation were placed in bed and blankets. At the end of the study, 350 persons were evaluate sleeping quality subjectively. After using the products, 80% of the subjects felt themselves well and very well while 63.5% of them found the product effective and very effective [32].

Textile products that can emit strong FIR are brilliant members for maintaining body temperature. Fabrics emitting FIR can keep the body warm in cold environments. For instance, sleeping pillows giving momentary heat in cool weather and gloves used for warming up the wrist can be examined under this category. Similarly, wool and cotton products impregnated with ceramic powders are available in the market in the form of socks, gloves, jacket and car seat pad. These products are put onto the market with their FIR health benefits in accordance with their marketing goals [2,30].

4. Fir Yarn Properties and Future Trends

Bamboo charcoal powders are black in colour as they are produced through carbonization process and hence the produced yarns are also black. However, in a study carried out by Li et al., white yarn was observed by modifying bamboo charcoal powders with titandioxid [8].

In a study carried out by Li et al. [7], fibers obtained by adding bamboo charcoal to nylon fibers were turned into textile surfaces after being mixed with polyethylene terephthalate (PET) and stainless steel. At the end of the study, the infrared radiation values of the obtained surface came out above 0,85 ε. As the values were above 0,8 ε, it was concluded that the obtained fabrics would be beneficial for human health.

In another study carried out by Lin et al. [13], polyester containing bamboo charcoal powders of 1.2% was wound with stainless steel wire (40 µm) and antibacterial nylon. Stainless steel was used as core spun and wound with FIR polyester and antimicrobial nylon. Three kinds of fabrics were obtained with these yarns. Fabrics were analysed according to spinning number (8, 11, 14 turn/cm) of hybrid yarn. According to far infrared test results, increase in spinning number is in proportionate to far infrared emission. FIR textiles represent a growing and exciting area in functional textiles. As new technologies and supporting studies continue, this area will certainly continue to grow up and create interest [2].

5. Conclusion

This study dealt with the effect of far infrared radiation on human health as well as producing yarns that emit such rays. In addition, this study presented some information on basic properties of FIR yarns. It was underlined that these rays are beneficial for human health. The study show up that bioceramic materials can emit these rays and that the fibers obtained through the addition of nano-size bioceramic powders in the extruder during fiber spinning emit FIR rays. These products range from home textile (bed, blanket) to daily used products (socks, gloves), therapeutic textiles (hand, knee and wrist bandages, socks for cellulitis).

References

[1] B. Demirel, G.A.K. Gürdil, A. Tekgüler, Kızılötesi Dalga-boyundaki Işınlarla Isısal Grafikleme Yöntemi ve Tarımda Kullanılma Olanakları. 25. Tarımsal mekanizasyon kongresi, 1-3 October, 2009 Isparta-Turkey.

[2] J. Dyer, Infrared functional textiles, 184-197, 2011. [Ed. Pan N., Sun G. Functional textiles for improved performance, protection and health. Woodhead Publishing Ltd.] DOI: 10.1533/9780857092878.184

[3] Infrared Saunas, Available: https://infraredsauna.com/infrared-sauna-detox/, Date of access: 10.08.2017.

[4] R. Beever, Do Far-Infrared Saunas Have Cardiovascular Benefits in People with Type 2 Diabetes?. Canadian Journal of Diabetes. 34(2) (2010) 113-118. *DOI: http://dx.doi.org/10.1016/S1499-2671(10)42007-9*

[5] TK. Leung, In Vitro and In Vivo Studies of the Biological Effects of Bioceramic (a Material of Emitting High Performance Far-Infrared Ray) Irradiation, Chinese Journal of Physiology 58(3) (2015) 147-155. *DOI: 10.4077/CJP.2015.BAD294*

[6] X. Hu, M. Tian, L. Qu, S. Zhu, G. Han, Multifunctional cotton fabrics with graphene/polyurethane coatings with far-infrared emission, electrical conductivity, and ultraviolet blocking properties, Carbon 95 (2015) 625-633. *DOI: https://doi.org/10.1016/j.carbon.2015.08.099*

[7] JH Lin, YT Huang, TT Li, CM Lin, CW Lou, Manufacture technique and performance evaluation of electromagnetic-shielding/far-infrared elastic warp-knitted composite fabrics, The Journal of the Textile Institute, Vol. 107, No. 4, (2016) 493–503. *DOI: http://dx.doi.org/10.1080/00405000.2015.1045253*

[8] QS Li, MS Xu, GJ Zhou, LQ Wang, Preparation and characterization of white bamboo charcoal PET fiber, Chinese Chemical Letters 21 (2010) 995–998. *DOI: https://doi.org/10.1016/j.cclet.2010.01.022*

[9] S. Wang, Y. Zhang, H. Liu, Wear Comfort Evaluation of Pearl-Cellulose Fabrics, Advanced Materials Research 175-176 (2011) 480-484. *DOI: 10.4028/www.scientific.net/AMR.175-176.480*

[10] YM. Park, JW. Shin, Surface Properties Studies of MPCMs Containing Fabrics for Thermo-regulating Textiles, Fibers and Polymers Vol.12, No.3 (2011) 384-389. *DOI: https://doi.org/10.1007/s12221-011-0384-x*

[11] CW. Lou, JH Lin, Evaluation of Bamboo Charcoal/Stainless Steel/TPU Composite Woven Fabrics, Fibers and Polymers 12, 4 (2011) 514-520. *DOI: https://doi.org/10.1007/s12221-011-0514-5*

[12] JH Lin, YT Huang, TT Li, CM Lin, CW Lou, Bamboo charcoal/phase change material/stainless steel ring-spun complex yarn and its far-infrared/ anion-releasing elastic warp-knitted fabric: Fabrication and functional evaluation, Journal of Industrial Textiles 46, 2 (2015) 624-642. *DOI: https://doi.org/10.1177/1528083715595007*

[13] JH Lin, ZC Yu, JF Zhang, CW Lou, Manufacturing Techniques and Functional Properties of the Bamboo Charcoal/ Antibacterial/ Stainless Steel Metal Composite Woven Fabric, Advanced Materials Research 910 (2014) 238-241. *DOI: 10.4028/www.scientific.net/AMR.910.238*

[14] JH Lin, AP Chen, CT Hsieh, CW Lin, CM Lin, CW Loy, Physical properties of the functional bamboo charcoal/stainless steel core-sheath yarns and knitted fabrics, Textile Research Journal 81(6) (2015) 567–573. *DOI: 10.1177/0040517510385173*

[15] YL Hsing, WH Hsing, CT Hsieh, JH Lin, CW Lou, Composite Environmentally Protective Sandwich Insulation Material Design. The 13th Asian Textile Conference, 763-766, 3–6 November, 2015 Geelong, Victoria, Australia.

[16] MA Pooley, DM Anderson, HW Beckham, JF Brennan, Engineered emissivity of textile fabrics by the inclusion of ceramic particles, Optics Express 24, 10 (2016). *DOI:10.1364/OE.24.010556*

[17] YH. Shih, JH. Lin, CT. Hsieh, CW. Lin, CW. Lou, Far-Infrared Nonwoven Fabrics Made of Various Ratios of Bamboo Fiber to Far-Infrared Fiber: Far-Infrared Emissivity and Mechanical Property Evaluations, The 13th Asian Textile Conference, 830-834, 3–6 November, 2015 Geelong, Victoria, Australia.

[18] F. Vatansever, MR. Hamblin, Far infrared radiation (FIR): Its biological effects and medical applications, Photon Lasers Med 1(4) (2012) 255–266. *DOI 10.1515/plm-2012-0034*

[19] A. Vathare, Far-infrared Rays Reflecting Fabrics for Improving the Performance of Human body, D. K. T. E. Society's Textile & Engineering Institute, Department Of Textiles, Ichalkaranji, 2014.

[20] YS. Lin, HC. Pan, CT. Lee, TK. Leung, Manufacturing method for a far infrared substrate, Patent Appl. 20080217163A1, Sept 11, 2008.

[21]https://tr.wikipedia.org/wiki/K%C4%B1z%C4%B1l%C3%B6tesi, Date of Access: 18.02.2017

[22] Emissivity Measure TSS-5X, Instruction Manual, Japan Sensor Corporation

[23] TK Leung, CM Lee, SY Tsai, YC Chen, JS Chao, A Pilot Study of Ceramic Powder Far-Infrared Ray Irradiation (cFIR) on Physiology: Observation of Cell Cultures and Amphibian Skeletal Muscle, Chinese Journal of Physiology 54(4) (2011) 247-254, *DOI: 10.4077/CJP.2011.AMM044*

[24] Biocera, Available: http://biocera.co.kr/far-infrared-ray-bioceara-sb.html, Date of Access: 07.08.2017

[25] D. Cobb, Ancient wisdom inspires ‘responsive’ Far Infrared fibres. Available: http://www.innovationintextiles.com/ancient-wisdom-inspires-responsive-far-infrared-fibres/, Date of Access: 27.12.2016.

[26] Bamboo charcoal, Available: https://en.wikipedia.org/wiki/Bamboo_charcoal, Date of Access: 08.01.2017.

[27] T. Furuta, Y Shimizu, Y Kondo, Evaluating the Temperature and Humidity Characteristics of a Solar Energy Absorbing and Retaining Fabric, Textile Research Journal, 66(3) (1996) 123-130. *DOI: https://doi.org/10.1177/004051759606600301*

[28] P. Richelmi, FM Bianchi, C. Angelinetta, Evaluation of the cosmetic effect of a pantyhose which helps to reduce imperfections caused by cellulite and local adiposities. The evaluation was carried out through a clinical test, Bio basic Europe, Milan-Italy.

[29] I. Loturco, CCC. Abad, FY. Nakamura, SP. Ramos, R. Kobal, S. Gil, LA. Pereira, FHP. Burini, H. Roschel, C. Ugrinowitsch, V. Tricoli, Effects of far infrared rays emitting clothing on recovery after an intense plyometric exercise bout applied to elite soccer players: a randomized double-blind placebo-controlled trial, Biol. Sport 33 (2016) 277-283. *DOI: 10.5604/20831862.1208479*

[30] Far Infrared Health, Available: https://farinfraredhealth.com, Date of Access: 07.08.2017

[31] GD. Ko, D Berbrayer, Effect of ceramic-impregnated "thermoflow" gloves on patients with Raynaud ’ s syndrome: randomized, placebo-controlled study, Altern Med Rev. 7(4) (2002) 328–335.

[32] S. Inoue, M. Kabaya, Biological activities caused by far-infrared radiation, Int J Biometeorol 33(3) (1989) 145–150.

[33] Chung J., Lee S., 2014. Development of Nanofibrous Membranes with Far-Infrared Radiation and their Antimicrobial Properties. Fibers and Polymers, Vol.15, No.6, 1153-1159, *DOI 10.1007/s12221-014-1153-4.*

International Journal of Computational and Experimental Science and Engineering (IJCESEN)
Vol. 4-No.3 (2018) pp. 39-42
http://dergipark.gov.tr/ijcesen

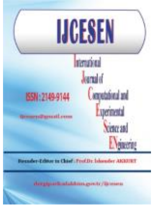

ISSN:2149-9144

Research Article

Comparison of Bearing Capacity of Piled Raft Foundations Consisting of Different Number of Piles under Static and Repetitive Loads

Baki BAĞRIAÇIK[1*],Sefer Ercan EPSİLELİ[1], Emre PINARCI[2] and Mustafa BELEN[2]

[1]Cukurova University, Engineering Faculty, Civil Engineering Department, 01330, Adana-Turkey
[2] Cukurova University, Engineering Faculty, Geology Engineering Department, 01330, Adana-Turkey

* **Corresponding Author** : bakibagriacik@gmail.com
ORCID:0000-0002-1860-2881

Article Info:

DOI:10.22399/ijcesen.477263
Received : 1 November 2018
Accepted : 26 November 2018

Keywords

Repetitive load
Static load
Sandy soil
Piled raft foundation

Abstract:

In this study, large-scale experiments have been carried out at 5th Regional Research and Development Headquarters Engineering of Highways in order to determine the contribution of the piles in the pile-raft foundation to the bearing capacity. The bearing capacity were determined for only the raft, the raft with single pile and the raft with four pile under static and repetitive loading. In the examinations, sand samples which were taken from a river bed were used. The sand was classified as uniform clean sand (SP) according to standarts.As a result of study following results were obtained. Only raft has reached lowest bearing capacity at different alternatives under static loading. When used single pile and four piles at piled raft foundation systems, the bearing capacity has increased by 1.130 and 2.52 respectively under static loading. As the number of piles increased, it was observed that the settlements at piled raft foundations under the same repetitive loading decrease.

1. Introduction

In recent years, due to the increasing population and decreasing land use requirements, there have been improvements in civil engineering applications. In order to meet the growing population needs, it has become necessary to plan and build multi-storey high-rise buildings in soft and loose ground conditions. During the planning of such structures, they are exposed to large static and dynamic loads such as their own weight, earthquake and wind of the structures should be considered. If these effects are taken into consideration, the loads to be transferred to the soil has reached the most extreme values. In this case, shallow foundations may be insufficient in terms of settlement and the bearing capacity. Piled raft foundations is most widely used for solve these problems. The piled raft foundations are generally not economical, according to the shallow foundations. But, they transport the load from structure to the soil layers with sufficient bearing capacity. There are a lot of studies about piled raft foundations. These studies were summaried below. One of the most important parameters of the determining bearing capacity at piled raft foundations while designing is the distance between piles. Determining the optimum value of the distance between piles make enough bearing capacity and settlement as well as economical designing of the piled raft foundation. In the literature, there are generally theoretical studies and numerical studies based on software packages like finite elements and boundary elements for determining to this parameters [1, 2, 3]. In these studies, it's stated that optimum distance between piles should be 2.5 times to 12.0 times the diameter of the pile. There are also experimental studies for determining for an optimum distance between piles in the literature. According to results of these experimental studies, optimum distance between piles should be 3 times to 4 times of the pile's diameter [4, 5, 6, 7, 8, 9, 10]. Another parameter affects the optimum distance between piles on the piled raft foundation design is the determining how to change the load proportions between piles and raft foundation. As mentioned in the literature, experimental studies in order to be able to determine load proportions between piles and raft foundation are very limited. In general, these parameters had determined by using theoretical studies, software packages based on finite and boundary elements methods. It's determined that according to the studies conducted by finite and boundary elements methods on the piled raft foundations, bearing capacity's 15%-40% carried by raft foundation and 85%-60% carried by the piles [11, 12, 13, 14]. Parameters like diameters of piles, configurations, and properties of installed soil also have importance for piled raft foundations. Although there are a limited number of experimental studies to determine these parameters [14], in general, many theoretical studies and the studies done by software packages based on finite and boundary elements exist [1, 2, 3]. The parameters obtained from these studies is also over a wide range. When looked to literature, there are a lot of studies about piled raft foundations. But, in the literature, there is not much experimental work carried out under static and repetitive loads to investigate the different parameters of piled raft foundations embedded in sandy soils. So, this paper aim to determine the bearing capacity for only the raft, the raft with single pile and the raft with four pile under static and repetitive loading.

2. Material and Method

The model tests were conducted in the Research and Development Laboratory of 5th Regional Directorate of Highways, using by big scale cyclic plate loading system. The testing equipment consists of the test case, loading unit, data logger, and software (Figure 1 and Figure 2). The test box is designed as a rigid and length, width and height 2 m. The model raft and model piles were produced from steel which has stiffness 210000 Mpa, unit weight 77 kN/m^2. The model raft foundation's width, length and thickness are respectively 300 mm, 300 mm and 20 mm (Figure 3). The model pile's dimension and length are 0.05 m and 0.4 m respectively (Figure 3). The actuator produce monotonic or repeated loads to a maximum capacity of 245 kN. This actuator give different amplitudes and frequencies which produce static and cycling load with electromechanical control system. In order to determine the values of the load and settlement which were applied on the foundation plate, an electronic load cell and a Linear Variable Displacement Transformer (LVDT) were used. In the examinations, sand samples which were taken from river bed were used. Experiments were performed at soil mechanics laboratory on oven-dried sand samples. The sand was determined as uniform clean sand (SP) according to ASTM [15], Percentage of Medium Grained Sand % 46.40, Percentage of Fine Grained Sand is % 53.60, Maximum Dry Specific Gravity is 17.06 kN/m^3, Minimum Dry Specific Gravity is 15.03 kN/m^3 and Specific Gravity is 26.80 kN/m^3.Test procedure are given below. The side faces of the test case were scaled as 10 cm for placement of the sand to the test case for desired density by layers. The required sand for 10 cm layer was poured into the test case from a distance as close as possible, after that spreaded along the surface of

Figure 1. *Test Box*

Figure2. *Model Piles and Raft Foundation*

Figure3. *Data Acquisition System*

the case with the help of a trowel. The sand has smoothened and spreaded homogeneously without applying pressure using thin wooden plates. After compaction is complete, the piled raft foundation plate was placed on the surface of the soil and embeded into the soil using loader systems with a constant penetration rate [14, 16]. As soon as the base of the raft foundation contacts the surface of the soil, the loading was stopped, controlled with a spirit level and the surface smoothness was provided. Prior to the test measuring systems was placed to the test test setup. The measuring systems includes two vertical displacement gauges placed two sides on the foundation plate, and the load cell. The initial values of the measuring systems were reset, and final necessary controls were made for the load to be applied effect uniformly and for the smoothness of the system. The load was applied vertically to the foundation plate center and static and repetitive loads. The loading rate was kept constant during the test. After the tests were completed, the obtained load-displacement curves transferred to datalogger device and converted to digital values via software. After every test, bearing capacities were determined by plotting vertical load-settlement curves.

3. Results and Discussions

In this study, the behaviors of piled raft foundation consisting of four piles in two different configuration under static and repetitive loading conditions were investigated by large scale laboratory tests. The findings obtained from the experimental results were shown as Figure 4 and Figure 5 under static and repetitive loads. The bearing capacity is defined as the vertical displacement value corresponding to 10 percent of the raft foundation. All the test results were interpreted using this approach. The bearing capacity for raft foundation, piled raft foundation at single pile and for piled raft foundation at four piles are 41.150 kN, 46.400 kN and 103.715 kN respectively from Figure 4. It has been determined that the lowest bearing capacity is the only raft foundation. It has seen that the use of piles from 1 to 4 has increased the bearing capacity at a considerable rate. From figure 5, as the number of piles increased, it was observed that the settlements (displacement) at piled raft foundations under the same repetitive loading decrease from nearly 5.5 cm to 3.5 cm.

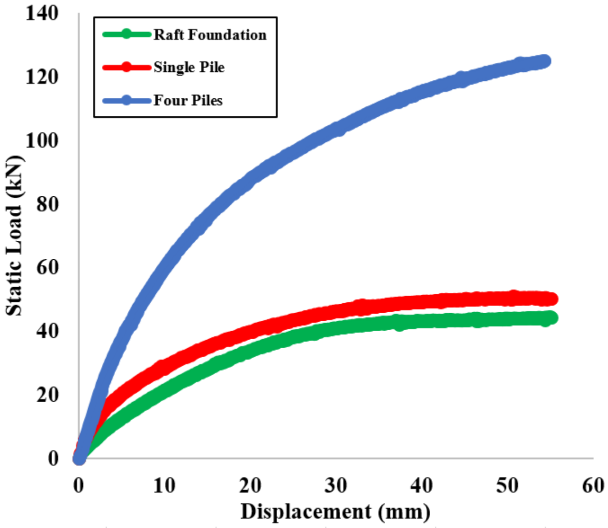

Figure 4. *The load-displacement graphics for static loading.*

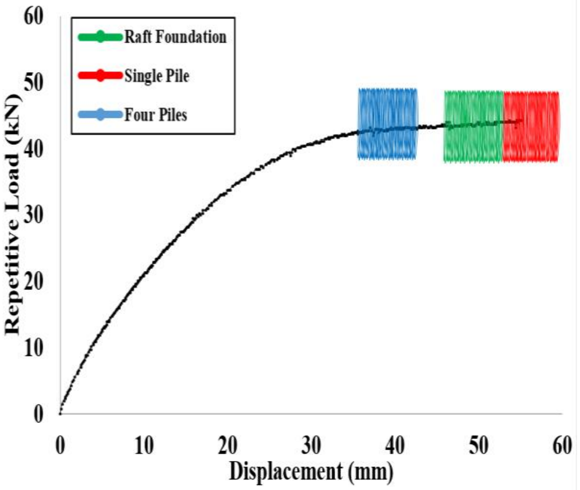

Figure 5. *The load-displacement graphics for repetitive loading.*

4. Conclusions

This paper aim to determine the bearing capacity for only the raft, the raft with single pile and the raft with four pile under static and repetitive loading. As a result of the study, the following results were obtained.

- The bearing capacity for raft foundation, piled raft foundation at single pile and for piled raft foundation at four piles are 41.150 kN, 46.400 kN and 103.715 kN respectively.
- It has been determined that the lowest bearing capacity is the only raft foundation.
- When used single pile and four piles at piled raft foundation systems, the bearing capacity has increased by 1.130 and 2.52 respectively under static loading.

- It has seen that the use of piles from 1 to 4 has increased the bearing capacity at a considerable rate.
- As the number of piles increased, it was observed that the settlements at piled raft foundations under the same repetitive loading decrease.

Acknowledgement

The tests were performed in the 5th Regional Research-Development Headquarters Engineering of Highways and Cukurova University Scientific Research Project Unit (Project Number: FBA-2017-8425) which is acknowledged.

References

[1] M. J. Tomlinson, Pile Design And Construction Practice, Chapman And Hall, London, UK, 2004.

[2] N. Erdemir and V. Okur, Kazık Gruplarının Sismik Etki Altındaki Performansı, Eskişehir Osmangazi Üniversitesi Mühendislik Mimarlık Fakültesi Dergisi. Sayı. 24, No.1, s. 91-107, 2011.

[3] A. G. Yazici, Kazıklar Arası Mesafenin Kazıklı Radye Temel Sisteminde Etkisinin İki ve Üç Boyutlu Analizi. Yüksek Lisans Tezi, Niğde Üniversitesi, Fen Bilimleri Enstitüsü, Niğde, 75s, 2013.

[4] T. Whitaker, Some Experiments on Model Piled Foundations in Clay, 6th International Congress of International Association of Bridge Structure Engineering, Stockholm, Sweden, pp. 124-139, 1961.

[5] H. Kishida, K. Matsushita and I. Sakamoto, Soil-Structure Interaction of the Elevator Tower and Concrete Footings. Proceedings of the 4th World Conference on Earthquake Engineering, Vol. 3, Santiago de Chile, pp 101–115, 1969.

[6] A. Tejchman, Model Investigation of Pile Groups in Sand, Journal of the Soil Mechanics Foundation Division, ASCE, USA, Vol. 99, No. SM2, 199–217, 1973.

[7] D. L. York and R. J. Leahy, Experiences with Heave and Relaxation of End Bearing Piles. Associated Pile and Fitting Corp. Pile Talk Seminer, New York, pp. 73-85,1979.

[8] R. W. Cooke, Piled Raft Foundations on Stiff Clays-A Contribution to Design Philosophy, Géotechnique, Vol. 36, No:2, pp. 169-203,1986.

[9] D. D. Sönmez, Orta Sıkılıktaki Kumdaki Kazık Gruplarının Negatif Sürtünmesi ile İlgili Bir Model Çalışma, Yüksek Lisans Tezi, Orta Doğu Teknik Üniversitesi, Fen Bilimleri Enstitüsü, Ankara, 89s,1994.

[10] N. F. Ismael, Axial Load Tests on Pile and Pile Group in Cemented Sands, Journal of Geotechnical and Geoenvironmental Engineering. pp 767-773, 2001.

[11] R. Butterfield and P. K. Banerjee, The Problem of Pile Group-Pile Cap Interaction, Géotechnique, Volume 21, No:2, pp. 135-142, 1971.

[12] F. Kuwabara, An Elastic Analysis for Piled Raft Foundations in Homogeneous Soils, Soils and Foundations, Vol. 29, No:1, pp. 82-92,1989.

[13] M. U. Ergun ve H. K. Türkmen, Kazıklı Radye Temellerin Etkin Tasarımı. 103I007 nolu Tübitak Projesi, Ankara, 2007.

[14] D. D. C. Nguyen, S. B. Jo and D. S. Kim, Design Method of Piled-Raft Foundations Under Vertical Load Considering Interaction Effects, Computers and Geotechnics, Vol. 47, pp. 16-27, 2013.

[15] ASTM D422, Standard Test Method for Particle-Size Analysis of Soils.

[16] S. Gök, Kazıklı Radye Temellerin Analizi. Doktora Tezi, İstanbul Teknik Üniversitesi, Fen Bilimleri Enstitüsü, İstanbul, 101s, 2007.

International Journal of Computational and Experimental Science and Engineering (IJCESEN)
Vol. 4-No.3 (2018) pp. 43-50
http://dergipark.gov.tr/ijcesen

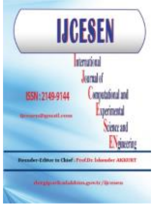

ISSN: 2149-9144

Research Article

Thermal Analysis of a Zirconium Dioxide Coated Aluminum Alloy Piston

Murat OZSOY[1]*, Ismet TIKIZ[2], Huseyin PEHLIVAN[1]

[1] Sakarya University, Engineering Faculty, Mechanical Engineering Department, Sakarya, TURKEY
[2] Kırklareli University, Engineering Faculty, Mechanical Engineering Department, Kırklareli, TURKEY

* **Corresponding Author** : ozsoy@sakarya.edu.tr
ORCID: 0000-0003-2400-5212

Article Info:

DOI: 10.22399/ijcesen.479222
Received : 06 November 2018
Accepted : 26 November 2018

Keywords

Thermal analysis
Finite element method
Thermal barrier coating
Aluminum alloy piston

Abstract:

Performance and operating costs are the most important factors in internal combustion engines. It is one of the most commonly used methods to coat pistons with advanced technological ceramic materials in order to improve performance and fatigue life in internal combustion engines. In this study, changes in temperature and heat flux were investigated in various thickness coatings made on a 2500 cc turbo diesel engine piston. As bonding coat, NiCrAl was used in a thickness of 0.2 mm, while ZrO_2 (zirconium dioxide) was used in thicknesses of 0.2-0.4-0.6 and 0.8 mm as thermal barrier coating material. The piston was modeled in PTC Creo parametric software and then transferred to ANSYS Workbench environment to create a mathematical model. Engineering calculations were also done using the finite element method. After the calculation, the temperatures at the depth of 5 mm from the combustion chamber upper surface, the binder layer upper surface, the thermal coating upper surface and the combustion chamber upper surface were compared. As a result, it was observed that the combustion chamber and the section at the depth of 5 mm from the combustion chamber had a temperature decrease of 13%.

1. Introduction

Thermal barrier coatings (TBCs) are extensively applied to protect metallic components of aircraft engines in an aggressive environment for improving the engine efficiency by increasing operating temperatures [1]. The zirconia based materials got increasing interest in the thermal barrier coatings [2]. These ceramic coatings help increase the entry temperature, which translates to higher performance and efficiency of the engine. However, with an ever-increasing demand for higher operating temperatures, a failure mode related to interaction between the ceramic coatings and molten deposits significantly affects the durability of TBCs [3]. Thermal barrier coatings (TBCs) have been widely used to provide thermal protection for the hot-section metal components in advanced gas turbines and diesel engines to improve thermal efficiency and performances [1–3]. Currently, 6–8 wt.% Y_2O_3 stabilized zirconia (YSZ) is considered as a good choice for the ceramic top coat material due to its superior durability during thermal cycling [4].

Ramaswamy at al. [5] study involves the need and developmental efforts made via Computational Fluid Dynamics (CFD) to generate a model via ANSYS - Fluent simulation software that predicts the temperature gradient across Thermal Barrier Coatings of different type ceramics and coating thicknesses.

To determine the optimum coating thickness, Dudavera at all. [6] simulated the thermal state of the piston using ANSYS Multiphysics. In this study, motor tests of the pistons using the single-cylinder unit of a four-cylinder two-stroke engine. The coating was applied to the surface of the piston head on the combustion chamber side.

Bolek at al. [7], investigate thermal barriers composed of ZrO_2 + 20%Y_2O_3 and β-NiAl intermetallic diffusion layers were fabricated on Inconel 713C. The numerical simulation of the real shape of the interface between the layers revealed that stress concentration zones occur not only at the peaks and valleys of the interface but also on the semi-flat surface in the midway between them.

Kumar at al. [8] has researched material structural forms. The analysis was carried out for Al - ZrO_2 combination with different volume fraction indices. A parametric study with different power-law indices, thickness ratios, aspect ratios, support conditions and load parameters on non-dimensional centroidal deflection had been performed.

Yerrennagoudaru and Manjunatha [9] designed conventional and modified piston in the Unigraphics software and the resulting flow field was analyzed for different piston configurations by using CFD software Fluent ANSYS-14.5. Compere temperature in conventional piston and modified piston, during analysis conventional piston means without ceramic and platinum coating, modified piston means with without ceramic and platinum coating and for these pistons Swirl ratio, Tumble ratio Y, Cross Tumble Ratio graphs has drawn.

Ma at al. [10] was investigated ultrasonic vibration was introduced to assist laser clad coatings, and the effect of ultrasonic vibration on the cross section morphology, microstructure evolution and dilution characteristics between coating and substrate. Thermal and structure finite element analysis has been employed to be informed the thermal stresses developed in Al_2O_3-SG, ZrO_2-12%Si+Al and ZrO_2-SG coatings subjected to thermal loading by Kocabicak at all. [11]. Systems with 0.4 mm coating thickness and 4 mm substrate material thickness were modelled. The finite element technique can be used to optimise the design and the processing of ceramic coatings.

Celik ve Sarikaya [12] were investigated the effect on residual stresses of porosity in MgO–ZrO_2 coatings on Al–Si alloy substrate. Thermal loads were applied to the model at the temperature of 550^{o}C using finite element method. Finite element calculations demonstrated that the highest thermal shock resistance was reached in the coating system with 7.5% small size sphere shape and uniformly distributed porosity. The coating with above 7.5% porosity had maximum values in radial, axial and shear stresses.

Taymaz at al. [13] studies the effect of surface preparation techniques. Thermal and structural finite element analysis has been employed to analyse the level of stresses developed Al_2O_3–SG, ZrO_2 (12% Si+Al) and ZrO_2–SG coatings subjected to thermal loading. Nominal and shear stresses at the critical interface regions (film/interlayer/substrate) were obtained and compared. The results showed that the ZrO_2–SG coatings have a higher thermal shock resistance than the Al_2O_3–SG and ZrO_2 (12%Si+Al) coating systems.

Thermal analysis evolution of MgO–ZrO_2/NiCrAlY coatings on Ni metal and AlSi alloy (LM13) substrates was studied by Sarikaya and Celik [14]. MgO–ZrO_2/NiCrAlY coatings were deposited on metallic substrates using an atmospheric plasma spray technique. Thermal loadings were applied to the model at the temperature range 800–1000 °C using finite element method. It was also found that the larger residual stresses were obtained with an increase of the coating thickness and interlayer bond coatings decreased residual stresses.

Mimaroglu at al. [15] employed coupled (thermal and structure) finite-element analysis to analyse the influences of porosity volume, size and distribution in MgO.ZrO_2-GG coating subjected to thermal loading. The results showed that the volume, size, location and distribution of the porosity have a significant influence on the level of the developed thermal stresses in the case of MgO.ZrO_2-GG coatings the optimum low-level stresses are developed with 7% small-size uniformly-distributed porosity allocated far away from the coating surface.

Khor and Gu [16] prepared coatings with different thicknesses and coating layers for bond strength and thermal cycling resistance tests. They were studied the microstructure, micro hardness, density, elastic modulus, thermal conductivity/diffusivity and coefficient of thermal expansion. The 8 wt.% Y_2O_3 stabilized ZrO_2 and NiCoCrAlY powders were used for the FGM coatings. The thermal cycling life of five-layer FGM coating is five times higher than that of the duplex coating which can be indicated from the FEA results.

Finite element code in ANSYS has been employed to analysis fracture in ceramic coatings subjected to thermal loading by Mimaroglu at all. [17].

Hypothetical material properties have been considered as material data for coupled (thermal and structure) finite element analysis and evaluated the stress intensity factors in different coatings. The results showed that the shorter the crack length and the thinner the coating, the sounder the coatings. Furthermore, coatings representing a wide range of thermal and mechanical properties have a close normalized stress intensity factor values. It is also concluded that the finite element technique can be used to optimize the design and the processing of ceramic coatings

As a result of the literature review made above, there is an increasing number of experimental and numerical studies on the thermal analysis of pistons. Generally, although bond materials were the same, different types of coating materials were used. In this study, the temperature distribution was examined for the original model and thermally coated model with four different thicknesses.

2. Geometric and Mathematical Modelling of the Piston

Geometric model of the piston body is modelled as a solid model at PTC Creo Parametric software. After modelling the piston body, first a 0.2 mm binding layer then thermal barrier coats with thicknesses of 0.2 mm-0.4 mm-0.6 mm and 0.8 mm modelled. Then for each thermal barrier coat a new assembly modelled, at last for finite element analyses four types of geometric models created. The Figure1 shows information about the properties of the geometric models.

H is a virtual path has 91 points on it for post processing. This path is created on the top surface of combustion chamber, 5 mm below the combustion chamber, on top surface of bond coat (binding layer) and on top surface of thermal coat.

After creating the geometric models of the original and thermal barrier coated pistons at PTC Creo Parametric, models were transferred to the Ansys Workbench software which is used for calculation by the finite element method. There are five types of models, first is original piston, second is 0.2 mm NiCrAl binding layer and 0.2 mm ZrO_2 thermal barrier coated, third is 0.2 mm NiCrAl binding layer and 0.4 mm ZrO_2 thermal barrier coated, fourth is 0.2 mm NiCrAl binding layer and 0.6 mm ZrO_2 thermal barrier coated and last one is 0.2 mm NiCrAl binding layer and 0.8 mm ZrO_2 thermal barrier coated.

After creating and transferring the geometric model to the ANSYS Workbench environment, the most important step is creating the mesh. For creating a healthy mesh, mesh metrics-element quality method was used. The Element quality option provides a composite quality metric that ranges between 0 and 1. This metric is based on the ratio of the volume to the sum of the square of the edge lengths for 2D quad/tri elements, or the square root of the cube of the sum of the square of the edge lengths for 3D elements. A value of 1 indicates a perfect cube or square while a value of 0 indicates that the element has a zero volume [18]. Table 1 shows the number of mesh, elements and also element quality of each mathematical model. All models have same bond coat as NiCrAl with a thickness of 0.2 mm so at table only thermal barrier coat included. Also a meshed model of one coated piston can be seen at Figure 2. During the meshing for binding layer and thermal barrier coat 0.1 mm element size of vertical direction used for a better mesh quality.

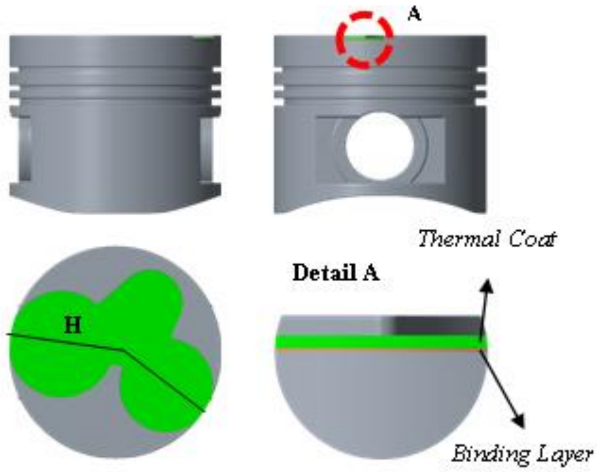

Figure 1. *Geometric model of the thermal coated piston.*

Table 1. *Mesh statics-element quality of original and thermal barrier coated pistons*

Model Properties	Mesh Statistics		Element Quality (average)
	Node Quantity	Element Quantity	
Base Piston	316197	208595	0.82
0.2 mm Coated	355475	215467	0.79
0.4 mm Coated	370882	219597	0.78
0.6 mm Coated	385398	223087	0.77
0.8 mm Coated	399914	226577	0.76

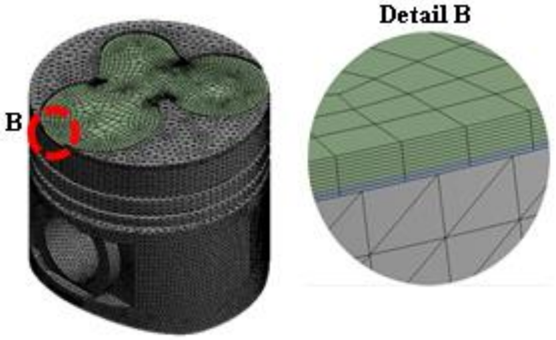

Figure 2. *Meshed model of 0.2 mm NiCrAl 0.8 mm ZrO_2*

SOLID87 3-D 10-Node Tetrahedral Thermal Solid and SOLID90 3-D 20-Node Thermal Solid used as element types for meshing the volumes.

SOLID87 is well suited to model irregular meshes (such as produced from various CAD/CAM systems). The element has one degree of freedom, temperature, at each node. SOLID90 has 20 nodes with a single degree of freedom, temperature, at each node. The 20-node elements have compatible temperature shapes and are well suited to model curved boundaries [18].

After creating the mesh, material properties of the piston, binding layer and thermal coat was defined. Table 2 also shows the materials and their thermal properties used at finite element analyses.

Table 2. *Thermal properties of the materials*

Material	Thermal conductivity [W/m °C]	Thermal expansion 10−6 [1/°C]	Specific heat [J/kg °C]
AlSi	237.5	21	960
NiCrAl	16.1	12	764
ZrO_2	3	11	460

The next step of the analysis is defining the boundary conditions. For this mathematical model different boundary conditions were defined in seven regions [19]. Boundary conditions are listed below at Figure 3 and Table 3 below. After creating the mesh, defining material properties and boundary conditions, solutions were made for five different models.

Table 3. *Properties of boundary conditions*

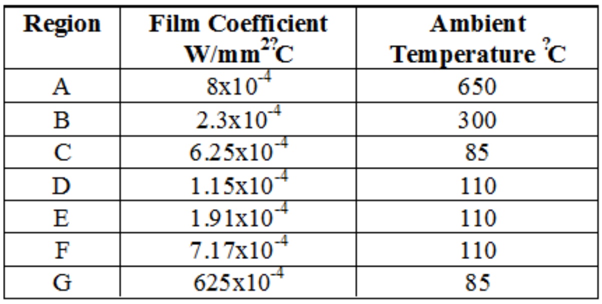

Region	Film Coefficient W/mm$^{2?}$C	Ambient Temperature $^{?}$C
A	8x10^{-4}	650
B	2.3x10^{-4}	300
C	6.25x10^{-4}	85
D	1.15x10^{-4}	110
E	1.91x10^{-4}	110
F	7.17x10^{-4}	110
G	625x10^{-4}	85

3. Results of the Analysis

As previously mentioned, five different models were used for the solution. First is original piston without coat. The other four models are coated. The binder coating on all models is 0.2 mm. Thermal coatings of four models are 0.2,0.4,0.6 and 0.8 mm ZrO_2. All models were solved under the same boundary conditions. Finally, the responses of the models to the same boundary conditions were compared. Solutions were made in a computer with four core Intel Pentium I7-3770K @3.50 Hz and 16 Gb physical memory on windows 10 x64 platform. To compare the results, 4 paths were formed on the piston combustion chamber surface, 5 mm below the piston combustion chamber, above the binding coating and above the thermal coating. Detail of this path can be seen at figure 1(H). Likewise, the heat flux of all models is compared. Figure 4,5,6,7 shows temperature effect (TE) of termal barrier coating (TBC) on paths named H and temperature distrubition (TD) on several surfaces. Further, total heat flux of uncoated and 0.8 mm ZrO_2 coated pistons can be seen Figure 8. After solutions for each coating, results were examined according to the upper surface of the combustion chamber of the uncoated piston. Maximum temperature occured 242.3 °C at uncoated piston, 236.7 °C at 0.2 mm ZrO_2 coated piston, 232.2 °C at 0.4 mm ZrO_2 coated piston, 227.95 °C at 0.6 mm ZrO_2 coated piston and 224.7 °C at 0.8 mm ZrO_2 coated piston. All results can be seen at Table 4.

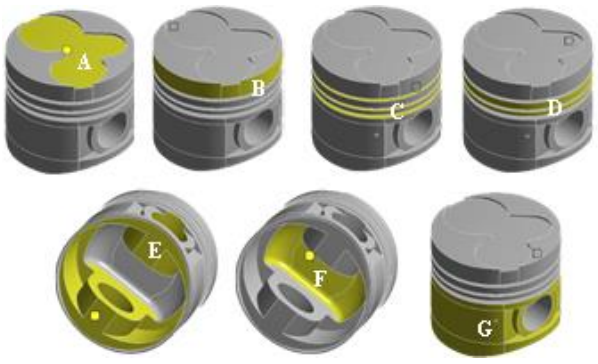

Figure 3. *Boundary condition regions of the piston*

Table 4. *Results of the finite element analysis*

Type	Uncoated	0.2 mm coated	0.4 mm coated	0.6 mm coated	0.8 mm coated
Combustion chamber top surface max. temp.	242.3	236.68	232.16	227.95	224.70
Binding layer top surface max. temp.	---	250.31	245.16	240.44	225.32
Thermal coating top surface max. temp.	---	264.97	277.79	290.67	299.38
Heat flux max	0.83	1	0.95	1.22	1.44
Piston Section max. temp.	236.4	230.63	226.27	222.27	219.31

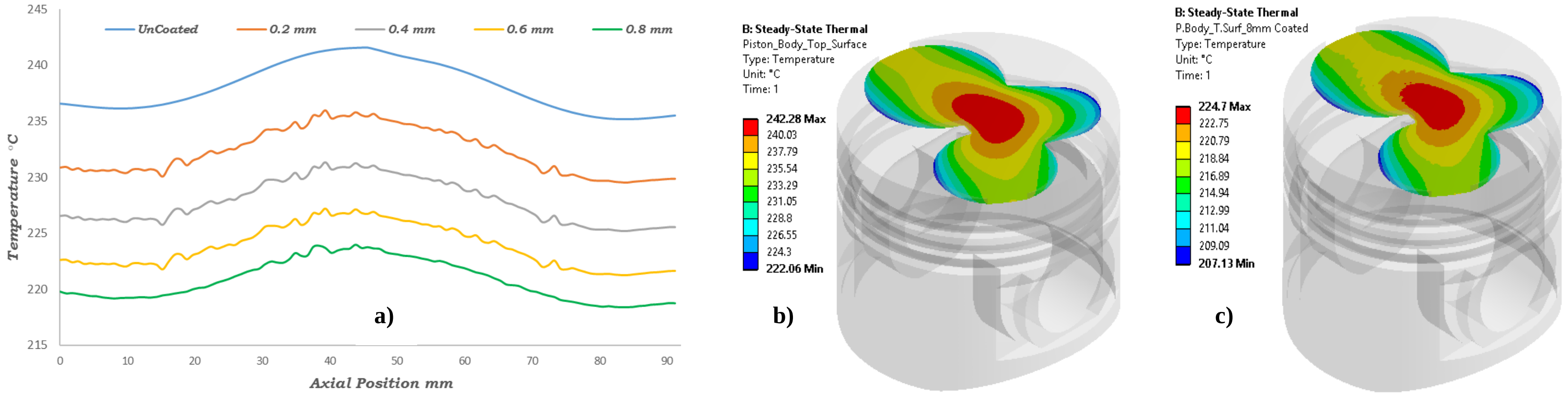

***Figure 4**. TE of TBC on piston combustion chamber top surface changing with distance (a), TD on combustion chamber of uncoated piston (b), TD on combustion chamber of uncoated piston with 0.8 mm ZrO_2 coated (c).*

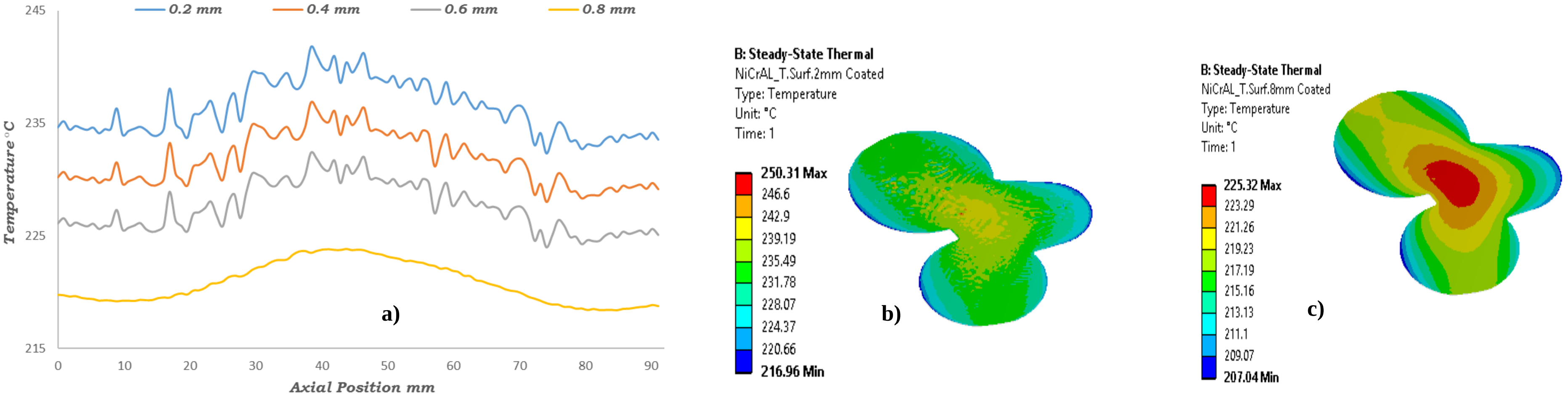

***Figure 5**. TE of TBC on Binding_Layer_Top_Surface changing with distance (a), TD on 0.2 mm NiCrAl coat with 0.2 mm ZrO_2 coated (b), TD on 0.2 mm NiCrAl coat with 0.8 mm ZrO_2 coated (c).*

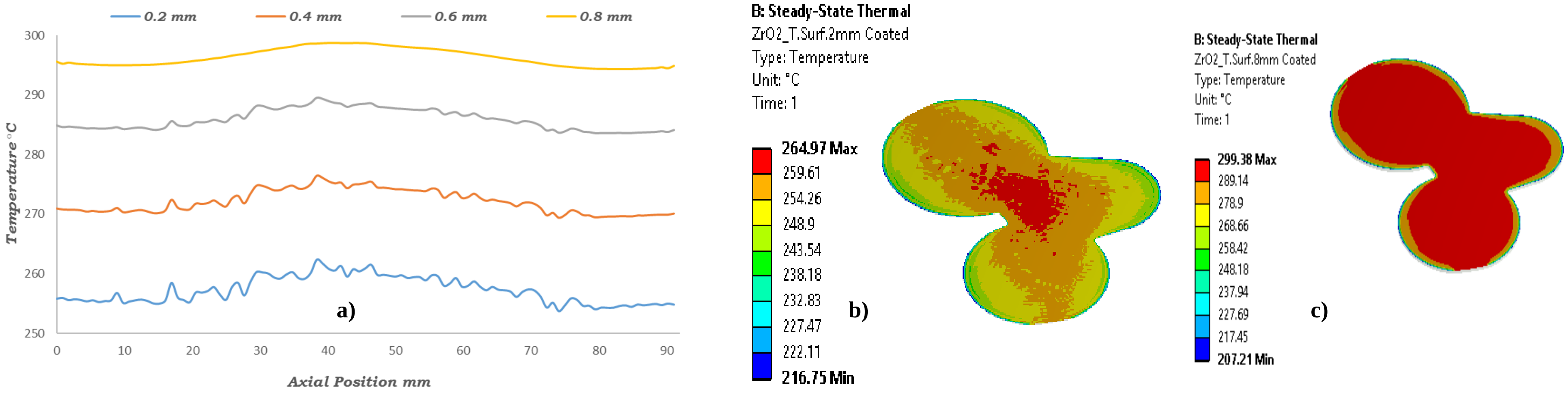

***Figure 6**. TE of TBC on Thermal_Coating_Top_Surface changing with distance (a), TD on 0.2 mm ZrO_2 coated (b), TD on 0.8 mm ZrO_2 coated (c).*

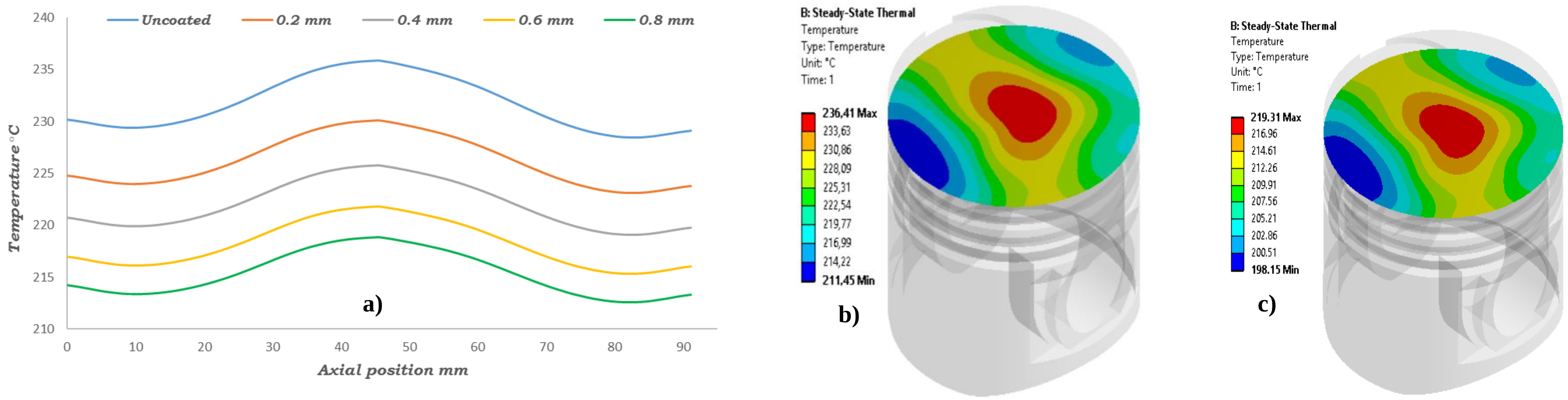

***Figure 7.** TE of TBC on 5mm below combustion chamber changing with distance (a),TD on 5 mm below combustion chamber at uncoated piston(b), TD on 5 mm below combustion chamber at coated with 0.8 mm ZrO_2 (c).*

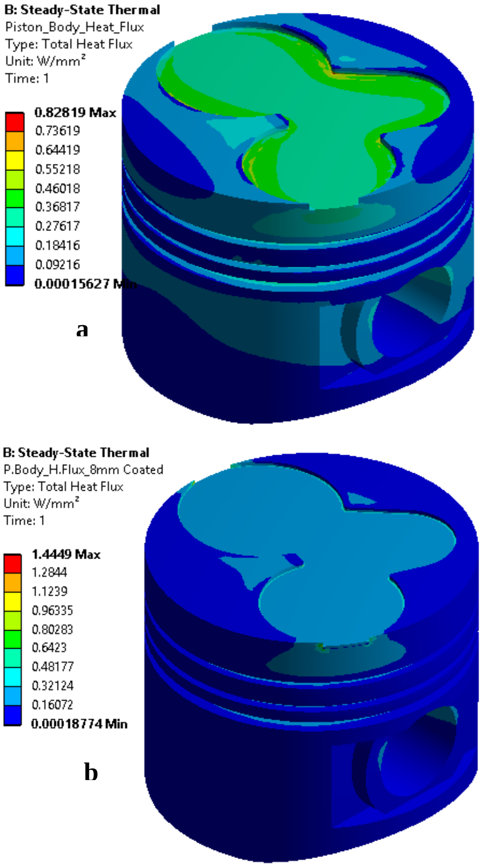

***Figure 8.** Total heat flux of uncoated piston a) and total heat flux of 0.8 mm ZrO_2 coated piston.*

4. Conclusion

When the results were examined, in the terms of occurring maximum temperature at piston combustion chamber top surface level (Figure 4), it was observed that there was 7% decrease between the uncoated piston and 0.8 mm ZrO_2 coated piston. Looking at the results of the bond coat (binding layer), a temperature decrease of 10% is observed (Figure 5). The temperature increase as a value of 13 % is observed on the top surface of the thermal coating (Figure 6).
This means that, the temperature is more confined on the thermal coating surface depending on the coating increasing.

At piston section level (5 mm below the combustion chamber top surface of uncoated piston, Figure 7) , a 7 % temperature decrease seen. At the end of the study, as expected a reduction in temperature was achieved by the coating of combustion chamber top surface. The next step of this study is optimization of the binding and thermal coats. Also make an experimental study in terms of verify the results.

References

[1] Fu, Y., Shao, C., Cai, C., Wang, Y., Zhou, Y., Zhou, G., Temperature induced structure degradation of yttria-stabilized zirconia thermal barrier coatings, Surface & Coatings Technology 351 (2018), 21–28 https://doi.org/10.1016/j.surfcoat.2018.07.057

[2] Khan, M., Zeng, Y., Lan, Z., Wang, Y., Reduced thermal conductivity of solid solution of 20% CeO_2 +ZrO_2 and 8% Y_2O_3 +ZrO_2 prepared by atmospheric plasma spray technique, Ceramics International, https://doi.org/10.1016/j.ceramint.2018.09.252

[3] Liu, H., Cai, J., Zhu, J., CMAS (CaO–MgO–Al_2O_3–SiO_2) resistance of Y_2O_3-stabilized ZrO_2 thermal barrier coatings with Pt layers, Ceramics International 44 (2018), 452–458 https://doi.org/10.1016/j.ceramint.2017.09.197

[4] Wang, J., Sun, J., Jing, Q., Liu, B., Zhang, H., Yu, Y., Yuan, J., Dong, S., Zhou, X., Cao, X., Phase stability and thermo-physical properties of ZrO2-CeO2-TiO2 ceramics for thermal barrier coatings, Journal of the European Ceramic Society 38 (2018), 2841–2850, https://doi.org/10.1016/j.jeurceramsoc.2018.02.019

[5] Ramaswamy, P., Shankar V, Reghu V.R., Mathew, N., Manoj, K.S., A Model to Predict the Influence of Inconsistencies in Thermal Barrier Coating (TBC) Thicknesses in Pistons of IC Engines, Materials Today: Proceedings 5 (2018), 12623–12631 https://doi.org/10.1016/j.matpr.2018.02.245

[6]Dudareva, N.Y., Enikeev, R.D.a, Ivanov, V.Y., Thermal Protection of Internal Combustion Engines Pistons, Procedia Engineering 206 (2017) 1382–1387 https://doi.org/10.1016/j.proeng.2017.10.649

[7]Bolek, T., Sitek, R., Sienkiewicz, J., Dobosz, R., Mizera, J., Kobayashi, A., Kurzydlowski, K.J., Simulation of the influence of the interface roughness on the residual stresses induced in (ZrO_2+Y_2O_3)+NiAl-type composite coatings deposited on Inconel 713C, Vacuum 136 (2017), 221-228 https://doi.org/10.1016/j.vacuum.2016.11.003

[8] Kumar, P.S.R., Kumar, P.N., Janardhana, G.R., Static Analysis of Al - ZrO_2FG Thick Plate Using Graded FEM, Materials Today: Proceedings 4 (2017), 8117–8126 https://doi.org/10.1016/j.matpr.2017.07.152

[9] Yerrennagoudaru, H., Manjunatha, K., Combustion analysis of modified inverted “M” type piston for diesel engine with platinum coating and without coating by using CFD, Materials Today: Proceedings 4 (2017), 2333–2340 https://doi.org/10.1016/j.matpr.2017.02.082

[10] Ma, G., Yan, S., Wu, D., Miao, Q., Liu, M., Niu, F., Microstructure evolution and mechanical properties of ultrasonic assisted laser clad yttria stabilized zirconia coating, Ceramics International 43 (2017), 9622–9629 https://doi.org/10.1016/j.ceramint.2017.04.103

[11] Kocabicak, U., Mimaroglu, A., Sarikaya, O., Mete, O.H., Comparison of the developed thermal stresses in Al_2O_3-SG, ZrO_2-12%Si+Al and ZrO_2-SG coating systems subjected to thermal loading, Materials and Design 20 (1999), 287-290 https://doi.org/10.1016/S0261-3069(99)00041-2

[12] Celik, E., Sarikaya, O., The effect on residual stresses of porosity in plasma sprayed MgO–ZrO2 coatings for an internal combustion diesel engine, Materials Science and Engineering A 379 (2004), 11–16 https://doi.org/10.1016/j.msea.2003.12.019

[13] Taymaz, I., Mimaroglu, A., Avci, E., Ucar, V., Gur, M., Comparison of thermal stresses developed in Al_2O_3–SG, ZrO_2–(12% Si+Al) and ZrO_2–SG thermal barrier coating systems with NiAl, NiCrAlY and NiCoCrAlY interlayer materials subjected to thermal loading,Surface and Coatings Technology 116–119 (1999), 690–693 https://doi.org/10.1016/S0257-8972(99)00121-8

[14] Sarikaya, O., Celik, E., Effects of residual stress on thickness and interlayer of thermal barrier ceramic MgO–ZrO_2 coatings on Ni and AlSi substrates using finite element method, Materials and Design 23 (2002), 645–650 https://doi.org/10.1016/S0261-3069(02)00047-X

[15] Mimaroglu, Kocabicak, U., A., Genc, S., Influence of porosity characteristics in Mg0.ZrO_2-GG coating subjected to thermal loading, Materials & Design, 18(1997), 77-80 https://doi.org/10.1016/S0261-3069(97)00042-3

[16] Khor, K.A., Gu, Y.W., Effects of residual stress on the performance of plasma sprayed functionally graded ZrO_2/NiCoCrAlY coatings, Materials Science and Engineering A277 (2000), 64–76 https://doi.org/10.1016/S0921-5093(99)00565-1

[17] Mimaroglu, A., Yenihayat, O.F. Avci, E., Numerical analysis of fracture in ceramic coatings subjected to thermal loading, Materials&Design 17 (1996), 283-287 https://doi.org/10.1016/S0261-3069(97)00023-X

[18] ANSYS Workbench Help

[19] Buyukkaya, E., Thermal analysis of functionally graded coating AlSi alloy and steel pistons, Surface & Coatings Technology 202 (2008) 3856–3865 https://doi.org/10.1016/j.surfcoat.2008.01.034